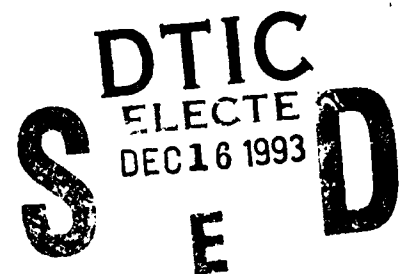


AD-A273 833



AFIT/GE/ENP/93D-01



**FAILURE MECHANISMS OF HIGH TEMPERATURE
SEMICONDUCTOR LASERS**

THESIS

David H. Leicester, Captain, USAF

AFIT/GE/ENP/93D-01

93-30479



Approved for public release; distribution unlimited

98 12 15 09 5

AFIT/GE/ENP/93D-01

**FAILURE MECHANISMS OF HIGH TEMPERATURE
SEMICONDUCTOR LASERS**

THESIS

**Presented to the Faculty of the Graduate School of Engineering
of the Air Force Institute of Technology**

Air University

**In Partial Fulfillment of the
Requirements for the Degree of
Master of Science in Electrical Engineering**

**David H. Leicester, B.S.E.E.,
Captain, USAF**

December 1993

Approved for public release; distribution unlimited

The opinions and conclusions in this paper are those of the author and are not intended to represent the official position of the DOD, USAF, or any other government agency.

Accession For	
NTIS CRA&I DTIC TAB Unannounced Justification	<input checked="checked" type="checkbox"/> <input type="checkbox"/>
By	
Distribution /	
Availability Codes	
Dist	Avail and / or Special
A-1	

DTIC QUALITY INSPECTED 1

Abstract

The primary intent of this research was to determine the influence of three common degradation mechanisms, dark area defects, facet degradation, and contact degradation, on the operational lifetime of GaAs edge-emitting semiconductor lasers driven by continuous current at 100°C. Inherent to this work was the quantified characterization of the lasers during their operation. This characterization arose as the power output as a function of driving current at room temperature before and after laser exposure to 100°C ambient temperature. These power vs. current characterizations were conducted at room temperature on each laser before and after exposure to 100°C as well as at the beginning and end of each laser's exposure to 100°C. An additional means of examining laser degradation came from measuring the current required over time to maintain a constant power outputs of 5, 7, or 10mW at the elevated temperature.

The research demonstrated that facet degradation and contact degradation were minor contributors to the bulk of the data base's degradation. Dark area defects were thus the primary degradation mechanism as the data's gradually increasing current necessary to maintain constant output will attest. An HF acid rinse on one laser, reacting aggressively to local crystal defects, highlighted the growth of dark area defects toward the lasing cavity due to continued lasing. One trend in the data was left unexplained. As a whole, the lasers performed with higher slope efficiencies at elevated temperature, contrary to previously documented research. This topic deserves future research.

Acknowledgments

I would like to thank a few people for their continued contributions to this research. I thank Major Paul Ostdiek for his multiple suggestions, patience, and quick response to my several needs. Next, I would like to thank Captain Carl Kutsche, WL/ELR, for the hardware, counsel, and visits to the lab. Finally, I would like to thank Kirk Weigand, WL/ELO, for aiding me through the final tests involving acid rinsing and pulsed operation of one laser.

David H. Leicester

Table of Contents

Abstract	iii
Acknowledgments	iv
List of Figures	ix
List of Tables	xi
I. Background and Description of Analysis Conducted	1
I.1. Background	1
I.2. Problem	3
I.3. Definitions	3
I.4. Summary of Current Knowledge	5
I.4.1. Crystal Defects	6
I.4.2. Output Power Degradation	7
I.4.3. The Three Phases of Failure	8
I.5. Research Goals	9
I.5. Chapter Summary	9
II. Literature Review	11
II.1. Dark Defect Degradation	11
II.1.1. Introduction	11
II.1.2. Background	12
II.1.3. Types of Dark Defects	18
II.1.4. Growth and Motion of Dark Defects	24
II.1.5. Variables Influencing Dark Defect Degradation	26
II.1.6. Dark Defects' Influence on Other Parameters	33
II.1.7. Dark Defects Degradation Summary	42

II.2. Facet Degradation	44
II.2.1. Introduction	44
II.2.2. Facet Heating	44
II.2.3. Influence of Material Traits and Cavity Dimensions	46
II.2.4. Dielectric Coating	46
II.2.5. Optical Flux Density and Current Flux Density	50
II.2.6. Variations of a Quaternary Semiconductor	51
II.2.7. Facet Degradation Summary	51
II.3. Contact Degradation	52
II.3.1. Introduction	52
II.3.2. General Requirements	52
II.3.3. Au-Based Contacts	53
II.3.4. Characteristic Performance	55
II.3.5. Wire Bond Degradation	56
II.3.6. Contact Degradation Summary	57
II.4. Chapter Summary	58
III. Research Support	61
III.1. Hardware Design/Calibration	61
III.2. Device Manipulation	65
IV. Methodology	69
IV.1. Initial Characterization	70
IV.1.1. The Characteristic Power Curve	70
IV.2. Pre-Aging Lasers	72
IV.3. Maximum Lasing Temperature	73
IV.4. Elevated Temperature Stresses	74
IV.4.1. Current vs. Operation Time	75

IV.5. Cavity Dimensions	76
IV.6. Testing Sequence	77
IV.7. Chapter Summary	77
V. Data Analysis	78
V.1. The Characteristic Power Curve	78
V.1.1. Gain, Threshold Current, and Efficiency Parameters	78
V.1.2. Power Measurement Justification	82
V.1.3. Sample Characteristic Power Curve	87
V.1.4. Characteristic Power Curve Summary	87
V.2. The Operational Lifetime of a Laser	88
V.2.1. Extrapolated Lifetime	88
V.2.2. Categories of Operation	89
V.2.3. Calculated Lifetime Function	90
V.3. Mechanisms Governing Breakdown	91
V.3.1. Contact Degradation	91
V.3.2. Facet Degradation	92
V.3.3. Dark Defect Degradation	95
V.3.4. Lasers Inoperational at Elevated Temperature	96
V.3.5. Degradation Mechanism Summary	100
V.4. Data Summary	100
V.5. Improved Performance at Elevated Temperature	106
V.5.1. Additional Annealing Effects	107
V.5.2. Improved Facet Reflectivity	108
V.5.3. Improved Contacts	110
V.5.4. Cavity Stress Reduction	112
V.5.5. Variable Internal Quantum Efficiency	112

V.5.6. Anomalous Improved Performance Summary	115
V.6. Summary and Conclusions	116
VI. Conclusions and Recommendations	119
VI.1. Research Goals	119
VI.1.1. Degradation Mechanisms	119
VI.1.2. Laser Characterization	121
VI.1.3. Lifetime Calculation	121
VI.2. Additional Observations	122
VI.3. Recommendations for Future Research	123
Appendixes 1-14	
1. Steel Plate Carousel Design Diagram	124
2. Laser Mount Design Diagrams	126
3. Power Measurement Block Diagram Setup	130
4. Hardware List	132
5. Optical Microscope Adapters Design Diagram	135
6. Cleaving Technique Checklist	137
7. TO-5 Package Mount/Wafer 599, 600, 706 Material Profiles	139
8. Spectral Distribution Graphs	143
9. Initial Rough Characterization of High Temperature Performance	146
10. Room Temperature Characterization of Laser 66B	150
11. Current Required During Aging for Laser 54C	154
12. Laser Characterization Summary Chart	156
13. Lifetime Calculation as a Function of Power	164
14. Variable List	166
Bibliography	169
Vita	173

List of Figures

Chapter I

1.	Pave Pace Photonic Backplane	2
2.	Estimation of time to failure by linear extrapolation	5
3.	Generation Time of first DSD as a function of temperature under 10kA/cm ² current density	7
4.	Failure rate and failure period (bathtub curve)	9

Chapter II

1.	Typical degradation modes	12
2.	Basic concept of (a) point defect and (b) plane defect	13
3.	Basic concepts of line defects	14
4.	Basic structure of a planar-type semiconductor laser	16
5.	Multiple structure of AlGaAs/GaAs (four well) and InGaAsInGaAsP (five well)	17
6.	Generation time of first DSD as a function the square of current density	19
7.	Generation time of the first DSD as a function of the junction temperature	20
8.	(a) Elongating mechanism of <100> DLD; (b) Electro-luminescent pattern	21
9.	TEM top-view micrographs of worm-like defects	23
10.	The basic structure for a ridge type laser	24
11.	Concept of the climbing motion process	25
12.	Schematic of the composition of the GRINSCH devices investigated	29
13.	CL and EBIC profiles before and after damage of GRINSCH devices	30
14.	CL and EBIC profiles before and after damage of GRINSCH devices	31

15.	(a) Temperature distributions along a laser's active stripe; (b) EL pattern of the degraded laser mapping DAD to temperature.	34
16.	Successive EL patterns mapped to temperature distributions	36
17.	Relations between degraded lasing characteristics and dark line numbers	38
18.	Relation between the increase of threshold current density and the decrease of spontaneous emission intensity	40
19.	Local temperature rise at the mirror facet of InGaAsP/GaAs SCH SQW laser without mirror coating	45
20.	Variations of facet reflectivity R_0 for the fundamental TE_0 mode as a function of active layer thickness	47
21.	Laser-current degradation rates $R = d/dt (I/I_0)$ vs. optical power	49
Chapter V		
1.	Change in gain spectra as a function of carrier injection	80
2.	Spreading of a TEM mode	84
3.	A generic edge emitting semiconductor laser	85
4.	Inner and outer facets of laser 49A	93
5.	Inner facet of 38B, displaying possible facet crystal damage	94
6a.	Inner and outer facets of 55A, after HF rinse	97
6b.	Inner and outer facets of 55B, after HF rinse	98
7.	The non-parallel facets of laser 45A	99
8ab.	(a) Initial and final room temperature average characterizations of the luminescent category of devices; (b) average characterizations for devices aged at 5mW	103
8cd.	Average characterizations for devices aged at (c) 7mW and (d) 10mW	104
8ef.	Average characterizations for (e) control devices and (f) entire data base	105

List of Tables

Chapter II

- | | | |
|-----|---------------------------------------------------------------------------------------------------------------|----|
| I | Ratio of annihilated donors (N_F/N_i) measure for different irradiation doses and for different materials | 32 |
| II | The conditions of the successive degradation steps | 37 |
| III | Requirements for a good ohmic contact for III-V compound semiconductors | 54 |

Chapter V

- | | | |
|------|-------------------------------------------------------------------------------|---------|
| Ia-f | Characterizations as grouped by operational history | 101-102 |
| II | Multiple characterizations for laser 55A | 109 |
| III | Lattice constants and the coefficients of thermal expansion for GaAs and InAs | 114 |

FAILURE MECHANISMS OF HIGH TEMPERATURE SEMICONDUCTOR LASERS

I. Background and Description of Analysis Conducted

This thesis describes and attempts to model the influence of elevated temperature on the operation of a semiconductor (SC) laser design provided by the ELR division of Wright Laboratory of Wright Patterson Air Force Base. The discussion begins with the background outlining the need for this research. The sections following, in order of discussion, include a detailed problem statement, definitions of aspects intrinsic to the research, a summary of related research, and a list of research goals.

I.1. Background

As the semiconductor laser becomes a standard tool for communications technology, the demand for applying it in a broader range of operation environments grows. Their tiny size makes them highly compatible with the ever shrinking electronic world. Also, with their inherent efficiency and simple structure they will be fairly easy to incorporate into the business of communications and control applications.

The Air Force has a few of its own proposed uses for SC lasers. One such project is a laser-based solution for the growing complexity of the PAVE PACE Interboard Communications. This unit controls an aircraft's electrical nervous system. Presently the communications demand twenty two thousand metal interconnects between the unit and an aircraft's electrical system. The 22,000 connectors could be replaced with fewer optical

connections as has been proposed by the unit in Fig. 1. All optical interfacing hardware is presently available except for a laser transmitter.

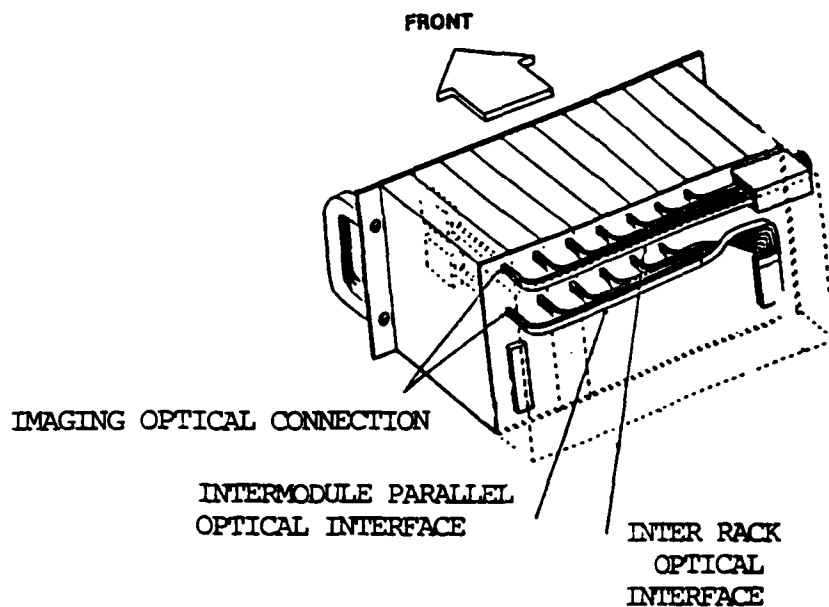


Fig. 1 (WL/ELRD): PAVE PACE Photonic Backplane

Another project involves Auto-Target Recognition and the desire to identify and classify a Target in Real Time, this demands a faster data processing ability which could be handled by lasers. A final proposed use is a pilot helmet-mounted laser projector to highlight the important data where the pilot can always find it.

The problem, and reason for this thesis, arises from the fact that present commercial semiconductor lasers do not operate in the high temperature environments, 100-200°C, found in aircraft. One solution demands active cooling of commercial lasers to bring the ambient temperature down to typical operating conditions. This is a heavy, cumbersome solution that defeats the advantage of the laser's small size and generates more heat. The design of lasers able to operate in the high temperatures provides an alternate solution. Design of such lasers begins with the characterization of how lasers operate in high temperatures.

1.2. Problem

The primary goal of this research will be to provide and explain a modeled description of the influence of a 100°C ambient temperature on the continuous operation of the laser design provided by Wright Laboratories. This research will analyze the lasers under continuous wave operation and focus on operational temperatures between 100-200°C. Other products of this research include the change of the spectral distribution with temperature and aging, a statistical evaluation of the operational lifetime as a function of power at 100°C, and a proposed description of the mechanisms dictating the breakdown. The detailed description of the breakdown mechanisms shall direct future improvements of the design under analysis.

1.3. Definitions

Two primary concepts need clarification for this research, the failure criteria and accelerated life testing. Beginning with the failure criteria, Fukuda describes the most common standard for laser failure as being when the device requires 1.5 times the initial current, $I = 1.5 \cdot I_0$, to maintain a constant power output (1:88). This definition requires operation of the laser at a constant power output. Maintaining constant output requires a feedback network linking the power output and the driving current. Continual data sampling monitors the current's change with time. This criterion can be approximated by periodically inspecting operation and manually adjusting the current to maintain the power. This will serve as the failure criterion for this research.

A second failure criterion, though predominantly used for light emitting diodes, LED's (1:87), is a 1 decibel decrease in optical power from the initial, or some predetermined, level while driving the device at a constant current. This criterion requires that the devices operate continually at the established current. Although possible, this is not a standard evaluation of lasers and thus not used in this research.

As a modification to the above criteria, periodic power measurements as a function of current could be taken to obtain the change in the external quantum efficiency. From the change in external quantum efficiency the current required to maintain a fixed reference power could be interpolated. This criterion represents a compromise of the two above recognized standards. The result would be the mean time to failure, MTTF, for a constant drive current and still employing the fixed power output to determine when a failure current level is attained. The drawback to this scheme is that it would not conform to any exercised standard found in technical literature.

Moving on from the failure criteria, the concept of accelerated life testing needs clarification. As the typical laser operates for approximately 10,000 hours before failing, accelerated life testing presents the only practical means for extrapolating the MTTF. Under high stress environments differing in only a single variable, device life can be estimated by monitoring the time to failure. From several devices under identical high stress environments a cumulative failure distribution can be obtained. Fukuda provides three empirical relations for the lifetime of a laser (1:106):

$$life = A_T \exp(E_a / kT) \quad (1.1)$$

$$life = A_P P^{-n} \quad (1.2)$$

$$life = A_J J^{-n} \quad (1.3)$$

where in the respective equations the variables are the temperature, T , (an Arrhenius relation for T), the current density, J , and the light output power density, P . The exponent, n , is a distinct positive number for equations 2 and 3. Eliseev cites the activation energy, E_a for GaAlAs/GaAs laser diodes to be typically between 0.7-0.9 eV, and for InGaAsP/InP radiating heterostructures to be 0.61 eV (2:33). The arguments, A_T , A_P , A_J , are constants reflecting the fixed variables influencing operating conditions. The first two relations employ the current required to maintain constant output power as a measure. The third relation employs the 1 dB output drop for a constant current as the failure criterion. Fukuda goes on to reason that due to the small margin of permitted operation parameters,

sufficient acceleration can not always be applied. In this case, a linear extrapolation can be employed to determine the MTTF as shown in Fig. 2.

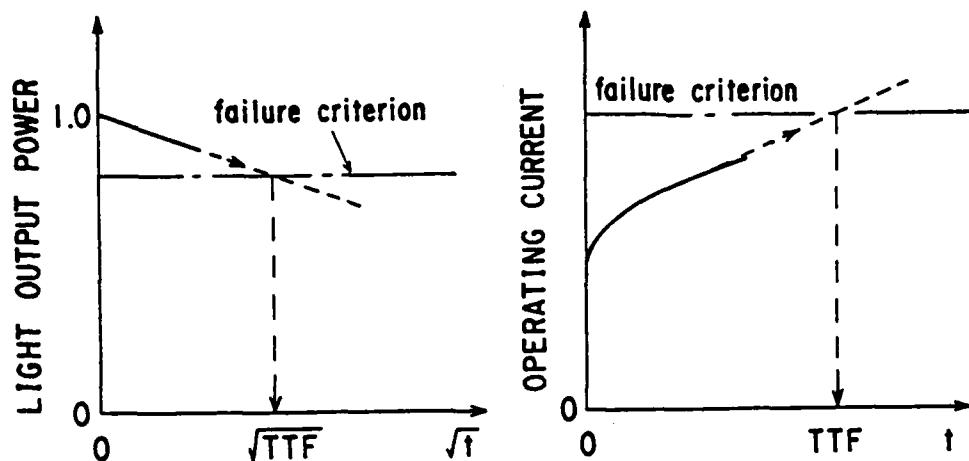


Fig. 2 (1:107): Estimation of time to failure by linear extrapolation

An intermediate goal of this research would be to determine the lifetime as a function of power and temperature. From the above development the function would assume a form of:

$$life = AP^{-n} \exp(E_a / kT) \quad (1.4)$$

As this goal would demand the analysis of over 100 laser packages, the immediate goal discussed in this thesis is to analyze the lifetime at 100°C. Thus the function to be modeled will be:

$$life = A_p P^{-n} \quad (1.2)$$

1.4. Summary of Current Knowledge

The next section highlights those aspects of the literature review most involved with the research plan. This general summary outlines the influence of crystal defects, optical power output, and the different periods attributed to the failure rates of semiconductor devices.

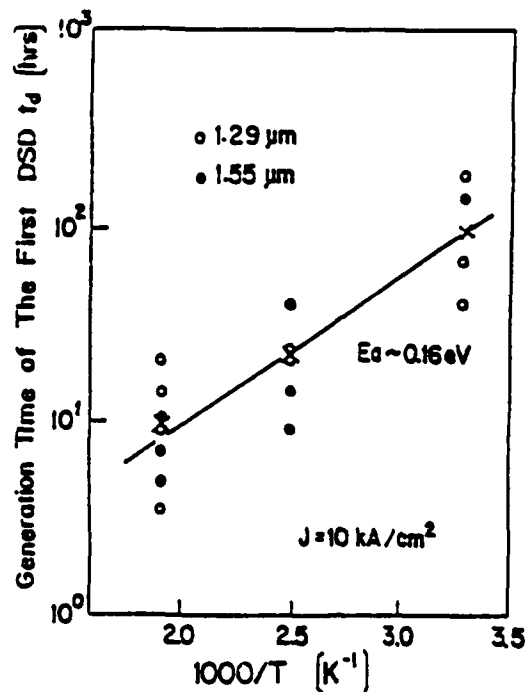
I.4.1. Crystal Defects. As this research focuses on the breakdown of lasers, much of the background study involves describing the mechanisms causing laser failure. The first study, conducted by Kobayashi et al., demonstrated that local temperature rise, current crowding, and a lower breakdown voltage were present near dark line defects when these values were compared to those of a sound region of a device (3:508). For clarification, dark line defects are local interruptions of the crystal structure which enhance non-radiative recombination. One observation made from this study was that the current density at a dark line defect will typically be twice that of an undegraded region. This will hold until the fatal degradation, when a defect shorts the active region.

Another report by Fukuda et al. modeled the evolution of the dark spot defects, DSDs, in laser operation (4:1246). Assuming that defect generation would depend on current and junction temperature, device aging was carried out at forward current densities of 5, 10, and 15 kA/cm² and junction temperatures of about 30, 130, 250°C. The generation time of the first DSD, t_d , strongly depended on current density and mildly on temperature. The dependence on current density for a fixed temperature can be expressed approximately by the following relation:

$$t_d \propto \exp(-AJ^2), \quad (1.5)$$

where J is the injected current density and A is a constant. Fig. 3 graphs the generation time for the first DSD as a function of temperature. For the range of variables, the generation time of DSD's is linked strongly to current density, mildly to temperature.

The growth of dark line defects, DLDs, is strongly linked to current density as well. Fukuda et al. researched this topic by first baking 8 samples at 250°C for 200-300 hours without operation (5:L87). The pulse threshold current never changed and no dark defects were observed. Then they operated 2 samples at 10 kA/cm² and 120-130°C and the lasers degraded at the same rate as samples run at 10 kA/cm² and 250°C. Finally, 5 samples were operated at 5 kA/cm² and 120-130°C, and only a few DSDs were observed



The lasers produced approximately linear degradation curves with time and the corresponding degradation rates increased exponentially with optical power. The lasers operating at 30mW demonstrated a 35% lower degradation rate than lasers that were operated solely at 30mW in isothermal tests at 50°C. Also, catastrophic failures occurred among only 20% of the devices, all during the 50mW phase, significantly lower than the 80% of the isothermal tests. The lasers intended to operate in the reverse sequence demonstrated drastically different behavior. All devices failed catastrophically with a mean time to failure of 1 hour during the first 50mW phase. These results imply that laser lifetime may be enhanced by applying low power pre-aging to the devices. This important conclusion prompted the pre-aging of the data base used for this thesis.

I.4.3. The Three Phases of Failure. The mechanisms predicted to cause failure in the devices under study arise during the device's failure period attributed to normal "wearing out". As for all semiconductor devices, two other general mechanisms may dictate an early break down of the device. Failure during an early period may occur in devices that have large structural faults that arose during fabrication. Devices failing in this period effectively never satisfied design parameters. A second failure period, described as the random failure period, accounts for the random failure inherent to any large set of data and the distribution functions inherent to several measurements. The final failure period is attributed to the device wearing out. Fukuda links these three failure periods together and describes them as the bathtub curve, as displayed in the figure below (Fig. 4). The study will focus on those devices that "wear-out" and hence measures will be taken to filter out the devices that break down in the early failure period. As the second period is random, no means can be taken to filter out devices failing in this fashion.

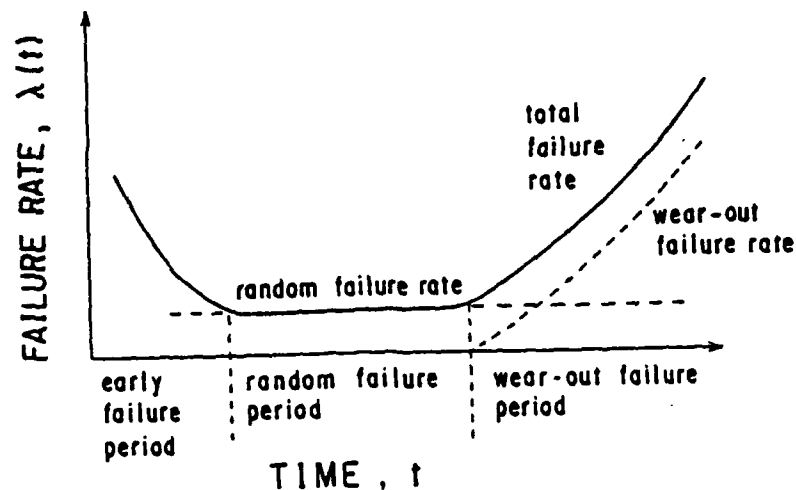


Fig. 4 (1:87): Failure rate and failure period (bathtub curve)

I.5. Research Goals

The primary goal of this research is to determine the influence of the three primary mechanisms of degradation inherent to laser reliability, dark area defects, facet degradation, and contact degradation. This determination of influence includes demonstrating which mechanisms exist and which dominate degradation. This goal requires two more immediate goals to quantify this influence. The first is the characterization of the design's power output as a function of current at room temperature and 100°C. The second is the lifetime of the design as a function of power at 100°C. Elaboration of these goals will be presented throughout the document.

I.6. Chapter Summary

This chapter outlined the need to model the influence of elevated temperature operating conditions on the operation of edge emitting semiconductor lasers. As future aircraft circuitry continues to demand more signal processing at faster operating rates, the need for laser signal transmission increases. Aircraft electronics operating conditions typically run between 100-200°C, this demands that the lasers must be able to operate under such conditions. As today's lasers can not operate in this environment, efforts must

be conducted to design lasers that can. Of fundamental interest to the design of lasers operating at elevated temperatures is an understanding of what these temperatures do to lasers.

The primary interest of a device's operation is the definition of device failure. The standard considers the laser as failed if the current required to drive the laser at a specified power level increases from the initial current by 50%. Having set the standards of acceptable performance, we are concerned with the physical mechanisms causing failure and their models. This concern is the central focus of this thesis.

The next section of this chapter highlighted topics from recent research influencing high temperature operation of lasers. The primary cause of degradation typically arises from dark area defects, or imperfections in the crystal structure of the device. It is also found that lasers often last longer when they are pre-aged at low output power for the first few hours of operation. The final highlight noted that three failure periods, inherent to any solid state device operation, outline the operation of the lasers. The interest of this research focuses on the third failure period, involving mechanisms that wear out the device. Therefore, the lasers were screened to eliminate those that would fail in the first period. These topics receive more attention in chapter 2, the literature review.

The final section outlined the three goals of this research. These goals are listed below:

1. (Primary goal) To determine which of three mechanisms, dark area defects, facet degradation, or contact degradation, influence and dominate the operational degradation of the laser design.
2. To characterize the design at room temperature and 100°C.
3. To determine the lifetime of the design as a function of power at 100°C.

II. Literature Review

This chapter presents a detailed review of published research relating to the degradation of edge emitting semiconductor lasers. The last chapter touched on highlights of this research but this chapter provides some depth to these highlights. Three general mechanisms arose as the focal points for research, dark defects, facet degradation, and ohmic contact degradation. This review breaks into these three general areas and each presents its own introduction and summary. The first section provides an additional background outlining laser models as they pertain to the crystal degradation in dark defects. A final summary collects the observations of this review.

II.1. Dark Defect Degradation

II.1.1. Introduction. Along with the advent of AlGaAs/GaAs lasers came the problem of how to prevent the laser from destroying itself in normal operation. The intensity of power inherent to semiconductor lasers generated high temperatures and mechanisms that could melt or shatter the semiconductor. If eventual decay could not be prevented than at least it could be minimized to extend the laser's operational lifetime. Thus the need to explain and model the degradation of the laser's operation arose. Three general categories of degradation exist which are based on the rate at which the device's characteristics change. These categories are the gradual, rapid, and sudden modes. Sample characteristics demonstrating this degradation include the laser's output power for a constant current input over time, (Fig. 1a), or the current needed to maintain a constant output power over time, (Fig. 1b). The dominant contributor to rapid degradation has been attributed to what are known as dark defects. The aim of this chapter is to document the variety of dark defects, their affects on degradation, and the proposed remedies to these attributes limiting the operational lifetime of lasing devices.

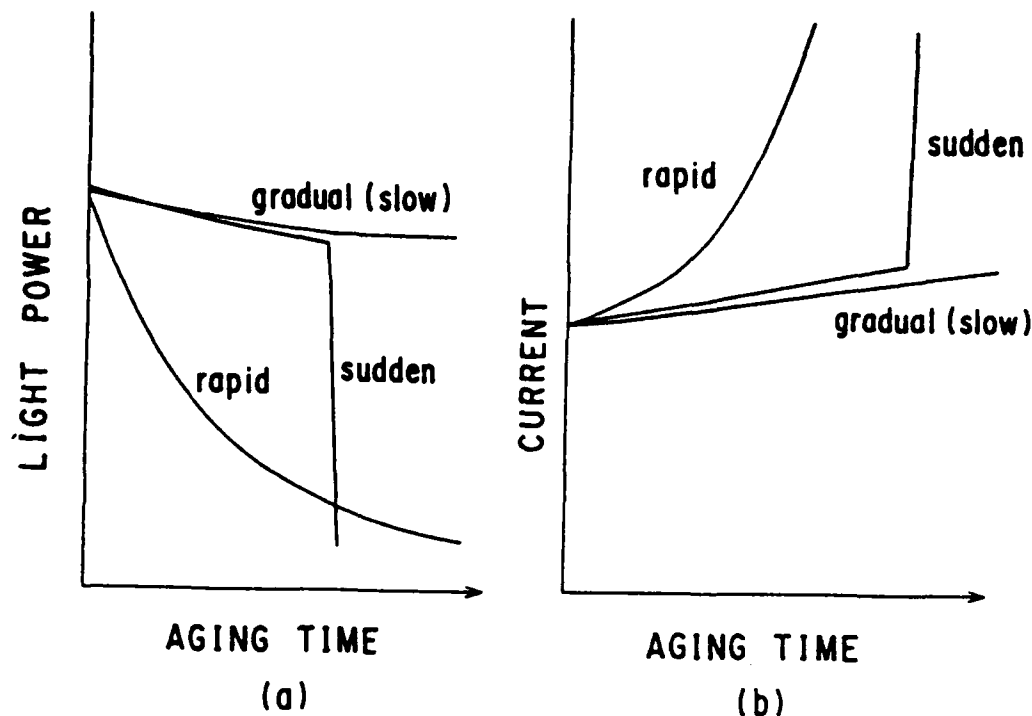


Fig. 1 (1:116) Typical degradation modes.

First a background is provided, outlining some of the basic theory describing dark defects. Following this, the work reports on the various strains of the dark defects observed in semiconductor lasers. Then their mode of motion is described. Next the characteristics that govern the growth of dark defects are detailed. After this, a qualitative/quantitative overview of the dark defects' influences on the device's other operating characteristics is presented. Finally a summary and observations on how to reduce the dark defects' degradation on a lasing device are offered.

II.1.2. Background. Crystals contain imperfections that disturb the local periodic arrangement of the atoms. These imperfections serve as sites for nonradiative recombination in a laser which is directly related to device degradation. Simply put, if more power is required to fuel nonradiative recombination, then less power is available for lasing. Also, nonradiative recombination processes typically dissipate the power via phonons. These vibrational energy packets heat the lattice and are therefore capable of melting the local structure if enough power is available. This leads to more defects

enhancing the nonradiative recombination process as a whole. The defects change the tight binding state of the electron and the atom, providing a continuum of energy states between the valence and conduction bands. Through the continuum of states, electrons and holes recombine nonradiatively.

To understand the evolution of dark defects, an examination of the crystal defects is in order. Such imperfections may be point, line and plane defects (1:118). Point defects typically are due to either a vacancy site or an interstitial atom. (Fig. 2(a)) The plane defect is typically a stacking fault in which the regular sequence of a stack of identical atom layers is locally interrupted in the crystal. By interrupted, it is meant that a region of the layer may have a portion missing (intrinsic), or may only exist over a local region (extrinsic). Both are shown in Fig. 2(b).

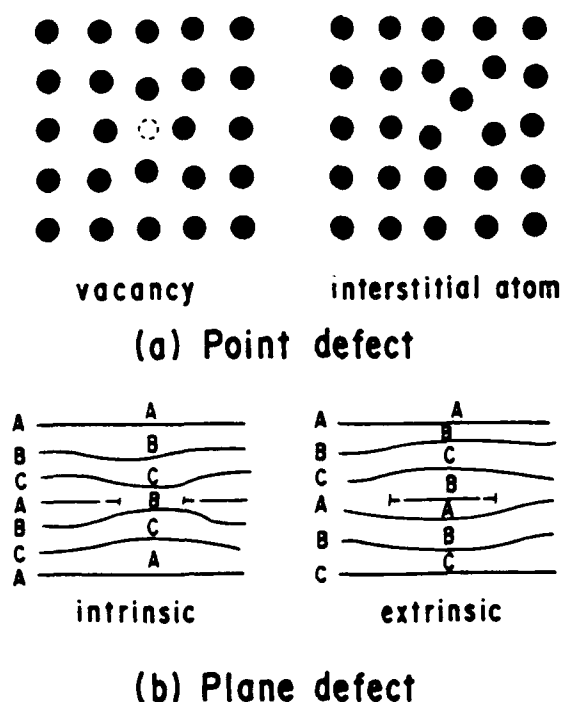


Fig. 2 (1:119) Basic concept of (a) point defect and (b) plane defect.

The line defect is a region of the crystal that is severely distorted and results from a lattice slip or the boundary between slipped and un-slipped parts in the crystal. A vector known as the Burger's vector is used to indicate the strength and direction of the lattice slip. Two cases of line defects are the edge dislocation and screw dislocation. As illustrated in Fig. 3, the edge dislocation occurs when the direction of the slip, and hence the Burger's vector, is perpendicular to the dislocation line. A screw dislocation arises when the slip direction is parallel to the dislocation line and the Burger's vector. A dislocation line can also occur that incorporates the edge and screw dislocation simultaneously. This is called a mixed dislocation line and will lie at an angle to the Burger's vector as determined by the lattice constants of the structure. Dislocation lines can't end inside the crystal. As a result, dislocation lines form closed loops, branch into other dislocations, or end at the surface and grain boundaries. Thus dislocation lines will generally combine to form complex dislocation networks.

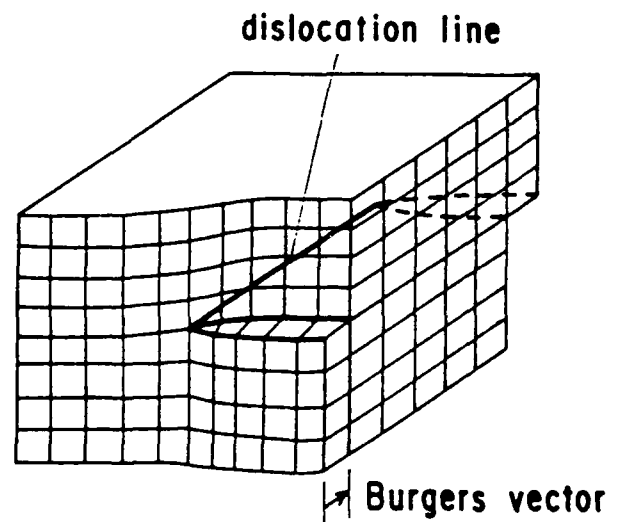
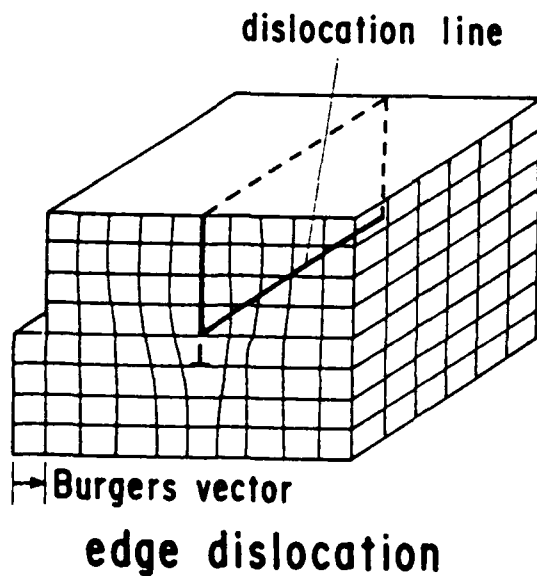


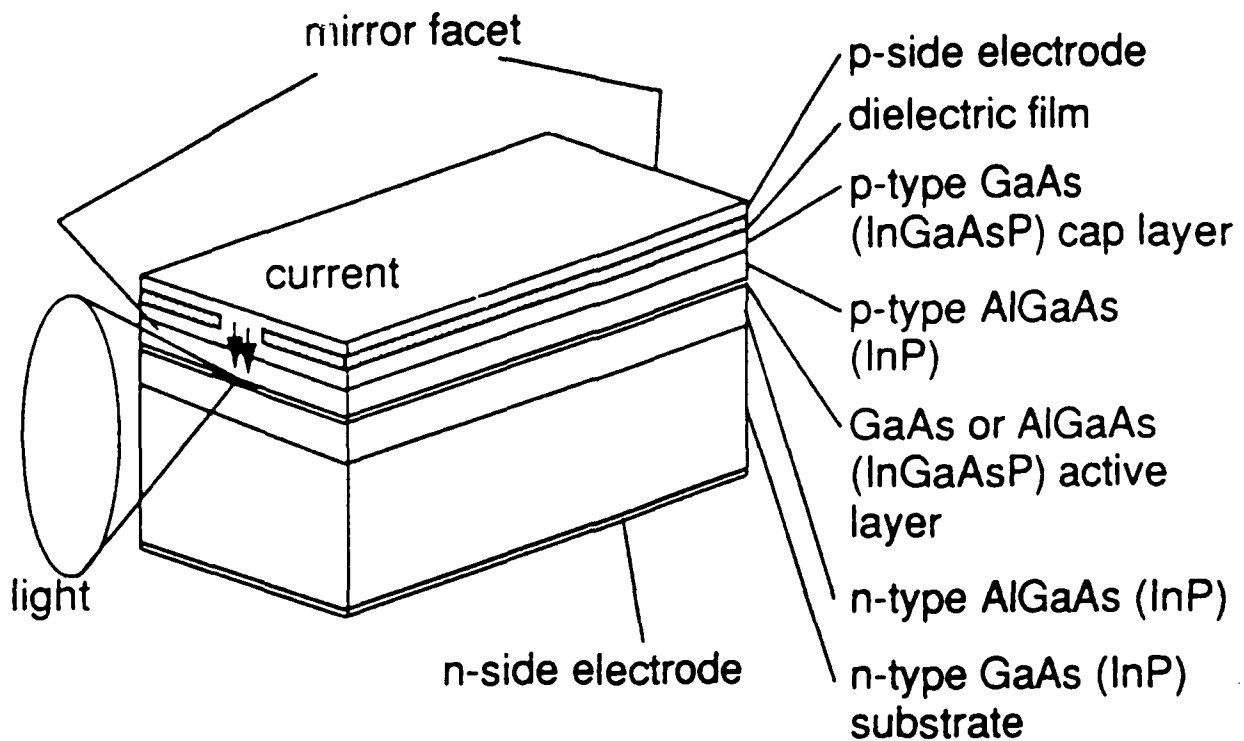
Fig. 3 (1:120) Basic concepts of line defects

During operation, nonradiative recombination at these defects will create added stress to the already locally stressed structure providing vibrational energy which causes the defects to shift and grow. The next section addresses the common traits inherent to change in defects change during operation. But first, two classes of lasers are introduced.

Two laser models repeatedly serve as the references for the lasers analyzed in the studies. The first structure to be outlined is the Fabry-Perot, or planar, laser. The second model, the multiple quantum well (MQW) laser, is a variation on the first.

The Fabry-Perot (FP) laser is illustrated in Fig. 4, which shows a cross section of each layer. On the bottom side of a n-type GaAs substrate, there is an electrode covering the entire surface. On top of the substrate, progressing away from the substrate, there is a heavily doped n-type AlGaAs layer, an intrinsic GaAs layer serving as the active layer, then a heavily doped p-type AlGaAs layer, and a p-type GaAs cap layer. On top of these layers, there is a dielectric layer with a narrow strip exposing the cap layer. The top layer is the p-side electrode which makes an ohmic contact along the narrow exposed strip through the dielectric layer. The structure is cleaved along lattice planes, usually a $\{011\}$ plane, normal to the strip contact. This cleaving forms facets which serve as the active cavity's mirrors. Since the doped layers above and below the active region have lower refractive indices than the active region, the EM radiation is optically confined to the gain region. A Fabry-Perot type optical cavity is formed by the two mirror facets and the active layer, hence this is known as a Fabry-Perot type laser. Variations on this structure include grading the relative amounts of the aluminum and gallium in the doped layers to improve optical confinement and coating the facets with dielectric layers, typically Al_2O_3 , to increase the reflectivity and reduce oxidation of the mirrors.

The quantum well (QW) laser is based on the FP laser and its characteristics can be understood on the basis of FP lasers. The structure is quite similar to the FP laser except in the active layer. The active layer thickness for a quantum well is on the order of the de Broglie wavelength, $\lambda = h / p$. Here h is Planck's constant and p is the photon's



() for InGaAsP/InP laser

Fig. 4 (1:44) Basic structure of a planar-type semiconductor laser.

momentum. This narrow thickness restricts the motion of the injected carrier in the direction perpendicular to the thin layer. The kinetic energy is quantized into discrete energy levels. The thickness of the active layer is typically less than a few tens of nanometers. Devices containing this feature are called QW structures, in which the thin region is called the potential well and adjacent thicker regions are known as potential barriers. A laser having a single thin region is known as single quantum well (SQW), and if there are alternating thick and thin regions in the active layer, it is known as a multiple quantum well laser (MQW). Fig. 5 displays the band structure of the active layer of a MQW laser. In actual QW lasers, optical and carrier confinement can be increased by employing graded index waveguides, the doped layers, as explained in the FP description. MQW lasers also inherently have better optical confinement than SQW lasers. These improved structures can require a lower current to trigger lasing. This amount of current,

known as the lasing threshold current, is typically one-half to one-third that of a FP laser. The extent to which threshold current changes under operation serves as one measure of the degradation of the laser.

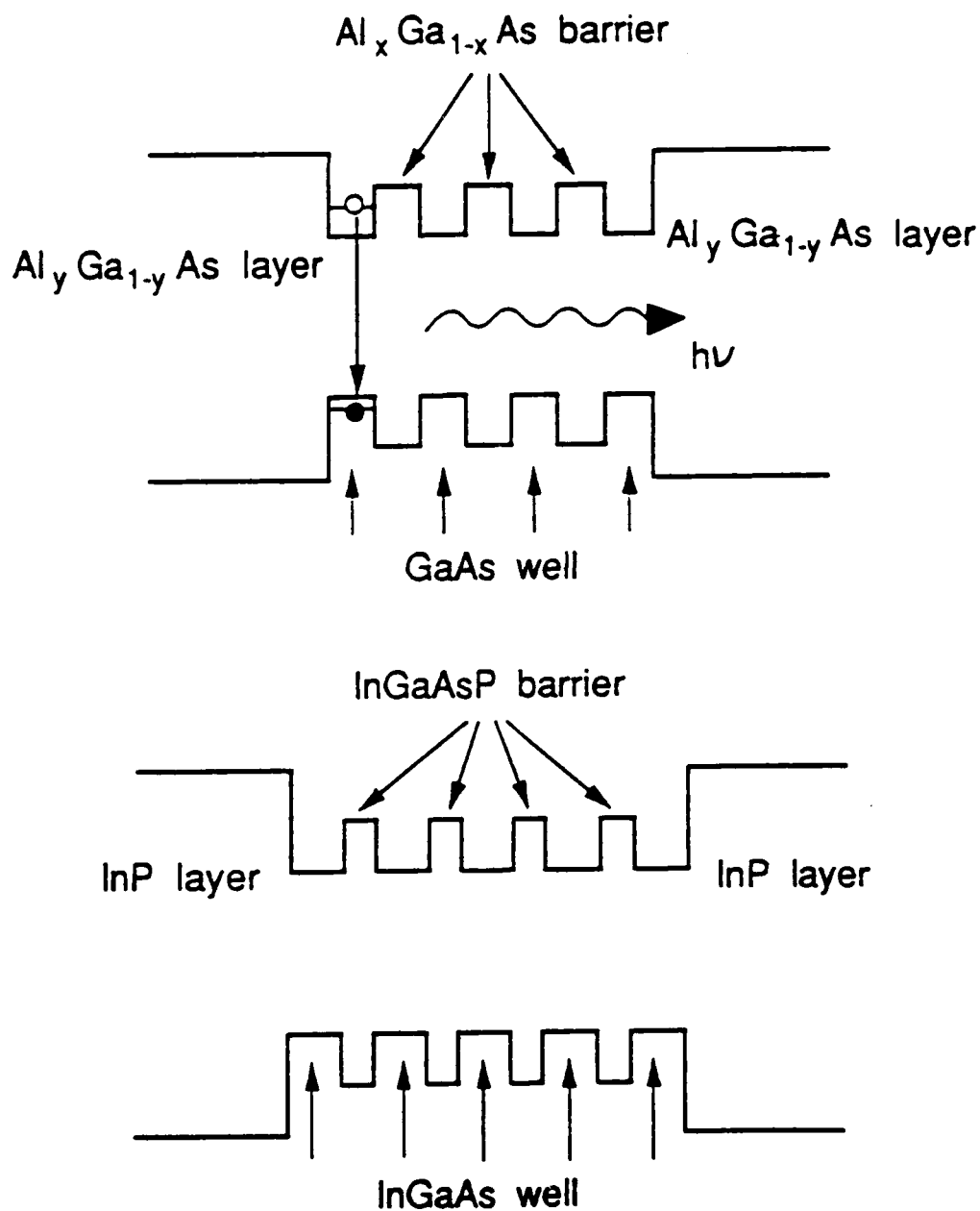


Fig. 5 (1:77) Multiple structure of AlGaAs/GaAs (four well) and InGaAs/InGaAsP (five well active layer).

II.1.3. Types of Dark Defects. The most elemental dark defect is the dark spot defect (DSD). Fukuda et al. studied the generation of the DSD in an early effort to quantify its influence on a laser (5:L87). Their first goal was to ascertain that DSDs corresponded to crystal defects. After operating a laser until DSDs could be observed via electroluminescent (EL) observation, they selectively etched off layer by layer of the sample. First the p-side electrode was removed, and the surface of InGaAsP cap layer was smooth. The cap layer was etched off, but the p-side cladding layer in the degraded sample had no features correlating to the EL topographical map. Next the active layer was etched through. The etch pits on the heteroboundary of the active layer and the n-side cladding layer completely correlated with the DSDs in the corresponding EL topographical map. Upon further layer removal, this correlation diminished rapidly and the etch pit density dropped significantly from the density near the active layer. This study demonstrated that the DSD phenomena arises from crystal defects in the active layer of a laser.

Fukuda et al. also modeled the evolution of the DSDs in laser operation (4:1246). The structures analyzed lased at 1.29 and 1.55 micrometers. They began by preselecting samples free of DSD's or DLD's as observed by EL. A qualifier needed here is that while the samples were free of the DSD's they were not free of the origins that would generate the DSD's. In other words, some samples contained crystal defects outside the active region so they would not initially act as DSDs. Assuming that defect generation would depend on current and junction temperature, device aging was carried out at forward current densities of 5, 10, and 15 kA/cm² and junction temperatures of about 30, 130, 250°C. Fig. 6 shows the generation time of the first DSD, t_d , and the operating current density. The junction temperatures of samples were adjusted to be between 120 and 140°C by changing the ambient temperature. The generation time of the first DSD

strongly depended on current density, and it can be expressed approximately by the following relation:

$$t_d \propto \exp(-AJ^2), \quad (2.1)$$

where J is the injected current density and A is a constant. Fig. 7 (4:1249) graphs the generation time for the first DSD as a function of temperature. For the range of variables, it is clear that the generation time mainly depends on the injected current densities.

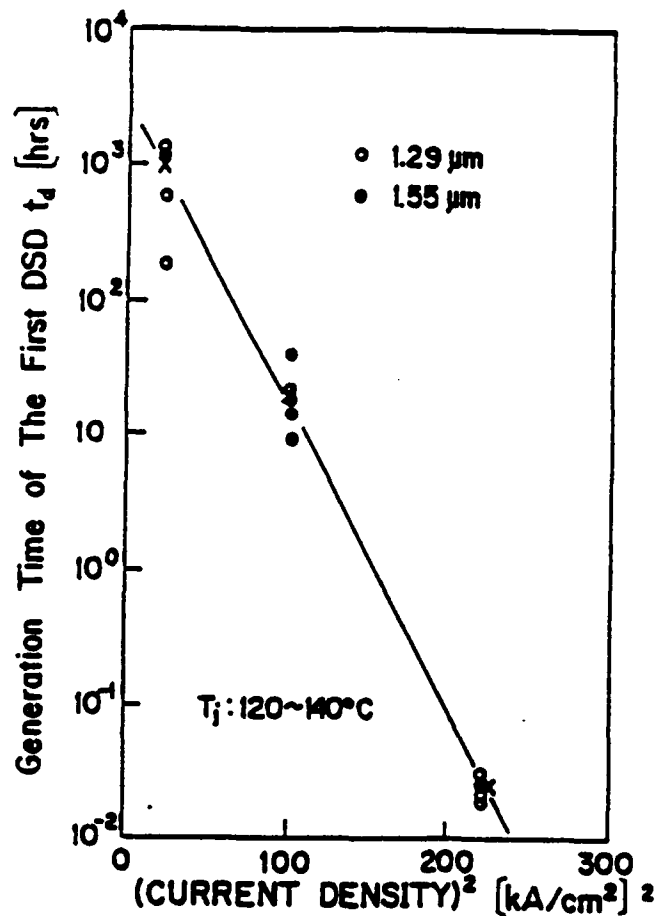


Fig. 6 (4:1248) Generation time of the first DSD as a function of the square of current densities under junction temperature of $120\text{--}140^\circ\text{C}$. Cross point (X) is the median generation time of the first DSD for each aging condition. (Wavelengths: $\lambda = 1.29 \mu\text{m}$, $\lambda = 1.55 \mu\text{m}$).

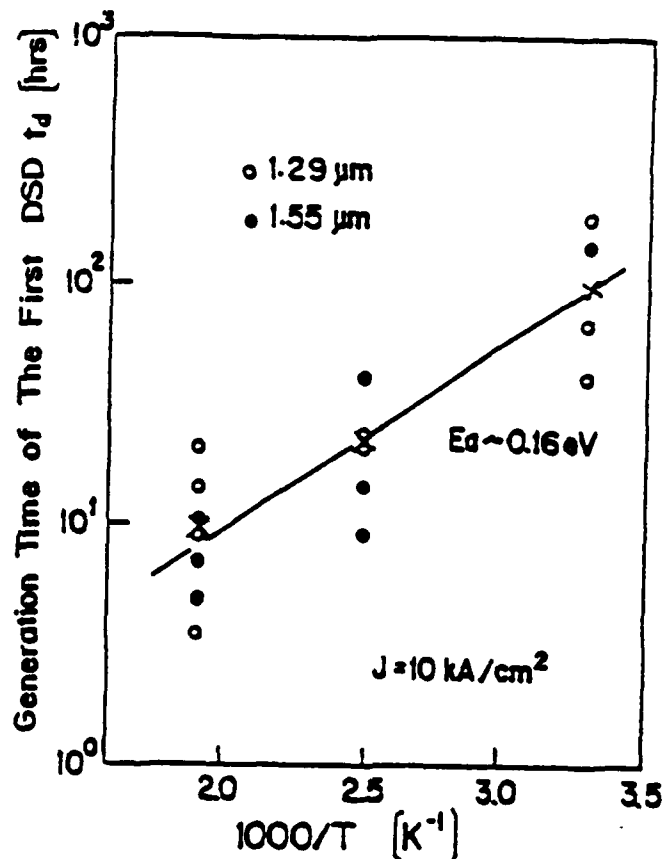


Fig. 7 (4:1249) Generation time of the first DSD as a function of the junction temperature under current density of 10 kA/cm. Cross point (X) is the median generation time for the first DSD for each condition.

While M. Fukuda et al. studied DSDs they were careful to note that dark line defects (DLDs) were not very common under their testing environment, other studies more interested in DLDs took to testing an inherently more stressed structure, a GaAs laser on a silicon substrate (7:791). Their actual goal was to try various filtering mechanisms on Si substrate to reduce the density of threading dislocations and determine if the substrate could be used as a viable alternative to GaAs. The threading dislocations would serve as nonradiative recombination centers and thus DLDs. The threading dislocation develops during processing and, if it grows through the active layer of the laser, will grow and

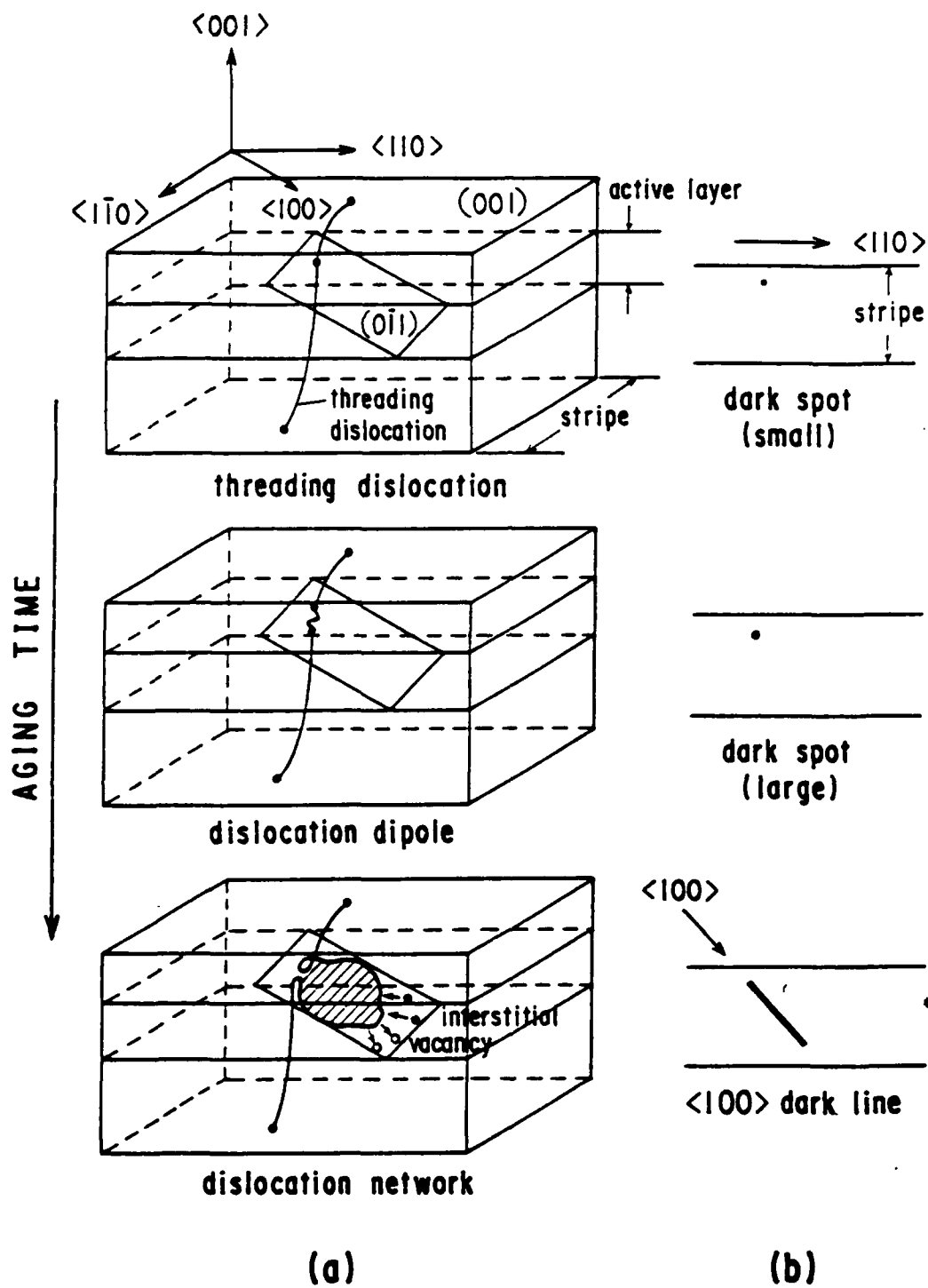


Fig. 8 (1:123) (a) Elongating mechanism of <100> DLD; (b) Electro-luminescent (EL) pattern

develop from a DSD to a DLD. The details to actual growth and motion of defects are presented later. Fig. 8 shows how a threading dislocation evolves into a DLD with "aging" time, the time of normal operation. The study revealed that while thermal cycle annealing and strained-layer superlattices are effective in reducing the threading dislocation density, even the best structures still degraded rapidly when compared to a GaAs substrate.

Another study analyzing dark defects attributed the mechanism to arsenic-out diffusion (8:2260). An EL graph of several active regions after removal of a portion of the n-side metallization revealed a number of DSDs and DLDs, collectively referred to as dark area defects (DADs). Examination of the p-side of the wafers revealed numerous small gallium rich/arsenic deficient depressions. These local deficiencies are believed to have formed during fabrication, forming localized concentration gradients which encourage Arsenic-out diffusion from the active layer. Upon comparing figures of the EL graphs to figures of the depressions, the depressions projected onto DADs in the active layer. To further support the cause of the defects, an EL micrograph was taken of an active layer. Then, comparing a "good" spot to a degraded spot, the elemental composition of both were analyzed. The arsenic concentration at the degraded point was below the correct stoichiometric concentration in the p-confinement and cap layer. The concentration gradually decreased from the vicinity of the active region to the cap layer. This gradual decrease indicated a diffusion process.

Another defect structure found in research is the worm-like defect structure. This structure initiates from a mirror facet and propagates to the center of the cavity. Using the TEM micrographs, a circular black spot, appearing at the tip of each worm-like defect, is believed to be a metal-rich droplet approximately $0.15\mu\text{m}$ in diameter (Fig. 9). A large dissipation of nonradiative recombination by surface recombination or previous dark defects results in a localized melting at the surface of the facet. The evaporation of the group-V elements leaves a metal rich droplet which melts all material it touches. As the source of this energy comes from the laser beam, the melting interface between the metal

and the lattice progresses toward the center of the cavity. On the backside of the metal drop, the metal is shadowing the material from more energy deposition and with a relatively cooler temperature the materials begin to solidify. The defective boundary between the resolidified material gives rise to the worm-like structure seen in the TEM. Crystal defects initially contained in the active region could also generate this structure but the tell tale-signature, the metal rich droplet, would not be present, which makes observation of the progress of the defect more difficult.

Another study verified the influence of facet defects on laser operation (10:211). Upon analyzing a graded index separate confinement heterostructure single quantum well (GRINSCH-SQW) with a single low reflective (<10%) facet coating, the authors detected

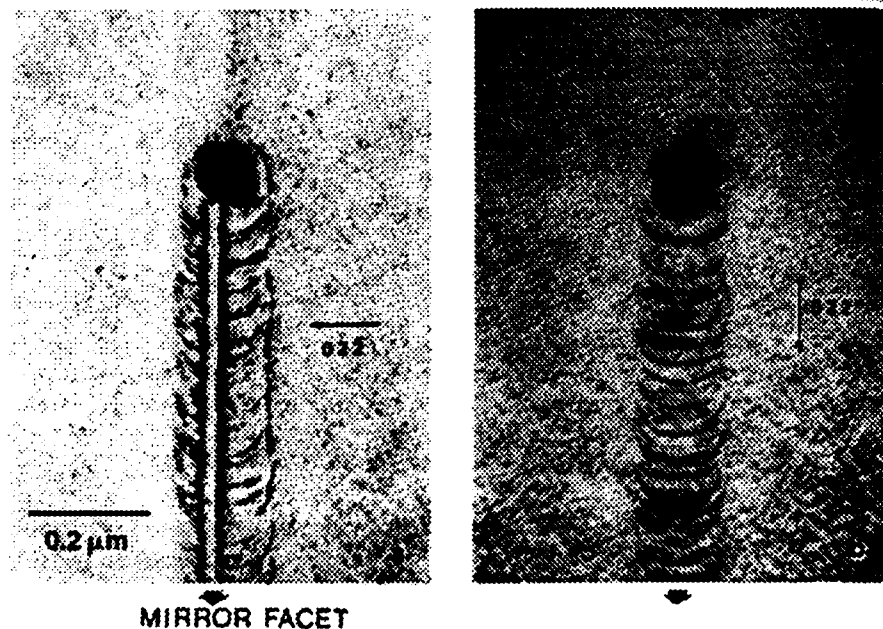


Fig. 9 (9:620) TEM top-view micrographs of worm-like defects. The dark spots are metal-rich droplets propagated from the mirror facet.

a $\langle 110 \rangle$ DLD behind every facet defect. Some $\langle 110 \rangle$ DLD defects occurred that had no corresponding facet anomalies. These defects were caused by excessive pulse width of the driving current signal. This study also analyzed a ridge waveguide structure (Fig. 10) with low reflective ($<1\%$) facet coating on both ends. The interesting point here is that even if a damaged facet is not in contact with the active region, it can cause DLDs to the laser.

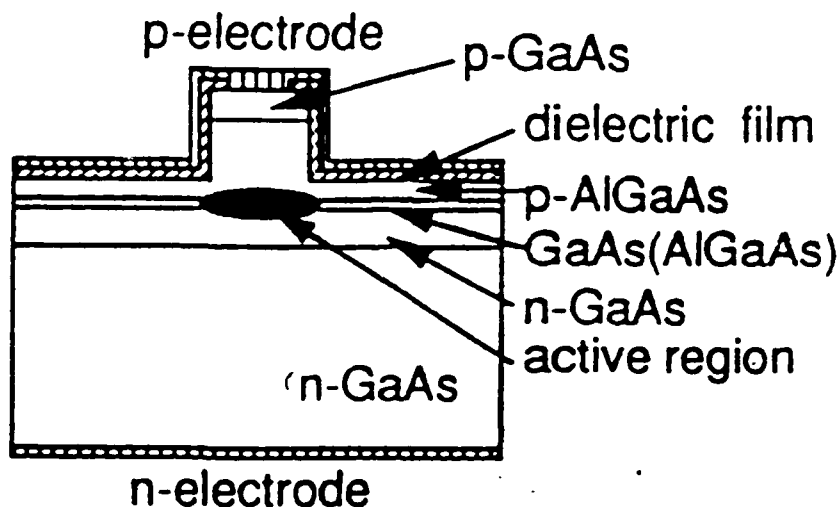


Fig. 10 (1:68) The basic structure for a ridge type laser.

II.1.4. Growth and Motion of Dark Defects. Line dislocations move by gliding or climbing (1:119). The Burger's vector is used to distinguish these motions. The dislocation line and Burger's vector form what's known as the slip plane. Gliding occurs when the dislocation line moves in this plane. In general, the slip plane is the plane with the highest density of atoms and the direction of motion is the direction in which the atoms are most closely spaced in the slip plane. Plastic deformation will encourage this movement. Applying this to a III-V compound's zincblende lattice, this means that gliding motion occurs in the (111) plane and in the $\langle 110 \rangle$ direction, as the earlier mentioned studies will confirm (1,9). The velocity of the gliding motion has been shown to increase inversely with the bonding energy between atoms, and therefore, the bandgap energy.

Climbing occurs when the dislocation moves out of the slip plane and perpendicular to the Burger's vector. The motion requires additional atoms or a vacancy in the dislocation line in order to move out of the slip plane. Therefore, unless a diffusion of atoms is in process, the climbing motion is difficult and requires thermal activation. The entire dislocation does not climb. The movement occurs a bit at a time through what is called a jog (Fig. 11). The jogs themselves can be treated as edge dislocations of one lattice space.

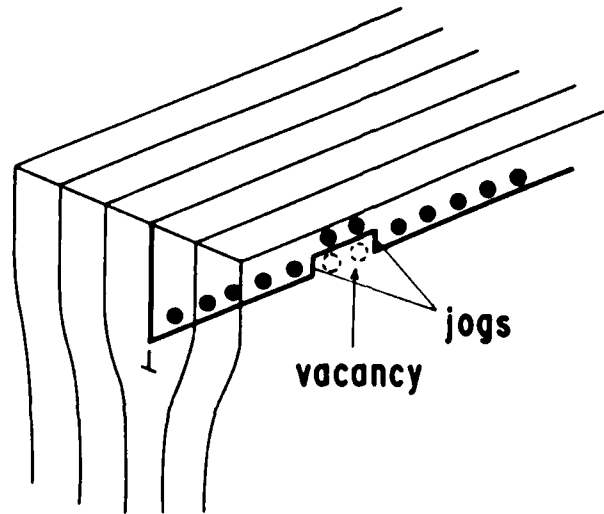


Fig. 11 (1:121) Concept of the climbing motion process.

Now that it is known that defects can move, what causes such motion? Given an initial threading dislocation having continued from the substrate or a stacking fault and passed through the active layer, one would initially see a DSD. As this is a center of nonradiative absorption, the growing heat will deform the thread into a dislocation dipole. upon further aging, the dipole will form a network elongating in the active layer. In this situation, a DLD can be observed in an EL topograph. This elongation will always elongate in the $\langle 100 \rangle$ direction by observation from the direction perpendicular to the active layer (001) plane.

A more prevalent DLD is the $\langle 110 \rangle$ DLD. This growth will be triggered by any anomaly. If no threading dislocations are in the active region initially, a dislocation from

the surface, for example, a facet, may provide one and the natural gliding motion of the defect will cause DLD growth. Thus, the DLD will elongate in the (111) slip plane and its projection to the (001) plane will appear as a $\langle 110 \rangle$ DLD. In aging a FP laser with an active layer of InGaAsP of 10-15 X 200 X 0.2 micrometers at 10 kA/cm² and 250°C, the development speed of such defects was 0.3 micrometers per hour (5:L87).

II.1.5. Variables Influencing Dark Defect Degradation. Two characteristics of dark defects have already been addressed, the orientation of their growth and the time required for the first dark defect, a DSD, to be generated in a laser. The first trait depends obviously on the lattice structure and the second characteristic has been shown to depend primarily on current density and only slightly on temperature. A highly related characteristic is the possible dependence of the growth of DLDs on temperature and current. M. Fukuda et al. researched this topic by first baking 8 samples at 250°C for 200-300 hours without operation (3). The pulse threshold current never changed and no dark defects were observed. Then they operated 2 samples at 10 kA/cm² and 120-130°C, the lasers degraded at the same rate as samples run at 10 kA/cm² and 250°C. Finally, 5 samples were operated at 5 kA/cm² and 120-130°C and only a few DSDs were observed after 1000 hours. The pulse threshold current for these samples hardly changed. These results strongly indicate that the growth of dark defects depends strongly on operating current density and only weakly on the junction temperature.

Another variable uncovered involved the facet heating resulting from the duty cycle of the operating current (10:212). Defects that had not been attributed to facet defects implied that the devices being evaluated were operated at either too high an optical power or with an excessively long pulse width in the power vs. current curve measurement. A longer pulse width leads to more energy being applied to facet heating. By increasing the duty cycle and shortening the pulse width the authors effectively reduced degradation from this mechanism. As a larger duty cycle results in more junction heating and a longer pulse

width results in greater facet heating, it was concluded that the rate of degradation was dependent on facet heating.

The density of threading dislocations has also been shown to influence the rate of degeneration. Returning to the study involving a Si substrate with a GaAs based laser, it was observed that the degeneration rate could be improved by annealing and by implementing a strained superlattice (7:793). These processes effectively reduced the threading dislocation density to improve the degradation rate. Nonetheless, one reason the degradation rate was still rapid compared to a GaAs substrate is that the laser built on top of a substrate of similar material was inherently less prone to crystal defects and thus had a lower threading dislocation density than even the best of the structures on the Si substrate. The studies involving the BH lasers also anticipated influence by the threading dislocation density (9:612). Having found that point defect clusters or small precipitates usually can be revealed by selective etching as saucer pits, examination exposed a high density of such pits in the samples studied. However, a clear correlation between the etch pit density and the device degradation could not be ascertained.

In an effort to model the degradation behavior of lasers, Martins et al. outlined the influence of electron beam irradiation doses on device evolution (11:554). As a check on their efforts, all measurements were redundantly obtained from both electron-beam-induced current (EBIC) and nondispersive cathodoluminescence (CL) signal profiles. All devices were irradiated at 600 A/cm^2 and results were compared to a parallel set of devices running under continuous wave conditions. From previous work, it was known that the profiles would exhibit the following characteristics: (i) The EBIC signal and the width of the EBIC profile increases with increasing irradiation dose. (ii) The CL signal from the active and buffer layers decreases with increasing irradiation dose. (iii) The initial CL and EBIC profiles can be recovered when the degraded sample is directly biased.

Measurements were based on the external voltage necessary to recover the initial, non-degraded profiles. These values were used to evaluate the donor concentration in the

upper cladding layer as a function of irradiance dose. The donor concentration, having been changed by nonradiative recombination and leading to dark defects, in turn served as the measure of degradation. Fig. 12 gives the profiles for the two types of SQW lasers compared, one on a Si substrate and the other on a GaAs substrate. Just to give rough numbers, under an equivalent irradiation of 1.6 A/cm^2 , the GaAs/Si lasers began degrading at 2 minutes and for the GaAs/GaAs lasers, degradation began at 14 minutes. After degrading devices by uniform irradiation, local irradiation (only irradiating the laser structure on the Si substrate), and continuous wave operation, it was concluded that local irradiation and continuous wave operation suffered parallel degradation. Fig. 13 shows the profiles for uniform irradiation and Fig. 14 shows the profiles for both continuous operation and local irradiation.

The result of this study demonstrated the following relation (in the upper cladding layer) (11:558):

$$\frac{n_f}{n_i} = 1 - \frac{V_r}{U_c} \quad (2.2)$$

where n_f is the final donor concentration, n_i is the initial donor concentration, U_c is the built-in potential, assumed constant, and V_r is the external bias needed to generate the original EBIC and CL profiles. Table I documents this relation with a U_c equal to 1.86 volts. The implanted vs. non-implanted distinction in the GaAs/Si arose from crystalline damage that occurred during fabrication and the analysis covers regions both affected and unaffected by the damage.

This report also generated a proposed degradation process that was summarized in three stages (11:559):

Initially, the depletion region changes due to the annihilation of Si donors (the dopant). This annihilation is proposed to be mainly due to the formation of a complex involving silicon bound to gallium and a vacancy in gallium: $\text{Si}_{\text{Ga}} + \text{V}_{\text{Ga}} \rightarrow [\text{Si}_{\text{Ga}}\text{-V}_{\text{Ga}}]$.

GaAs	(p+)(0.6μm)	GRIN-SCH
Ga _(0.5) Al _(0.5) As	(p)(1.2μm)	
Ga _(0.5) Al _(0.5) As to Ga _(0.8) Al _(0.2) As	(n)(2000Å)	
GaAs	(200Å)	
Ga _(0.8) Al _(0.2) As to Ga _(0.5) Al _(0.5) As	(n)(2000Å)	
Ga _(0.5) Al _(0.5) As	(n)(2.0μm)	
GaAs	(n+)(0.8μm)	
GaAs(substr.)	(n+)	

GaAs	(p+)(0.6μm)	GRIN-SCH
Ga _(0.5) Al _(0.5) As	(p)(1.1μm)	
Ga _(0.5) Al _(0.5) As to Ga _(0.8) Al _(0.2) As	(n)(2000Å)	
GaAs	(60Å)	
Ga _(0.8) Al _(0.2) As to Ga _(0.5) Al _(0.5) As	(n)(2000Å)	
Ga _(0.5) Al _(0.5) As	(n)(1.1μm)	
Ga _(0.5) Al _(0.5) As to GaAs	(n+)(0.5μm)	
GaAs(MBE)	(n+)(0.6μm)	
Si(substr.)	(n+)	

Fig. 12 (11:555) Schematic of the composition and thickness of the layers of the GRIN-SCH devices investigated.

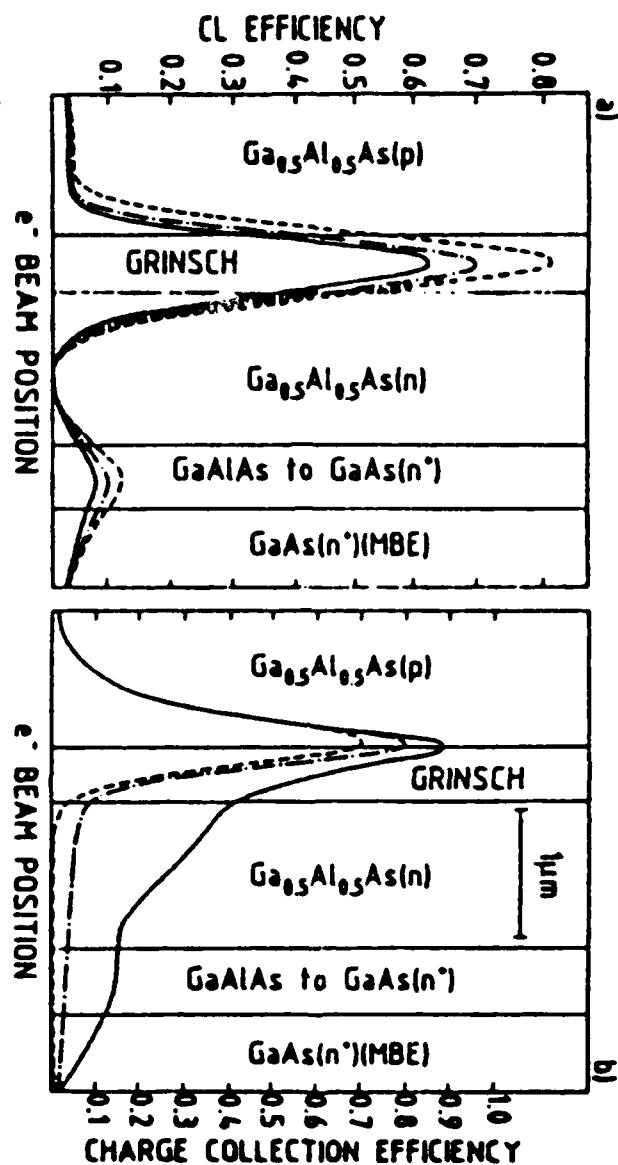


Fig. 13 (11:555) (a) CL and (b) EBIC profiles before (dashed lines) and after damage, for an intermediary (dot-dashed lines) and a final (solid lines) stage of degradation. These profiles were obtained by irradiating the whole surface of a nonimplanted GaAs/Si material.

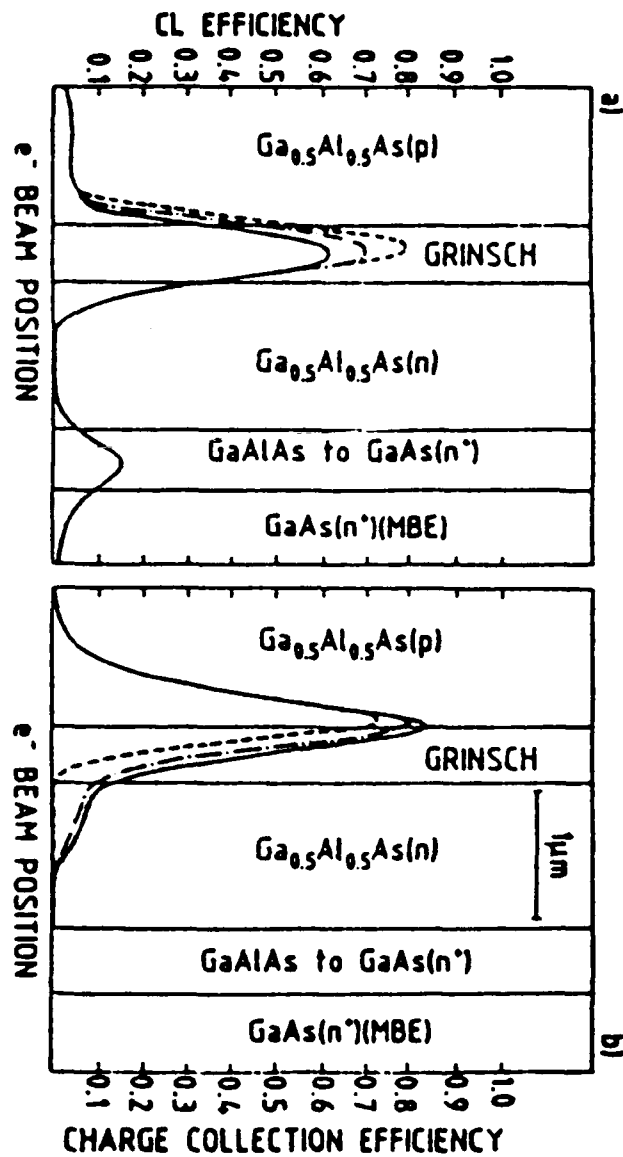


Fig. 14 (11:556) (a) CL and (b) EBIC profiles before (dashed lines) and after damage, for an intermediary (dot-dashed lines) and a final (solid lines) stage of degradation. These profiles were obtained by irradiating only the GRIN-SCH layers of a nonimplanted GaAs/Si material.

Sample	Irrad. dose ($\times 10^{21} e^- / \text{cm}^{-2}$)	V_{rec} (V)	N_f/N_i ($\pm 2\%$)
	3.6	...	1.00
GaAs/Si	6	0.50	0.73
(nonimplanted)	9	0.60	0.68
	3.6	0.40	0.78
GaAs/Si	6	1.00	0.46
(implanted)	9 ^a)	> 1.30	< 0.30
	4	...	1.00
GaAs/GaAs	8	0.40	0.78
	12	0.60	0.68

^aAt this stage, the applied bias necessary to recover the initial profiles was enough to reduce drastically the EBIC signal.

Table I (11:558) Ratio of annihilated donors (N_f/N_i) measured for different irradiation doses and for different materials. These values were deduced from the bias voltage necessary to recover the initial profiles.

This may serve as a deep electron trap and is promoted by an electrical field. The formation starts in the p-n junction and works towards the SQW.

The second stage begins when the complex formation reaches the active layer. The high density of carriers and photons enhance the process, generating more complexes and thus creating centers for nonradiative recombination. This is noticed externally by a drop in the quantum efficiency of the active layer. (More on this later.)

The third stage begins when the nonradiative recombination centers, the complexes, generate local heating. This causes the dislocations to glide and jump. With this, dark lines appear in the stressed region of the device.

These last two steps concur with Fukuda et al. in their study on current's and temperature's influence on degradation. In their description, degradation due to DLDs could be said to occur in two stages (4:1247). In the initial stage of DSD generation, the DSDs increase in number but do not absorb energy. In the second stage, no more DSDs are created but those that are present absorb light and increase in size, becoming the DLDs.

II.1.6. Dark Defects' Influence on Other Parameters. Up till now not much emphasis has been placed on how the devices' parameters change as a result of the dark defects. Dark defects affect factors such as local heating, currents, breakdown voltage, the spontaneous emission intensity, quantum efficiency, and material attenuation coefficients depend on the dark defect density and thus will change as the dark defects change. This section addresses studies analyzing the influence of dark defects on the lasing device's characteristics.

The first study, conducted by Kobayashi et al. demonstrated that local temperature rises, current crowding, and lower breakdown voltages were present near the dark line defects, when these values were compared to those of a sound region of a device (3:508). The reasoning is that, since virtually all electric power supplied is converted to heat and the current density is locally high, local heating will occur, even if current is insufficient to support lasing. To emphasize the current crowding, all measurements were carried out below the lasing threshold and thereby remove the temperature rise due to absorption of laser radiation. The study measured current and temperature distribution profiles by tracing the thermal radiation of infrared (TIR) and electroluminescence (EL) to a resolution of 5 micrometers. Fig. 15 displays the temperature distribution profiles along the active stripe of a laser. The solid curve (1) is the temperature profile for the forward current of 130mA, and the curves (2) and (3) are the profiles for the reverse current of 1mA and 4.8mA respectively. Note the correlation of local temperature maximums to EL minimums of the broken curve measured also at the forward current of 130mA. Also just below the graphs, note that the dark spots evident during lasing, correlate to the

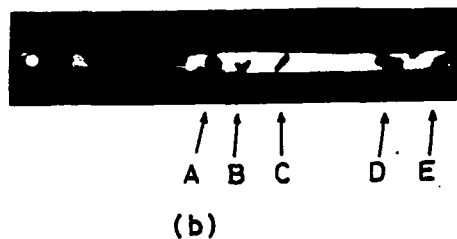
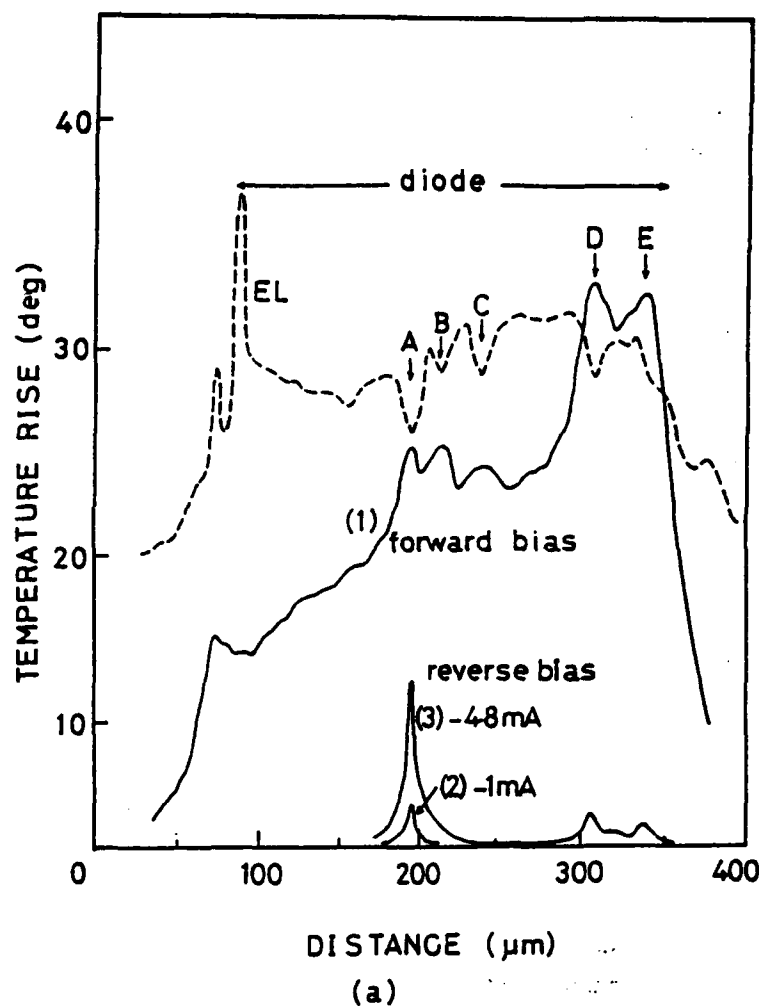


Fig. 15 (3:510) (a) The temperature distribution profiles along the stripe. The solid curve (1) is the temperature profile for the forward current of 130mA, and the curves (2) and (3) are the profiles for the reverse current of 1mA and 4.8mA, respectively. The broken curve shows the EL intensity distribution in which the dark lines (A) through (E) are indicated by arrows. Nonlinear scale of the ordinate comes from the nonlinear dependence of the detector on ΔT . (b) The EL pattern of the degraded diode observed through the n-type GaAs substrate. The dark lines(A) through (E) are indicated by arrows.

temperature hot spots. There are two possibilities for the observed non-uniform temperatures distribution. The first is the non-uniform current density along the stripe and the other is the development of thermal resistance during degradation. From previous discussion, we know that the dark regions are contained in the active region and that they provide a continuum of permitted energy states for the carriers to run recombine nonradiatively. Thus a non-uniform current density is more likely. The other explanation would require the defect network to continue through the cladding layers above and below, providing higher thermal resistance to surround the cavity and thus contain the thermal energy.

The next figure (Fig. 16) shows an example of the successive change of temperature distribution pattern observed at constant dc forward current of 130mA. The conditions of each degradation step are given in Table II. After the first step of degradation (D1), dark lines are observed in regions A and B and these correspond to the local hot spots of the EL profile. During the next step of degradation, the dark lines grew and the temperature rose accordingly (D2). After the third step, the network at B suddenly changed to become the path of least resistance. Thus, with a constant current source, the current distribution adjusted to the region with the lowest breakdown voltage and the temperature distribution adjusted in suite. Thus the network at A became cooler than either of the previous steps. An extension of what occurred at B can follow. With continued degradation, the network can burn a complete path through the active region, this will in effect short circuit the active region and thus virtually all current will flow here to generate one temperature peak much hotter than the remainder of the active layer.

A final observation made from this study was that the current density at the dark network will typically be twice that of an undegraded region. This will hold until the fatal degradation, the point when a dark network shorts the active region.

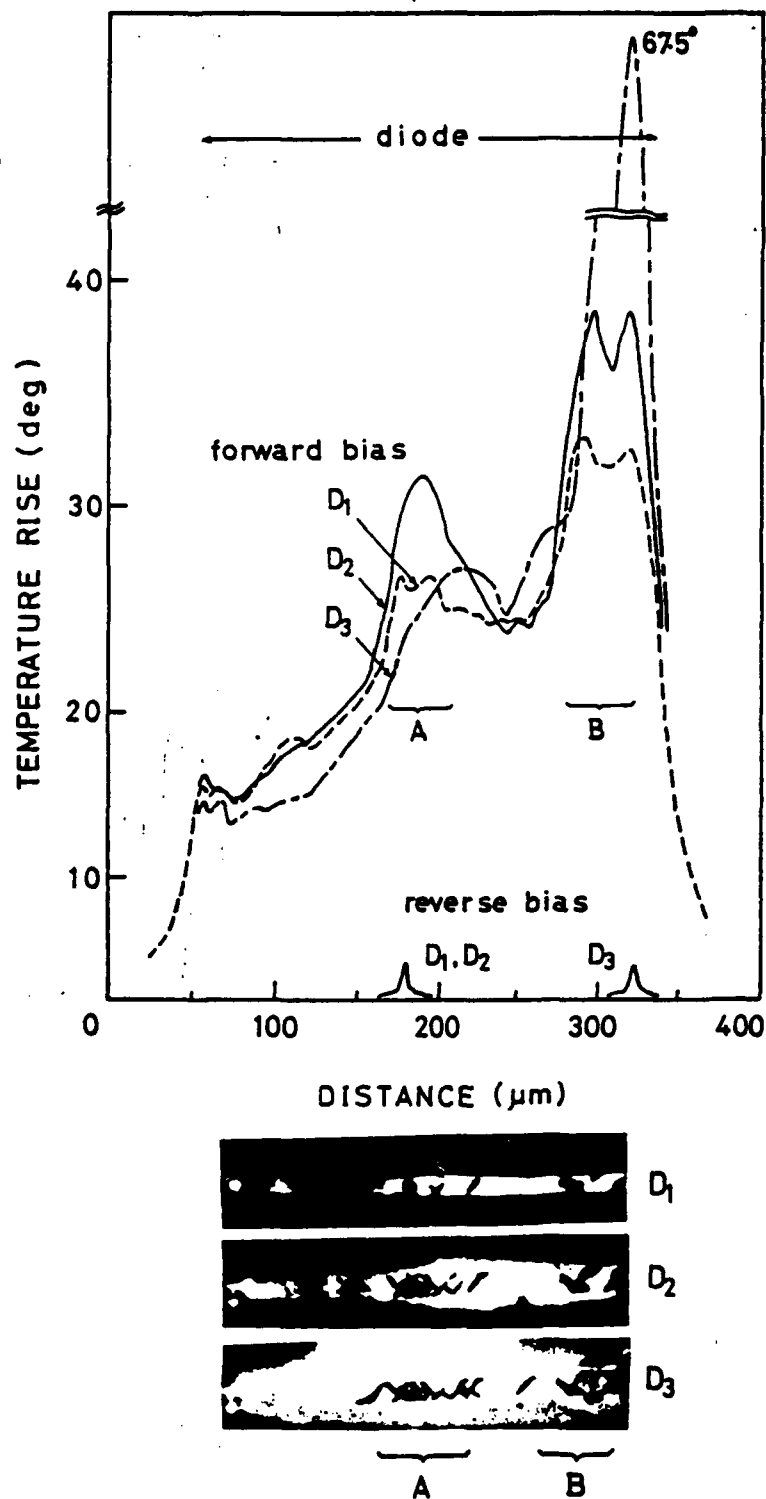


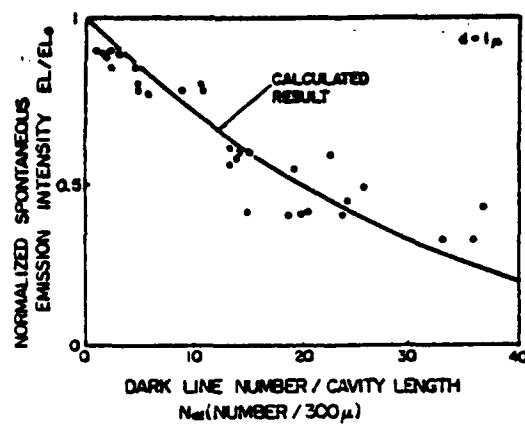
Fig. 16 (3:511) The change of temperature distribution profile and the EL pattern observed after the successive degradation. The broken, solid, and dot-dash curves are the profiles observed after the degradation step D₁, D₂, and D₃ respectively. Scale of the ordinate is nonlinear.

The next study determined that with degradation, the increase of the threshold current density from increased cavity loss and the decrease of the gain coefficient attributed to more dark lines in a form of positive feedback to enhance degradation (12:835). Before and after degradation, the current density and the external quantum efficiency were measured. After repeated measurements of several samples, the study plotted the spontaneous emission intensity (for this study EL) after and before degradation (EL/EL_0), the threshold current density, normalized to before degradation (J_{th}/J_{th0}), and the external differential quantum efficiency, normalized to before degradation (η_d/η_{d0}), all as a function of the number of dark lines/cavity length. All are shown in Fig. 17. As can be observed from the graphs, with an increase in dark line density, the threshold current density increases, the spontaneous emission intensity and the external differential quantum efficiency decrease.

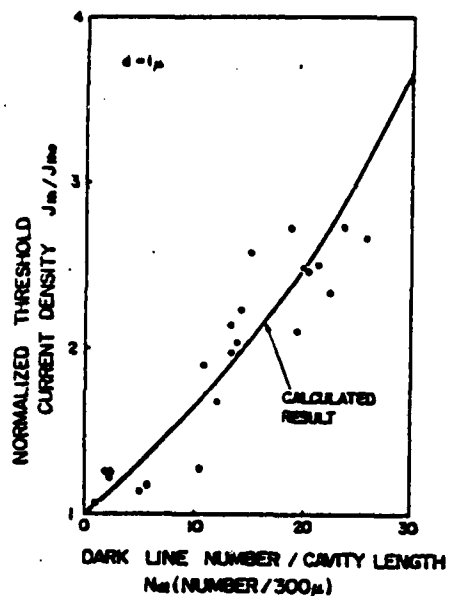
Degradation step	Condition of the degradation		Pulse threshold current*
	DC current	(operation time)	
Initial			138 mA
D ₁	235 mA (5 minutes), 284 mA (9 minutes), and 344 mA (2 minutes)		350 mA
D ₂	198 mA (7 minutes) and 357 mA (15 minutes)		730 mA
D ₃	200 mA (3 hours), 366 mA (2.5 hours), and 500 mA (2 hours)		4000 mA

*The threshold current after each step was measured by a 100 nsec current pulse at a repetition rate of about 50 Hz.

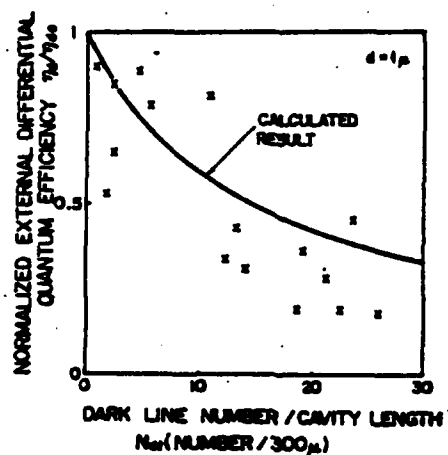
Table II (3:509) The conditions of the successive degradation steps.



(a)



(b)



(c)

Fig. 17 (12:837) Relations between degraded lasing characteristics and dark line numbers.

Solid lines are calculated results, (active layer thickness $d = 1\mu\text{m}$).

For the FP lasers analyzed, the relation between the increased threshold and the decreased spontaneous emission intensity in degraded lasers show that the two normalized quantities are approximately inversely proportional. Fig. 18 shows data points against a form fitted curve. The value "d" is the thickness of the active layer of the FP lasers.

Reasoning that more current was dissipated at the dark lines than the normal undegraded region, the study divided the total injected current into two components, that in the dark lines and that in the normal region. The study assumed that the current density in dark regions was some constant C times that of normal region (J_g) and that some portion of the length of the cavity was dark (L_a) where L was the total cavity length. Further assuming that there were some N_{d1} equivalent dark lines of width W_a , a sum of these current densities gains the relation (12:838):

$$J_t = \left(1 + (C - 1) \frac{L_a}{L} \right) J_g \quad (2.3)$$

$$L_a = N_{d1} W_a \quad (2.4)$$

where J_t is the average current density. In the dark line little or no spontaneous emission occurs. Therefore, the spontaneous emission intensity decreases with the increase of the number of dark lines. The degradation of the spontaneous emission intensity EL/EL_0 can easily be obtained from the ratio of the current injecting into normal regions after and before degradation (12:838).

$$\frac{EL}{EL_0} = 1 - \frac{L_a}{L} \cdot \frac{C}{\{1 + (C - 1)(L_a / L)\}} \quad (2.5)$$

This equation actually represents the upper limit of the spontaneous emission ratio.

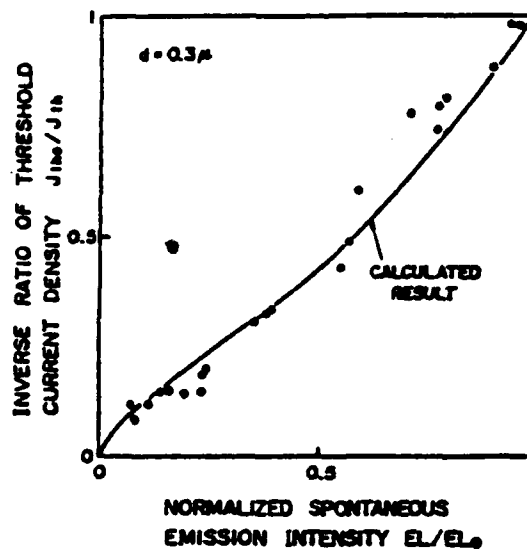
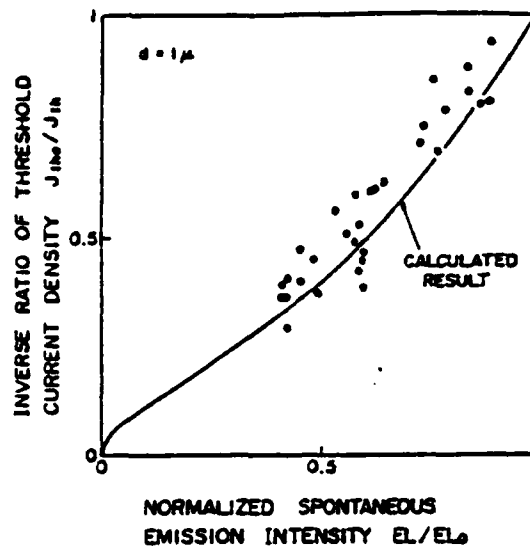


Fig. 18 (12:837) Relation between the increase of threshold current density and the decrease of spontaneous emission intensity, $d = 1$ micrometer, $d = 0.3$ micrometers.

When the dominant lasing mode is of the 0th mode, which is mostly in the active layer, we can obtain the threshold current density where the field is amplified in an exponential form. In defining α_a and α_g as amplification factors of the exponent in the effective absorption region (i.e. dark region) and in the normal region, respectively, the threshold condition of a laser having dark lines is written as (12:838),

$$2\alpha_a L_a + 2\alpha_g (L - L_a) = -\ln(1/R), \quad (2.6)$$

where R is the facet reflectivity. From equations (3), (4) and (6), threshold current density J_{th} is obtained in the following form with gain coefficient β_d and cavity loss α_d ,

$$\beta_d J_{th}^m = \alpha_d + \frac{\ln(1/R)}{L}, \quad (2.7)$$

$$\beta_d = \frac{\beta_b}{d^m} / \left(1 + (C-1) \frac{L_a}{L} \right)^m \cdot \left(\frac{L - L_a}{L} \right), \quad (2.8)$$

$$\alpha_d = \alpha_{2deg} \cdot \left(\frac{L_a}{L} \right) + \alpha_{2nond} \cdot \left(\frac{L - L_a}{L} \right), \quad (2.9)$$

where β_b is the gain factor, "d" is the active layer thickness, "m" the power of current dependency on gain, α_{2deg} and α_{2nond} are the absorption coefficients for the dark line defect regions and normal regions respectively. Before degradation, where $L_a=0$ and $C=1$, gain coefficient β_d and cavity loss α_0 take the following forms,

$$\beta_d = \frac{\beta_b}{d^m}, \quad (2.10)$$

$$\alpha_0 = \alpha_2 f_c, \quad (2.11)$$

Thus, the ratio of the threshold current density after and before degradation is obtained from equations (7)-(11).

Cavity loss after degradation α_d depends on the number of dark lines. If it is assumed that, under stimulated emission, the life time of the injected carriers is sufficiently short compared to the nonradiative lifetime in the dark line, the internal quantum efficiency is nearly independent of the number of dark lines. (This can be strained for a large number of dark lines). Then the ratio of the external differential quantum efficiency after and before degradation η_d/η_{do} is determined by the difference of internal absorption and expressed as,

$$\frac{\eta_d}{\eta_{do}} = \left(1 + \frac{\alpha_0 L}{\ln(1/R)}\right) / \left(1 + \frac{\alpha_d L}{\ln(1/R)}\right), \quad (2.12)$$

Thus some of the parameters that model the operation of a laser have been listed and their dependence on dark defects highlighted.

II.1.7. Dark Defect Degradation Summary. This review has proceeded to describe what are known as dark defects in the realm of reliability and operation of semiconductor lasers. Degradation is the process of change in a device's operating parameters over its operational lifetime. Dark defects primarily influence the rapid change of these parameters of which some examples include the increase of the current density necessary to trigger lasing and the amount of current demanded to maintain a given radiation output.

The dark defects occur as a result of growing crystal imperfection. These crystal defects may occur as point, line, and plane defects. The defects may arise during fabrication, from damage incurred with handling, or from driving the device beyond its

material constraints. Defect networks may be treated as the superposition of the elemental defects.

During operation, these crystal defects disturb the tight energy band structure of a crystal and provide a continuum of energy levels for nonradiative combination to occur. This energy, typically emitted as vibrational energy and heat, will serve to further stress an already locally stressed region. Also, the energy devoted to this destructive process is energy taken from the radiative emissions, thus lowering the efficiency of the laser.

The primary influences on the growth of dark defects are the current density, of which it varies as the density squared, and the dangling bonds at material interfaces between dissimilar materials, especially the facets. As these regions upset the regular crystal structure, stressing the structure, little excitation is necessary to spur on further crystal anomalies. Fritz et al. demonstrated that by increasing the duty cycle and shortening the pulse width for a given output power one can slow the degradation due to facet heating (10:211). Other studies demonstrated that annealing layers and employing a strained superlattice one can reduce the threading dislocation density and in turn slow degradation (3:1246). Also using a silicon substrate for a III-V lasing device, being an inherently strained structure, will degrade laser performance significantly more quickly than if a III-V substrate is used.

The final emphasis of the review focused on the actual dependence of device operating parameters on the density of dark defects. Characteristics detailed included the temperature and current distribution profiles as they correlated to dark regions. Studies demonstrated that the current density of degraded regions roughly doubles that of undegraded regions until fatal degradation occurs and the device is effectively shorted out. Other parameters modeled included the spontaneous emission intensity (EL), the threshold current density (J_{th}) and the external quantum efficiency (η_d).

II.2. Facet Degradation

II.2.1. Introduction. The facet operational behavior of a semiconductor laser plays a fundamental role in the lifetime of the device. This section outlines research and development serving to characterize and improve the facets of semiconductor lasers. Facets function to transmit and reflect the lasing beam in a semiconductor laser. In order to extend the lifetime, studies have been conducted to model the variables influencing laser facets. A few of the more obvious variables include the intensity of optical power passing through the facet and the cross area of the facet. Other less obvious factors include dielectric coating over the facets, the chemical composition of regions adjacent to the facets, and pre-aging the laser at lower initial drive currents. The articles reviewed in this literature search fall into two general categories. The first papers, sections 2 and 3, study the characteristics inherent to the facets themselves. The second group of papers, sections 4 and 5, focus on the degradation and lifetime studies influenced primarily by facet breakdown.

II.2.2. Facet Heating. The first study, conducted by Yoo et al. (13:L1686), focused on the local temperature rise in the mirror facet of high-power InGaAsP/GaAs laser. Specifically, the study analyzed the influence of surface states on facet temperature rise and compared the InGaAsP/GaAs high powered laser to an AlGaAs/GaAs high powered laser. A lower temperature rise implies less facet damage and hence longer operation. After stressing the devices, the local temperature rise of the InGaAsP/GaAs lasers measured one order of magnitude smaller than the AlGaAs/GaAs lasers of similar dimensions. The InGaAsP/GaAs lasers even performed with lower temperature rises than AlGaAs/GaAs lasers with a protective coating over the facets (Fig. 19).

The authors cited the root cause of the facet heating as nonradiative recombination of excess carriers, generated by the driving current and the absorption of photons near the mirror facet. The high surface recombination rate of the AlGaAs lasers likely results from

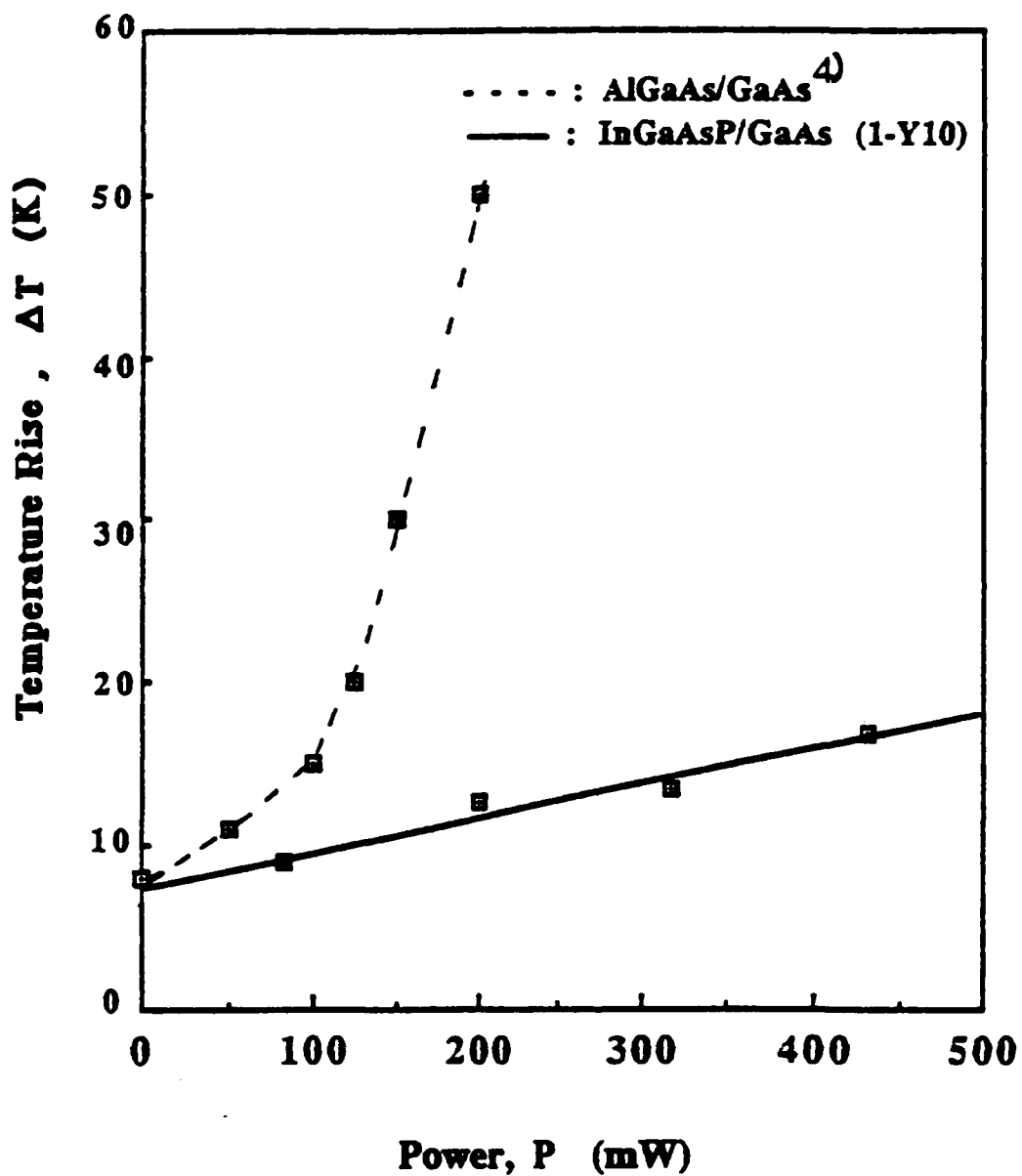


Fig. 19 (13:L1687) Local temperature rise at the mirror facet of InGaAsP/GaAs SCH SQW laser without mirror coating. Initial temperature rise (~8 K) reflects facet heating before threshold of stimulated emission.

the excess surface arsenic atoms which can form dangling-bond orbitals. This study concludes that in using phosphorous in the GaAs based device prevents the segregation of arsenic atoms and in turn reduces the number of recombination sites and thus lowers local facet heating.

II.2.3. Influence of Material Traits and Cavity Dimensions. The next article, by Ghafouri-Shiraz (14:38), investigated the effects of various material and structural parameters on the properties of InGaAsP/InP laser. The facet reflectivity and the mirror loss warranted interest in this review. After a highly mathematical treatment, the author demonstrated how the reflectivity increases with the thickness of the active layer and with an increase in the difference of the refractive indexes of the three layers composing a laser, $\Delta n = |n_a - n_c|$ (Fig 31a-b). The other trait, the mirror loss α_{mo} , depends not only on the facet reflectivity (R_0) but the length of the lasing cavity L ,

$$\alpha_{mo} = \frac{1}{L} \ln(1 / R_0). \quad (2.13)$$

The equations leading to these two properties contribute toward designing a laser's facets with inherently favorable traits.

II.2.4. Dielectric Coating. Having highlighted some of the traits of the facets, the next topic involves the degradation of laser performance caused by facet erosion. Gfeller's and Webb's report analyzes over 235,000 device hours of stress studies on single-quantum-well graded-refractive-index edge emitting heterojunction AlGaAs ridge lasers with uncoated and half-wavelength Al_2O_3 -coated facets (6:14). The coated facets demonstrated the same 30% reflectivity as the uncoated facets in order to keep the variables at a minimum. The stress studies conducted include lasing isothermal operation at fixed and multiple optical powers, fixed optical power at multiple temperatures of operation, and constant temperature and current operation in the non-lasing regime.

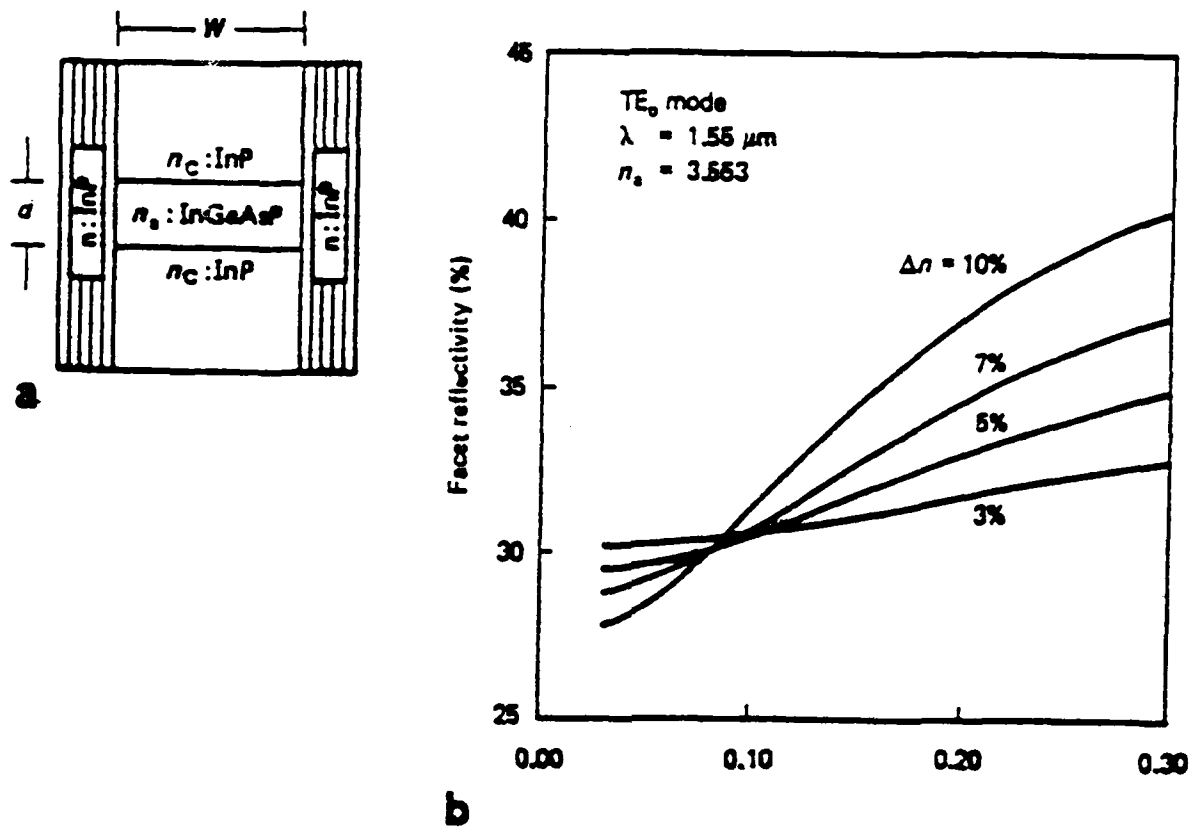


Fig. 20 (14:39,42) Variation of facet reflectivity R_0 for the fundamental TE_0 mode as a function of active layer thickness $d < 0.3 \mu\text{m}$ with Δn as a parameter.

The first stress environment compared operation of both lasers at 30 mW optical power and 50°C heatsink temperature. Ten uncoated lasers demonstrated three degradation phases. The first phase exhibited a 5%-15% increase of laser current during the first 100 hours of operation. The second phase exhibited gradual degradation lasting several hundred hours, roughly 45% increase over 700 hours. During this phase, due to the high power densities, 80% of the devices failed by sudden catastrophic increase of laser current with a mean time to failure of 130 hours. The remaining devices exhibited a

superlinear rate of degradation up to twice the initial current after 700 hours of operation. Ten coated lasers produced degradation rates of roughly 0.18%/khr (khr = 1000 hours) and no catastrophic failures occurred. The coated lasers did not reach the third phase of degradation.

The next stress test compared operation of the lasers at 30 mW optical power and 100°C heatsink temperature. The uncoated lasers demonstrated gradual degradation up to 40 hours, followed by catastrophic failure in all cases with a mean time to failure of 46.5 hours. The coated lasers produced a gradual degradation rate of 0.83%/khr after 6000 hours of operation.

To investigate the degradation behavior of the lasers at different optical power levels, twenty lasers, half coated and half uncoated, operated in a sequence of 10/30/50 mW optical power at 50°C heatsink and another twenty operated in the reverse power sequence.

In the forward sequence, each uncoated laser was permitted to degrade 15%, as measured by the increase in current, at each power level before progressing to the next level. The uncoated lasers produced approximately linear degradation curves with time and the corresponding degradation rates increased exponentially with optical power. The uncoated lasers operating at 30 mW demonstrated a 35% lower degradation rate than those of the isothermal tests. Also, catastrophic failures occurred among only 20% of the devices, all during the 50 mW phase, significantly lower than the 80% of the isothermal tests. The uncoated lasers intended to operate in the reverse sequence demonstrated drastically different behavior. All devices failed catastrophically with a mean time to failure of 1 hour during the first 50 mW phase. These results imply that laser lifetime may be enhanced by applying low power pre-aging to the devices.

Degradation could not dictate the power step transitions of the coated lasers due to their much slower degradation and thus they operated 1500-2500 hours at each power level. Also, for added data on coated laser degradation, with 100°C heatsink

temperatures, ten lasers operated with the same forward power sequence and ten lasers with the reverse power sequence. The linearized degradation rates produced a similar exponential increase with optical power as the uncoated lasers but at rates 60-100 times lower than the corresponding uncoated lasers. The average degradation rates measured the same for forward and reverse sequences. Fig. 21 displays curves relating the uncoated and coated laser degradation.

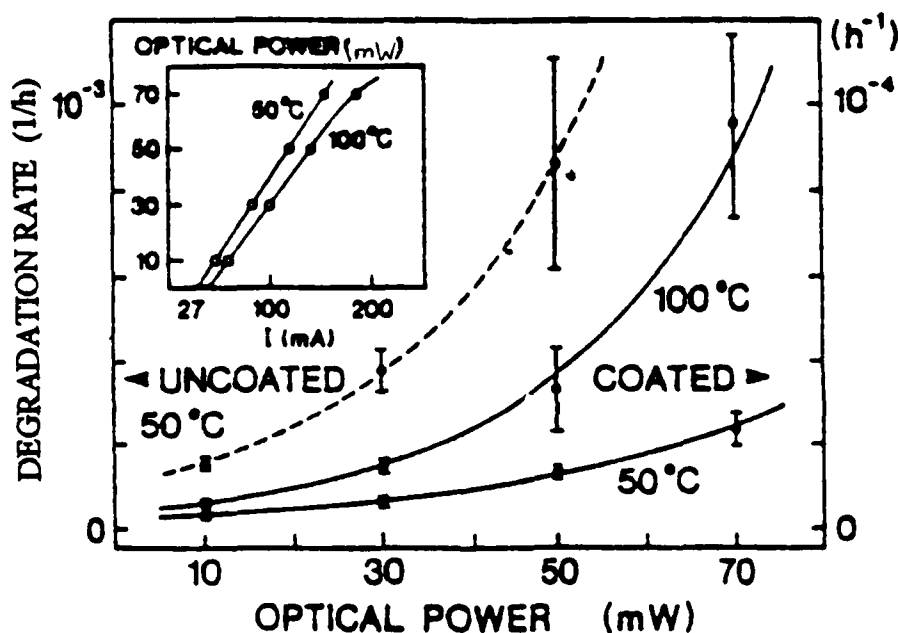


Fig. 21 (6:17) Laser-current degradation rates $R = d/dt (1/I_0)$ vs. optical power (power-step stress). Inset: P - I characteristics.

The next test subjected coated and uncoated lasers to a constant current at one half the threshold current and then at the threshold current for 1000 hours each at 50°C. The test generated the time change of the (normalized) threshold current (R_{th}). The uncoated lasers showed a small increase of R_{th} with current in the nonlasing regime ($R_{th} = 1 \pm \Delta 0.5 \cdot 10^{-5} 1/h$) and strong degradation ($R_{th} = 3.75 \pm \Delta 1.5 \cdot 10^{-5} 1/h$) in the lasing regime. Coated lasers showed negligible degradation and even negative degradation in

some cases. The degradation discontinuity between this test and the power step tests suggests that temperature and optical power in the facet region act as degradation accelerants in the lasing regime.

To summarize this study, a series of isothermal, constant optical power, and constant current tests demonstrated that while the facet coating would not prevent degradation, it does permit longer operation at higher temperatures and higher optical power outputs. The coating reduced the degradation rate as a function of optical power by a factor of 60 -100. These experiments also demonstrated that pre-aging uncoated lasers at low optical powers, for this design at around 10 mW, will improve the lifetime and slow the degradation rate of the device. Over all, these studies demonstrate facet coating as one design tool for producing lasers that may run at higher temperatures and higher optical powers.

All the study conducted on semiconductor facets serves the drive to improve semiconductor lasers. The next article, by Chen *et al.*, cites applications for dielectric coating to semiconductor lasers (15:245). On a basic level, by changing the reflectivity of the cavity mirrors, the total loss of the cavity, and hence the threshold current, also change. Another important use involves maximizing the external quantum efficiency for the output facet. Also, using facet coatings to dictate the reflectivities of the mirrors, a single device may have a highly reflective mirror in back and a front mirror, the output port, with low reflectivity, and hence high transmissivity. The spectral properties of a laser may also be modified by facet coatings. Via facet coating the lasers may be fine tuned to a desired wavelength and the bandwidth of the frequency pulse narrowed. The narrow bandwidth permits the laser to work more like a monochromatic energy source.

II.2.5. Optical Flux Density and Current Density. Chinone et al. conducted a study on the long-term degradation driven by facets to determine if the optical flux density contributes more than the current density to degradation (16: 1160). The tests demonstrated that the degradation rate rises steeply once the current density breaches a

certain value dictated by design. The tests also proved that the degradation rate grew proportionally to the optical flux density. Furthermore, all devices showed very little degradation before lasing commenced. The results indicated that the optical flux density during operation contributes more strongly to the long-term degradation than the current density. During the tests, the mirror facets were examined and noticeably damaged. Facet erosion appeared on gradually degraded diodes without exception. A final observation noted that the facet erosion involved the ambient atmosphere as certain regions of facet material were left unexposed to the atmosphere and these were hardly damaged.

II.2.6. Variations of a Quaternary Semiconductor. The next study, conducted by Hayakawa *et al.*, focused on facet degradation as a function of the relative portions of a quaternary semiconductor, $\text{Ga}_{1-x}\text{Al}_x\text{As}/\text{Ga}_{1-y}\text{Al}_y\text{As}$ (17: 6068). Simply put, compounds with mole fractions x of 0-0.17 and $y = x + 0.3$ were compared. The degradation formed with x near 0 arose mainly from the formation of dark region defects and dark line defects originating from the facet surfaces. Facet oxidation dominates for x at 0.08 and above, oxidizing faster as x increases. Life tests were performed for lasers with $x = 0, 0.05, 0.08, 0.12$, and 0.17 . These constant optical power tests revealed that the driving currents increased approximately in proportion to the square root of operating time for uncoated lasers in all cases. An Al_2O_3 facet coating effectively suppressed the degradation for x at 0.08 and above. The minimum degradation occurred for $x = 0.08$ and the explanation offered reasoned that the refractive index of this particular compound matched that of the native oxide that formed during operation. The ambient humidity provided another effective accelerant to degradation for uncoated lasers with higher x mole fractions. Again, the facet coating suppressed this influence.

II.2.7. Facet Degradation Summary. In summary, this paper has reviewed the traits of facets in semiconductor lasers. The local temperature rise results primarily from the optical flux of lasing. This temperature rise causes the facet to erode. as a result of facet erosion, the laser requires more current to sustain the same amount of optical output.

As a means to counter the device's degradation, studies employed facet coating and demonstrated them to markedly slow facet erosion. The next article suggested several practical applications for dielectric coating on facets including adjusting the threshold current and narrowing the frequency's bandwidth. The final studies reviewed demonstrated that device degradation can be reduced by incorporating phosphorous into GaAs or using $\text{Ga}_{1-x}\text{Al}_x\text{As}/\text{Ga}_{1-y}\text{Al}_y\text{As}$ with mole fractions $x = 0.08$ and $y = 0.11$.

II.3. Contact Degradation

II.3.1. Introduction. This study focuses on the recent developments in ohmic contacts as they apply to III-V compounds and the bonds to these contacts. As the thesis involves operating devices around 100°C , particular attention is paid to the influence of extended operation at elevated temperature on p-type and n-type ohmic contacts.

II.3.2. General Requirements. The bulk of this review stems from an article outlining the development of contacts over the last twenty years by Shen et al. (18:2113). The end product of a sound ohmic contact is to provide a connection without a large potential barrier between the metal and semiconductor. If it were to have a large barrier it would produce a rectifying connection or a contact with high specific contact resistance. The specific contact resistance is simply the resistance of the contact multiplied by the area of the contact, $\rho_c (\Omega \cdot \text{cm}^2)$. Two successful processes have emerged to answer these demands, molecular-beam epitaxy (MBE) and rapid thermal processing (RTP). These processes are the most relied upon techniques at present, and the following review outlines the behavior of contacts developed from these methods.

An early general conclusion of Shen et al. paper lists the dominant variables influencing specific contact resistance to be the doping level in the semiconductor, the barrier height of the metal-semiconductor combination, the carrier effective mass, the dielectric constant, and the temperature (18:2113). The geometry of the contact and current crowding effects do not heavily influence the contact resistance in typical operation.

Next the study outlines seven critical properties of a good ohmic contact.

Table III lists the factors and typical quantities relevant to these properties. The properties are listed below:

- 1) Low specific contact resistance: Mid- $10^{-6} \Omega \text{ cm}^2$ are typically acceptable for devices with $1\mu\text{m}$ dimensions but as devices shrink so must this parameter.
- 2) Contact stability: Shallow contacts with sharp interfaces must be maintained in the 400°C processing temperatures inherent to GaAs. Spiking typical to Au alloys when exposed to these temperatures are deleterious to small contacts.
- 3) Surface smoothness and good edge definition: Small clearances between devices demand good edge definition to avoid shorts. Also a smooth surface morphology is needed to ensure good pattern definition. This implies that non-alloyed ohmic contacts are needed.
- 4) Corrosion resistance: Oxidation and corrosion during processing and before wire bonding must be evaluated in terms of the integrity of bonds and the long term reliability. Inert metals such as Au satisfy this particularly well.
- 5) Radiation damage resistance: GaAs devices typically perform better than silicon in high radiation environments, encouraging use of these devices for work in such conditions. Thus contacts must be developed to resist such environments.
- 6) Low residual stress: Minimizing stress reduces induced dislocations which contribute to degradation. Typical solutions require thinner metallic layers and using metal with similar lattice constants and coefficients of thermal expansion to the semiconductors.
- 7) Good thermal and electrical conductivities: For large scale integration, heat dissipation is a limiting factor, and thus metallization must have high thermal and electrical conductivities.

II.3.3. Au-Based Contacts. Having outlined the characteristics of the ideal ohmic contact, the next problem demands finding the best available compromise to fill the demands. Au-based contacts seem among the best packages owing to their low specific

Factors	Desired conditions
Design	Fewer layers, moderate thickness, round edges
Processing	Simple, easy for mass production, wide process window, and withstand 400 °C for packaging/high temperature (800–900 °C) for dopant activation
Reproducibility	Good
Yield	High
ρ_c	Low ($< 10^{-6} \Omega \text{ cm}^2$)
Sheet resistance	Low (a few Ω/\square)
Thermal stability	Good (no ρ_c change at 400 °C for 100 h, minimum; no lateral and vertical diffusions)
Surface morphology	Smooth
Edge definition	Sharp
Corrosion resistance	Good (no oxides, no electromigration)
Wire bondability compounds	Compatible with Au or Al wires, no brittle intermetallic
Radiation resistance	Good
Cost	Low
Residue stress to semiconductor	Nil
Long term stability in service (10% increase in ρ_c)	> expected device lifetime
Thermal expansion coefficient	Close to the matched semiconductors
Adhesion to III-V compounds	Good

Table III (18:2116). Requirements of a good ohmic contact for III-V compound semiconductors.

contact resistance, good bondability, ease of deposition, and inertness. The primary drawback arises from the low melting point typical of this family of alloys.

Recent developments in contacts to n-type GaAs involve analyzing and comparing the Ni/AuGe/GaAs connection (18). Although an initial Ni layer optimizes the alloying kinetics and the interface can be smoothed to within 20nm, thermal stability and edge deterioration still exist. After comparing Au/Ni/Ge, Au/Pd/Ge, and Au/Pt/Ge, the Au/Pt/Ge demonstrated the best electrical properties and surface morphology. This implies that the Pt may serve to replace Ni in the Ni/AuGe metallization.

Other attempted alternatives to Ni/AuGe include employing refractory metals such as W, Ti, and Mo for high temperature metallizations (18). These systems have demonstrated stability up to 700°C and thus also act as a barrier to Ga and As out-diffusion. Au/Cr/Au/Ge contacts have been demonstrated as thermally stable for 128 hours at 390°C.

P-type GaAs contacts have not received as much attention, but recent advances have generated specific contact resistances down to the $10^{-7} \Omega \cdot \text{cm}^2$ range. The recent RTP techniques produced Au/Zn/Au and Pd/Zn/Pd contacts in this category (18). Studies used NiInW and Pd/Sb(Mn) metallizations to obtain a low specific contact resistance that remained stable for over 30 and 20 hours respectively at 400°C.

The summary by Shen et al. continues to highlight customized metallizations for AlGaAs, InGaAs, InGaAsP, GaSb, InP, and InAs. Intrinsic to these systems are unique methods employed for contact improvement. Although certainly of interest to future development should the contacts become a limiting factor to elevated temperature operation, they are too specialized for the present research aims.

II.3.4. Characteristic Performance. Intrinsic to this research are the reliability and actual performance of the contacts operating at extended heated conduction. Failure mechanisms are grouped into three main categories due to operation at high current density, high temperature, and high electric field conditions:

- 1) degradation due to interdiffusion between the metal and semiconductor,
- 2) metallization shorts or open circuits due to electromigration, and
- 3) inter-electrode shorts due to field induced electrode material transport.

Examples are presented describing each category of failure mechanism.

The most routine n-type Ni/AuGe contacts have demonstrated interdiffusion during package processing. Au penetrates 0.1-0.3 μm into the GaAs. A general means of reducing the diffusion is the installation of a barrier layer such as TiN to reduce atomic mobility.

Electromigration is a mass transport mechanism caused by electrons colliding with atoms and transferring momentum. Electromigration has been observed in Al, Al-alloy, and Au films operating at $5\text{-}20 \times 10^5$ A/cm², 200-300°C, for 10-1000 hours (1:142). If the metal layer is non-uniform a choke point in the current can occur. This point will experience a higher local current density and thus cause a higher mass flux. The non-uniform flux will remove more material from the choke point and exacerbate the non-uniformity. Eventually an open circuit may form. The choke point is referred to as a void and the material build-up down current as a hillock. The moved metal ions condense and form whiskers around the hillock as well.

As devices continue to shrink inter-electrode distances diminish and high fields become more influential in inducing inter-electrode migration. The whiskers that grow with this migration may form paths between electrodes. Migration has been demonstrated to be related to the amount of As₂O₃ on the GaAs surface prior to metal deposition. Ammonia plasma treatments before a Si₃N₄ deposition have diminished metal migration.

II.3.5. Wire Bond Degradation. While electromigration is influential to contact degradation, it also serves as the primary degradation mechanism for the wires' bonds to the electrodes (1:140). The reaction between metals also contribute and both mechanisms serve to increase the thermal and electrical resistance. Continued degradation leads to open and short circuits.

Aging studies demonstrate interdiffusion and intermetallics formation at the interface between solder and electrodes. Soft solder, such as In and Sn, generate grain boundary diffusion of Sn into Au and bulk diffusion of Au into Sn. Typically the grain diffusion proceeds more rapidly. After the diffusion intermetallics form. Generally a hard solder, such as Au rich Au-Sn, Au-Si, or Au-Ge, are markedly more stable and slow the diffusion.

Hard solder will also fatigue less if thermal cycle stressing or power cycling are inherent to the aging of the device. Soft solder will initially protect devices from mechanical stress in thermal variants, but the solder degrades and eventually cracks.

Returning to electromigration, void formation at the soft-solder bond will generate thermal hot spots as described previously. If a laser must maintain a given output power, the void's increased thermal resistance will increase the local operating temperature, which will inherently degrade efficiency and demand more current to maintain power. The process of positive feedback leads to a rapid increase of current and is called thermal runaway. Lasers have demonstrated this within 10,000 hours of aging at 50 to 70°C and under 1,000 hours at 100°C (18). Studies have also demonstrated that the current clearly enhances thermal resistance increase when metals such as Cr, Pt, and Sn are employed. Although the eutectic melting point for the Au/Sn solder is over 200°C, the three materials react with each other at 100°C under current biasing. If the package is passively baked at 200°C the same reaction does not occur. The general solution to these degradations demands using hard solder.

II.3.6. Contact Degradation Summary. This review has outlined the development and degradation mechanisms studied involving ohmic contacts to III-V semiconductors. The semiconductor doping level, barrier height, carrier effective mass, and the temperature strongly influence the specific contact resistance of ohmic contacts. Presently Au based contacts provide the best available systems for ohmic contacts. Their primary drawback stems from fact that the melting point for such alloys is generally below temperatures needed to process GaAs semiconductors. Otherwise the contacts strongly satisfy the characteristics desired of good ohmic contacts. Such properties include low specific contact resistance, surface smoothness and good edge definition, corrosion resistance, radiation damage resistance, low residual stress, and good thermal and electrical conductivities.

As this research intended to age devices in an accelerated manner, possible degradation characteristics that would limit the lifetime had to be studied. Degradation effected by the contacts and wire bonds to contacts falls under three general mechanisms:

- 1) degradation due to interdiffusion between the metal and semiconductor,
- 2) metallization shorts or open circuits due to electromigration, and
- 3) inter-electrode shorts due to field induced electrode material transport.

The last two mechanisms may generate a characteristic known as thermal runaway. The voids formed by a local hot spot in the metal increase current density which increases the migration and increases the thermal resistance. This process is self enhancing and if a laser is driven to maintain a constant power output it can only do so by increasing the current and accelerating the electromigration. The final result is a open circuit and failure of the laser.

The final section addressed degradation attributed directly to the wire bonds. The bond sights are particularly prone to diffusion between different metals. While a typical solder may have a melting point well above operating conditions, current has been shown to enhance reactions across the interface which cause degradation. Fukuda generally concluded that to create high reliability lasers, a hard solder, such as Au rich Au-Sn, Au-Si, or Au-Ge, are necessary and soft solders, such as In and Sn, will only operate on a short term basis (1).

II.4. Chapter Summary

This chapter has outlined research on three degradation mechanisms that tend to dictate the operational lifetime of edge emitting semiconductor lasers. These degradation mechanisms are the dark defects, facet degradation, and ohmic contact degradation. Dark defect degradation occurs under the widest range of operation conditions, but as it involves crystal defects throughout the active layer, it typically demands destructive analysis such as transmission electron microscopy (TEM) to verify its influence. Dark defects occur as

point, line, and plane defects. During operation crystal defects throughout the device grow or migrate toward heat sources, typically the active region of a laser. Once in the active region, the defects disturb the tight energy band structure and provide a continuum of energy levels. This continuum allows energy transitions to generate heat and vibration that further disturb the crystal and absorb radiative energy, all promoting further defect growth and laser degradation. The growth rate of dark defects depends on the square of the current density and the density on dangling bonds at material interfaces. Finally, dark defects typically absorb twice the current density of undegraded regions and studies modeled their influence on the spontaneous emission intensity, the threshold current density, and the external quantum efficiency.

The next degradation mechanism addressed involved the influence of facet's on a device's operation. The dominant parameter damaging the facet is the local temperature rise. The optical flux is in turn primarily responsible for this burning of the facet. As the facet burns, it boils off its surface and the reflectivity drops. This in turn demands more current to generate a constant power output. The most effective means for slowing this mechanism demands a dielectric coating over the facets. Another means, although not as effective an improvement, involves adjusting the mole fraction of a ternary compound serving as the active layer to minimize the rate of facet degradation.

Degradation of the electrodes demonstrate the third type of degradation. Three general mechanism are attributed to the solder, contact, and their bond:

- 1) degradation due to interdiffusion between the metal and semiconductor,
- 2) metallization shorts or open circuits due to electromigration, and
- 3) inter-electrode shorts due to field induced electrode material transport.

Typically degradation of the electrodes will result in either an open or short circuit. The primary means of reducing the degradation of the solder and bond is to employ a hard solder. Of course, the contact material itself should match the material properties of the semiconductor and solder to minimize residual stress. Other properties required of a good

contact include low contact resistance, surface smoothness and good edge definition, corrosion resistance, radiation damage resistance, low residual stress, and good thermal and electrical conductivities.

The aim of this research is to demonstrate the roles of these mechanisms in the degradation of lasers running in elevated temperatures and under continuous wave operation. The operation environments of the literature reviewed imply that: first, dark defects degradation can be expected to occur; second, facet degradation will depend highly on the materials employed; and third, that contact degradation is not expected to not be observed in the short time allotted for operation of the devices in this study.

III. Research Support

This chapter serves to summarize the efforts taken to prepare for the effects of elevated operation temperatures on the lifetime of the edge emitting semiconductor lasers provided by the ELR branch of Wright Laboratories. Efforts fell into three general categories; the design and calibration of support hardware, device manipulation, and data gathering. Data gathering is detailed under methodology in the next chapter. The first section expands on the design and calibration of the support hardware. Included among this hardware are a carousel platform, the laser mount, the thermocouples, and the adapters fabricated for use with an optical microscope.

The second section details the manipulation of the devices before subjecting them to elevated temperatures. Topics entailed in this section include a cleaving technique introduced to provide consistent cavity lengths throughout the data base. Also detailed in this section are the steps and criteria employed to select one of three designs for detailed study. Finally, the results of an attempt to burn out a laser with a high current density are detailed.

III.1. Hardware Design/Calibration

The early efforts of this research involved developing the customized hardware used to drive multiple lasers at high temperatures and obtain the optical output of these lasers. The general plan involved operating six lasers on top of independent hot plates. This section outlines the hardware developed to execute this plan. Also, this section describes the hardware constructed to measure the temperature, power output, and dimensions of the laser cavities.

As the spectral distribution of output of the lasers might be called for, a means for directing each laser's output to a monochromator was required. Therefore a rotating platform that would secure the hot plates and mount other typical laboratory hardware was devised. This platform permits each laser to be positioned, in turn, immediately in front of any single set up such as a focusing lens or a power meter. A circular platform with a 36 inch diameter and a 2 inch rectangular grid of 1/4 - 20 threaded holes was machined from 1/4 inch sheet steel. This platform was then mounted on top of a rotating platform intended for a computer monitor. Appendix 1 displays the design diagram and the outlines of the hot plates that would be mounted on the platform.

A laser mount permitting the operation at elevated temperature in a mechanically stable situation was devised next. The other concerns dictating this mount were that any measuring device would have to be placed immediately in front of the laser and that the lasers were to be packaged on TO-5 transistor package mounts. Appendix 2 displays the design diagrams for the final mount employed.

Initially, the plan called for building a feedback network linking the temperature at the laser to a unit controlling the driving power source for each hot plate. Finally it was determined that the thermal controlling hardware would not become available and the single thermal controller unit already possessed by the AFTT Physics Department would have to be employed simply as a thermometer with no active feedback.

After assembling the thermocouples, calibration of the five thermocouples was necessary. Upon attaching the thermocouples to the same location and elevating the point to several temperatures, all thermocouples produced the same results within 0.1°C and thus all were assumed to remain calibrated in future readings.

There were two drawbacks to the resulting setup involving the hot plates. First, the temperature was controlled only by the gauges built into the hot plates. This meant that the time lag between adjusting the temperature setting of the hot plate and its influence on the

laser mount was at least five minutes. The second drawback arose from the fact that the hot plates built in heat sensors allow at least a $\Delta T = \pm 3^{\circ}\text{C}$ tolerance about the desired central temperature. One hot plate generated an oscillation of $\Delta T = \pm 18^{\circ}\text{C}$ which prevented it from being employed more than once. This tolerance was observed in efforts to calibrate and employ the hotplates at 100, 125, and 200°C . As the laser output depends strongly on small changes in operating temperature, it was observed that $\Delta T = \pm 1^{\circ}\text{C}$ at 100°C could induce a $\Delta P = \pm 3\text{mW}$, this varying temperature introduced a large margin of error into maintaining a constant power output. As a result, the power output was adjusted only when the temperature was within one degree Celsius of the desired center temperature.

The final concern involving the thermocouples arises from the systematic error in the measurements recorded. The thermocouples were mounted roughly 1cm from the device. The active layer is known to be a heat source and it was assumed that the difference between the temperature of this region and the thermocouple was consistent throughout the data base.

Having described the hardware necessary for obtaining the power output of the lasers as a function of temperature and current, Appendix 3 provides the block diagram of the setup to obtain these measurements. Appendix 4 provides a list of the hardware employed to execute the measurements.

The next concern dealt with the measurement of the laser cavities' dimensions. These measurements were desired in case a relation based on the cavity dimensions was observed. These measurements were one way of ascertaining the uniformity of the data base. The diversion angle of the output was also necessary and this depends on the width of the laser cavity. A scanning electron microscope (SEM) analysis would be the best route for these measurements but an excessive amount of time would be required to measure all packages. Therefore, due to time constraints, SEM measurements were employed on a fraction of the packages. Optical microscopy was employed to measure all

devices using an Olympus microscope, a 0.01mm standard, and a scribed reticule lens.

The resolution of such measurements was limited to one micron and as the width of the cavities is between 2-10 microns this introduced considerable error.

To employ the optical microscope, aluminum tubes were fabricated to mount a camera and calibration lens for recording the measurements. Four tubes were constructed and Appendix 5 provides the engineering diagrams. As a flat black enamel would not adhere to inside of the tubes, lens paper was rolled up and inserted in the innermost tube. As the paper was a low-reflectivity material, this eliminated the reflected light hindering observation of the target by the camera.

The first target photographed by the optical microscope was a calibration standard. The different magnifications were identified by their objective lenses and the photographs yielded these measurements:

Objective lens	10X	50X	100X
magnification:			
Distance between scribes of reticule	14.4±1µm	2.9±1µm	1.4±1µm

As the calibration may change if the adapters are removed from the microscope, new calibration photos were taken whenever the system had been disturbed between measuring packages.

Next, photodiodes were assembled to measure the optical output of lasers. Six FND-100 photocells were mounted and by design produce a voltage between 3-95 volts that is directly proportional to the power striking the cell. As 1mW will saturate these devices, they could not be placed directly in a laser's path unless steps were taken to attenuate the beam. Attempts were made to place the detectors far enough away from the

laser so as to avoid saturation. Other attempts included placing a paper target in the laser path and measuring the diffuse reflection with the FND-100. These efforts induced considerable error and thus their use to determine the stability of the lasers' output could not be relied upon. Other efforts would have involved focusing lenses and attenuators but three Newport 815 Power Meters were obtained which could read the output directly. These meters were calibrated to the Coherent Fieldmaster power meter each occasion that they were placed in front of a laser. Repeated monochromator measurements suggested that the power meters be calibrated to read a beam wavelength of 960nm at room temperature and a beam wavelength of 980nm at 100°C.

This section has reviewed the design, calibration, and points of concern involving the customized hardware employed in measuring the mechanical, thermal, and optical characteristics of the lasers studied. Appendix 3 provides a block diagram of the setup used to obtain the thermal and optical characteristics. The customized hardware included a circular rotating platform to mount six hot plates, mounts for holding the TO-5 transistor packages, thermocouples to interface between the mounts and the Cole-Parmer Thermal Controller, and aluminum tubes for mounting a camera to an optical microscope. The limited thermal stability of the hot plates produces the largest margin of error in the measurements that were gathered. Another contributor to error in the measurements arises from the one micron resolution of the optical microscopy used to provide the cavity dimensions of each laser. SEM analysis was used as much as feasible to provide more accurate measurements of these dimensions.

III.2. Device Manipulation:

This section details the manipulation of the devices before subjecting them to elevated temperatures. Topics entailed in this section include a cleaving technique introduced to provide consistent cavity lengths throughout the data base. The steps and

criteria employed to select one of three laser designs for detailed study are outlined next. Also detailed in this section is an attempt to burn out a laser with a high current density.

In an effort to minimize the variables of the data base, specifically cavity length, a technique was developed to edge scribe the laser wafer before cleaving into laser bars with a scribe having skip-scribing capability. The technique employed by Wright Laboratories involved manually scribing the edge of the processed wafer before cleaving. This previous manual technique suffered poor device yields as the cleaves were uncontrollable, often shattering a large section of the wafer. This technique also produced unpredictable cavity lengths between 300-600 μ m. The technique developed in this research implements a Loomis MKT-38-LI scribing tool with edge-scribing and skip-scribing abilities, improving device yield to as much as 80%. Furthermore, the range of lengths of the cavities was narrowed to between 393-421 μ m for 79% of the devices where 400 μ m was the target length. A step-by-step summary of the process is detailed in Appendix 6.

An overview of the steps for obtaining the laser strips are listed below:

1. Scribe along the edge of the wafer chip at the desired crystal orientation and spatial period.
2. Mount wafer chip to a soft pliable metal strip with wax.
3. Gently flex the assembly parallel to the scribe marks. The cleaves can be observed by the reflection pattern of the wafer chip.
4. Dissolve the wax to dismount the laser strips.
5. Clean and prepare laser strips for mounting.

With this technique providing a consistent cavity length for the lasers, the next step dictating which lasers were to be tested involved the three designs that ELR had offered for examination. The lab identified these lasers by their wafer numbers, 599, 600, and 706. Wafers 599 and 600 employed a design where each p-contact strip had an n-contact strip on either side. All contact strips were on top of the wafer. Wafer 706 replaced the n-

contact strips by thinning the wafer and laying a metal contact all over the underside of the wafer. If all are operating criteria were identical, wafer 706 would be the preferred design for analysis as this was a simpler design to fabricate. Appendix 7 displays how all devices were packaged and their composition.

The primary criterion for choosing the preferred design was the yield of lasers per packaged devices. A secondary criterion was a low threshold current, at least below 100mA. A sample of each wafer chip was cleaved and mounted to compare these criteria. The cleaving produced the same yield of devices from each wafer and did not influence the following yields. Wafer 599 yielded 25 lasers of a possible 27 and the lasers began lasing below 50mA. Wafer 600 yielded 16 lasers of a possible 30 and began lasing below 90mA. Wafer 706 yielded 6 lasers of a possible 54 and began lasing below 140mA. Thus wafer 599 performed the best in both criteria and served as the data base. Wafer 600 could have served as a possible alternate but the low yield of wafer 706 prohibited any feasible research in the time frame permitted.

The wafer technologies differed primarily in their geometric layouts and had roughly identical materials compositions between the corresponding layers. Thus the output and current demands were expected to be similar. No differences beyond one order of magnitude were anticipated. During the early stages of this research, only a limited number of lasers were available and these were from the 600 and 706 technologies. As the 706 technology was the first available, and due to anticipated similarities, the initial tests providing rough insight to performance were conducted on the 706 technology.

The next tests were designed to overdrive and burn out the facet of a laser. A detailed progression of the spectral characteristics as a function of current at room temperature was recorded. Appendix 8 contains the spectral distributions of the minimum and maximum currents to allow stable lasing for laser 10B. For the single laser tested, laser 10B taken from the 706 wafer, lasing began at 61mA and lased at 945nm. As the current

increased the lasing wavelength shifted almost continuously up to 969nm at 224mA. Lasing discontinued at 225mA. At currents of 200mA and above lasing occurred for multiple wavelengths and the relative power distribution was continually changing. The laser burned out at 430mA but from later SEM analysis this proved due to the wire lead to the laser having melted, forming an open circuit. The laser was reconnected and proved still able to lase. Several 599 lasers proved that the output reached a maximum before any facets burned out.

To summarize this chapter, topics discussed focused on the fabrication, filtering criteria for choosing a laser design, and the general lasing characteristics observed at room temperature. By using an automated scribe with edge-scribing and skip-scribing abilities, laser cavities with lengths between 388-420 μm may be obtained. Next, from observing a sampling of lasers from all designs submitted, lasers packaged from wafer 599 demonstrated the highest possibility of lasing and typically the lowest lasing threshold currents. Finally, it was demonstrated that the laser will saturate before damaging the laser cavity or facets if overdriven by high current densities.

IV. Methodology

The aim of this chapter is twofold. It develops the five phases of analysis that guides the research and along the way demonstrates the three general categories of data obtained. These three categories, the characteristic power curve, the current necessary to maintain a constant output as a function of time, and the dimensions of the lasing cavity, are described as the argument develops. After this a brief outline provides the steps executed on a typical laser device and its control devices.

Lasers were provided by Wright Laboratory for operation in hot (100-200°C) environments. The lasers were provided on a TO-5 package and each package had 3 devices from a single bar on it. Research fell into five phases. The first phase involved the characterization of several lasers to determine a coarse, typical laser description before devices were submitted to any high stress operation conditions. The details of device description included the spectral distribution, the power output as a function of current, and the physical dimensions. Details are provided in the chapter discussing data. Characterization of the lasers occurred after each phase for the remainder of the study. The second phase involved pre-aging the devices at low stress environments in an effort to stabilize and improve future performance. This phase also served as a filtering mechanism for removing the portion of devices that inherently fail at an early stage. The research goals pertained to the devices' behavior in the wear-out stage so this filtering is appropriate. The third phase subjected 15 lasers to operational temperature limits to determine the maximum temperature that the lasers would operate at for two hours. The fourth phase subjected the lasers to 100°C and multiple power outputs to determine their operation in

various high stress environments. The final phase provided the physical dimensions and observable damage via scanning electron microscopy and optical microscopy.

IV.1. Initial Characterization

The first phase of this research served to provide a coarse characterization of the lasers provided. Characterization produced the spectral and optical output power as a function of continuous direct current operation. A side product of this phase was the yield of the 599, 600, and 706 wafer lasers mentioned in the previous chapter. This characterization involved 9 packages from the 599 wafer, 10 packages from the 600 wafer, and 18 packages from the 706 wafer.

The first test assumed that the output would center around a wavelength of 950nm and determined which devices could generate over 1mW of power at room temperature driven by a sustained direct current. A Coherent Fieldmaster power meter with a -30dB attenuator was placed immediately in front of each device. Any device that could generate an output over 1mW on the detector for a current below 200mA was considered a functioning laser.

Next, a device from each wafer that could generate the power had its output directed to the Jarrell-Ash MonoSpec 27 Monochromator. The devices demonstrated a central wavelength around 960nm at room temperature which served as the reference wavelength for all future room temperature characterizations.

IV.1.1. The Characteristic Power Curve. The efforts in the next tests provided a coarse initial evaluation of the power output as a function of the current. From here on this function will be referred to as the characteristic power curve and represents the first of three categories of data that are collected throughout the research. This curve produces the calculated threshold current and the differential quantum efficiency, or slope efficiency, of a laser. These parameters quantify how the operation of a laser changes with the stresses

induced by exposure to elevated temperature and/or lasing for any significant fraction of the device's operational lifetime. Most of these curves were measured by the Coherent Fieldmaster power meter, but when multiple lasers required simultaneous measurements, three Newport 815 power meters were also employed.

For this stage four packages from the 600D series were employed. As this was only a coarse characterization the devices from wafers 600 and 599 were similar enough not to warrant repeating this test for the 599 series that served as the data base for high temperature tests. Differences between the 599 and 600 technologies did not exceed one order of magnitude in the power output, slope efficiency, or required currents. Also future tests demonstrated that the characteristic curve changes significantly in the first two hours of continuous wave operation. In consequence, the characterizations obtained at this point only loosely resembled the typical characterization of a 599 laser taken immediately after pre-aging. This will be discussed shortly and detailed in the data chapter.

For the bulk of the data base, four distinct stages of analysis warranted the measurement of the characteristic curve. The first stage occurred at room temperature operationally immediately after pre-aging the device. The second stage occurred when the operational temperature initially stabilized at 100°C. The third stage occurred at the end of the elevated temperature period. The fourth stage occurred when the laser had returned to room temperature. Occasionally concerns warranted an additional intermediate characterization during the elevated temperature period.

To summarize the first phase of the research, the first test determined which devices actually lased. Next, several lasers were directed to the monochromator to obtain the average central wavelength at room temperature. Then a characteristic power curve was obtained to provide the guidelines for the expected threshold current, the initial slope efficiency, and the typical output power a device could generate before saturation. This

characterization provided the level of current to drive the device in a low stress manner with regard to the current and expected optical output.

IV.2. Pre-Aging Lasers

Moving on to the second phase of research, the lasers were pre-aged to avoid the rapidly changing lasing characteristics inherent to a new device. As suggested in previous studies, a typical laser design may operate up to 10,000 hours at room temperature. Thus pre-aging at room temperature and low lasing output power for 24 hours seemed unlikely to significantly influence the lifetime measurements for these devices. Literature indicates this is a common practice and has been demonstrated to enhance future performance. From the measurements taken correlating the output power as a function of constant current and time, the power tended to increase in the first 20 hours. No literature found offered a mechanism for this improvement. As the study would focus on degradation this initial improvement would only delay the measurement of relevant data during high temperature testing. Five lasers from the 599 wafer were set initially at 1.5mW output and after 17 hours at a constant current and room temperature, four lasers increased output power at least 268 % and the fifth stopped lasing. Another five lasers from the 599 wafer were set to 1.5mW and operated at a constant current for 16 hours. Four laser outputs increased at least 200 % and again the fifth stopped lasing.

Three other general performance traits in operating the lasers were observed. First, from the tests trying to obtain the initial characteristic power curve and also from trying to set the pre-aging power to 1.5mW, the initial half hour seemed to demonstrate the most dramatic increase in output power for a given lasing current above the lasing threshold current. This result suggested that pre-aging was not necessary for the duration used in tests already described. Using a maximum rate of change in output power of 0.1mW/hr to define a "stable laser", the average pre-aging period lasted 10.7 hours. Second, for a laser

that had been pre-aged and turned off for at least an hour, the first ten minutes of operation when turned on again demonstrated a mild increase of typically 1mW in output power for a constant current above threshold current. The third trait, observed in efforts to overdrive the lasers, was the saturation and discontinued lasing at high current densities. At room temperatures the lasers typically stopped lasing around 230mA. At elevated temperatures the saturation phenomenon set in at lower currents.

IV.3. Maximum Lasing Temperature

The third phase subjected 15 lasers to operational temperature limits to determine the maximum temperature that the lasers would operate at for two hours. These 15 lasers from the 599 wafer were operated at 125°C and 100°C. Only one laser of the five pre-aged lasers tested, laser 34B, would lase at 125°C. It generated 7mW for no more than five minutes and then quit lasing. The temperature for all devices was then reduced to 100°C. At this temperature, 8 pre-aged lasers were tested of which 3 lased. Also, 3 un-aged lasers were tested of which 1 lased. Laser 38B, maintaining a 3.3mW output, discontinued lasing after 29 minutes. The un-aged laser, laser 37C, lasing at 10.1mW, discontinued lasing after 100 minutes.

Two lasers were not monitored for roughly 8 hours at 100°C, and this introduced a large margin of uncertainty. Laser 34B, lasing at 4.5mW, discontinued lasing somewhere between 279 and 1005 minutes. Note that this is the laser that discontinued lasing at 125°C. The final laser, laser 38A, lasing at 6.6mW, stabilized at 94.7°C during the 8 hours of unmonitored lasing and the power dropped by 32% to 4.5mW in this time frame. Upon resumed monitoring, the device gradually required more current for the final 3 hours of observation. A crude projected lifetime was calculated to be 680 minutes for laser 38A under these continuous wave conditions. The current, temperature, and power histories are plotted for each lasing device in Appendix 9.

These tests demonstrate that at least two distinct mechanisms caused laser failure. Had an initial room temperature power versus current characterization and characterizations at the elevated operating temperature been taken at the start and end, these could be compared to each other and compared to a fourth characterization of each laser after it had returned to room temperature. The change in slope efficiency and threshold current would serve as indications of dark area defect damage to the cavity for the device demonstrating the gradual increase in driving current needed to maintain a constant output power. Unfortunately, this was not done and this lesson learned provided guidance for the later phases.

The second degradation mechanism, suggested by the sudden discontinued ability to lase, might suggest facet damage. This could be confirmed by measuring the lasing characteristics at room temperature and by SEM analysis. Again, power characterization before, during, and after lasing at the elevated temperature might have provided insight.

IV.4. Elevated Temperature Stresses

The fourth phase subjected the lasers to 100 °C and multiple power outputs to determine their operation in various high stress environments. The procedure for this exposure was executed according to the following steps:

1. A characteristic power curve was obtained at room temperature with the Coherent Fieldmaster power meter for the control and test lasers. Each laser lased for 10 - 45 minutes to permit stabilization.
2. For three of the five hotplate setups, a Newport 815 power meter, calibrated to the appropriate constant power level to be examined and for a wavelength responsivity of $\lambda=980\text{nm}$, was positioned in front of the laser. These meters were not moved again until the elevated exposure was over. Calibration occurred at room temperature and the Newport 815 was adjusted to the Coherent to read the identical maximum reading for the

identical current. The calibration wavelength for 100°C, 980nm, was determined by directing two lasers from the first test run to the monochromator.

3. Current source was disengaged.

4. Hot plate was elevated to 100°C and allowed to stabilize. Typically 45-120 minutes were necessary.

5. A characteristic power curve was obtained at 100°C. A 10 minute stabilization period was again observed before taking measurements.

6. If special concerns dictated, a characteristic power curve would be obtained in the middle of the elevated exposure period. The control laser was permitted the 10 minute stabilization period.

7. When the elevated operation was deemed complete, another characteristic power curve was obtained. The control laser was permitted the 10 minute stabilization period.

8. Upon returning to room temperature, typically 8-12 hours later, a final characteristic power curve was recorded by the Coherent Fieldmaster power meter. A 10-45 minute stabilization period was observed for all lasers.

IV.4.1. Current vs. Operation Time. The actual length of the elevated temperature period was typically determined by the second category of measurements, the current necessary to maintain a fixed power output as a function of laser operation time. Laser literature, Fukuda [2], establishes two standard means for determining when a device has failed. First, when the device can no longer lase for any given current. This can be observed when a previously lasing device suddenly sharply drops in output power and will no longer display two regions with distinct slope efficiencies. The second standard for failure describes the device as failed when 1.5 times the current initially required to produce the desired output power is necessary to generate the same power. As a consequence of this

second standard, devices lased at 100°C continuously at 5, 7, or 10mW and the current was monitored and regularly recorded as a function of the operation time of the device.

Generally two scenarios dictated the length of the laser's exposure to elevated temperatures. First, if the device operating throughout the exposure failed as per either of the standards above, then the exposure period had effectively been completed. Second, if a constant rate of current increase had been measured for at least three hours and the laser had operated for at least eight hours total, then a time to failure could be linearly extrapolated and the exposure period could be terminated.

IV.5. Cavity Dimensions

The final phase of research obtained all structural aspects of the device structures. This was necessary in case a relation could be made between performance and the cavity dimensions. Divergence angles also depended on device geometry, thus dictating a need for this phase. This introduces the third category of data gathered, the dimensions of the laser cavity. Two means were employed to obtain these dimensions, scanning electron microscopy (SEM), and optical microscopy.

Beginning with the traits of the SEM analysis, it could provide a resolution of 10nm whereas the optical microscopy only produced 1 μm at best. The SEM process also exposed a coarse profile of the quantum well, crystal defects near the surface, and various types of structural damage induced during fabrication or mounting of the devices. Finally, this process would have exposed any dark line defects that reached the facets and any catastrophic optical damage to facets. The drawbacks to this avenue were that this process typically demanded an hour for each TO-5 package, professional assistance had to be scheduled, and reservations for use of the system had to be made at least a week ahead of time.

As the only viable alternative, optical microscopy was employed to get the rough dimensions of all the cavities and SEM analysis was performed on a sample portion of the devices. The next chapter demonstrates any possible influence of the cavities' dimensions on the degradation characteristics.

IV.6. Testing Sequence

This section outlined the steps performed on the bulk of devices analyzed. As the first and third stages of research were aimed at providing rough insight to expected performance they were not executed on the majority of the test base. Thus the test base of 56 lasers distributed over 30 packages underwent pre-aging, the elevated temperature exposure procedure, and optical analysis for obtaining the cavity dimensions.

IV.7. Chapter Summary

In summary, this chapter developed the five stages of research employed to model the high temperature affects on laser operation. As a result of this work, three general categories of data were obtained. The first involved recording the optical power output as a function of current for a given ambient temperature and point in the operational lifetime of the laser. The second form of data mapped the current required to generate a fixed power output over an extended period of time at 100°C. The third type of data was the dimensions of each lasing cavity. After describing the reasoning and procedure to each stage of research, a brief outline of the testing cycle executed on the bulk of the test base was provided. The trends and discussion of the resulting data are addressed in the next chapter.

V Data Analysis

This chapter presents and develops the data obtained via the methods outlined in the last chapter. Two factors, one, the characteristic power curve, and two, the current demanded as a function of time to produce a constant output power, provide the cornerstones for most of the data development. For this reason a sample of each factor is detailed for a single laser. Next, the theory and development of the operational lifetime function is presented. In this development four categories of laser performance will be established based on the observed and calculated lifetimes. After developing various degradation mechanisms' influences on the lifetime, a summary of the characterizations obtained is given based on the various operating conditions. The final topic addressed will be the unpredicted trend of improved laser performance at initial exposure to 100°C. Mechanisms are proposed to explain this trend. The efforts taken to rule out or confirm these mechanisms are also presented.

V.1. The Characteristic Power Curve

This section provides the theoretical and experimental justification for the characteristic power curve repeatedly encountered throughout this document. First the theory is presented leading to the traits of this function. Next, an argument is made to justify the power measurements obtained. This requires calculating the divergence angles for the lasers. Having justified the theory and measurements for the curve, a detailed explanation of the calculations made on a single laser's measurements is conducted.

V.1.1. Gain, Threshold Current, and Efficiency Parameters. The detailed theoretical development of laser characteristics following shall provide insight as to how dark area defects and facet erosion play into the lasers' degradation. Fundamental laser

theory defines the threshold gain coefficient as that gain which occurs when the light wave makes a complete traversal of the cavity without any net attenuation (1:48). The gain originates from an injection excitation and the loss arises from the absorption loss in the active layer and the mirror loss at each facet. Mathematically, these effects are collected as the threshold condition:

$$R_1 R_2 \exp(2L(g_{th} - \alpha_i)) = 1 \quad (5.1)$$

$R_1=R_2=R$ the facet reflection coefficients

L the length of the cavity

g_{th} the threshold gain coefficient

α the absorption loss coefficient

Rearranging to isolate the gain coefficient obtains

$$g_{th} = \alpha + \frac{1}{L} \ln \frac{1}{R} \quad (5.2)$$

The mirror loss depends on the refractive index difference between the laser material and the surrounding medium (air) as :

$$R = \left[(n_r - 1) / (n_r + 1) \right]^2 \quad (5.3)$$

Where n_r is the refractive index of the laser material. Fukuda cites typical values for a InAlGaAs/GaAs lasers as(1:49):

$$n_r = 3.5$$

$$R = 0.30$$

$$\alpha = 10-20 \text{ cm}^{-1}$$

The gain coefficient, as a spectral function, changes with the driving current density, while the absorption coefficient remains fairly constant. The gain peak gradually shifts to higher energies as band filling occurs with higher currents. These relations are portrayed in the figure below.

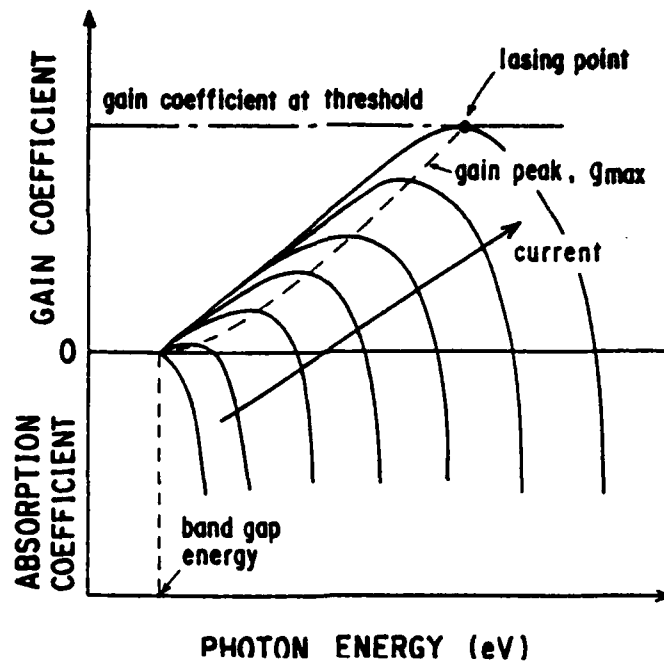


Fig. 1 (1:49) Change in gain spectra as a function of carrier injection.

The maximum gain coefficient can be approximated as a function of current density by:

$$g_{\max} = \beta \cdot \left(\frac{J}{d} - J_0 \right)^m \quad (5.4)$$

where d , the active layer thickness, is in microns, J , the current density, is defined for a thickness of 1 micron, m is a value between 1-2, and β is a constant (1:49), (Fig. 1).

Finally, J_0 is the current density over a 1 micron thickness required to obtain a gain. The threshold gain coefficient occurs at the peak gain under threshold current density.

A more accurate model accounts for the fact that not all of light is contained in the active layer. Defining Γ as the ratio of light in the active layer to the total light, the gain coefficient must be corrected as only the light in the active layer is related to the gain. The new model gives:

$$g_{th} = \left(\frac{1}{\Gamma} \right) \left(\alpha + \frac{1}{L} \ln \frac{1}{R} \right) \quad (5.5)$$

The threshold current density can be obtained from the last two equations to gain:

$$J_{th} = (d / \beta) \left\{ \left(\frac{1}{\Gamma} \right) \left(\alpha + \frac{1}{L} \ln \frac{1}{R} \right) \right\}^{1/m} + dJ_0 \quad (5.6)$$

Fukuda again cites typical parameters for the AlGaAs/GaAs laser as follows (1:50):

$$\beta \approx 0.02$$

$$\Gamma \approx 0.2$$

$$\alpha \approx 10\text{-}20 \text{ cm}^{-1}$$

$$m = 1$$

$$J_o \approx 4000 \text{ A/cm}^2 \cdot \mu\text{m}$$

The threshold current then can be obtained by multiplying the threshold current density by the cavity length and width of the active light emitting region, or for this study, the width of the p-side ohmic contact. The threshold current will increase as degradation occurs. In this model the absorption and facet reflection coefficients change to account for the increased threshold current as the facets and active region develop crystal defects that absorb more energy.

An approximation for threshold current can be obtained from measurements of the output power as a function of driving current. At low currents there is spontaneous emission to produce photo-luminescence and the gain increases with current. At threshold current, the light wave makes a complete traversal of the cavity without attenuation and this will begin the lasing process, the generation of a continued coherent light wave. With coherent light, the power of the electrons add only in a constructive manner and the gain, not to be confused with the gain coefficient, will increase at a markedly higher rate with continued increase of current (19:272).

For semiconductor lasers, the gain, and hence power, increases linearly with increased current until saturation effects, involving the finite number of available carriers for triggered transitions, set in. This linear relation can be extrapolated down to the intercept of zero optical power. The value of current at this extrapolated point serves as an approximated threshold current, I_{th} . The relation can be summed up as:

$$P = \frac{\Delta P}{\Delta I} (I - I_{th}) \quad (5.7)$$

Thus by measuring the spectral optical power against a measured driving current this relation can be demonstrated and an estimate for the threshold current obtained. This is the characteristic power curve already introduced and which served as the cornerstone for much of the development to follow.

Another parameter used to characterize a laser that inherently results from these measurement is the slope efficiency, $\eta_s = \Delta P / \Delta I$. This could be used as an alternate means to measure device degradation as this parameter drops with degradation.

A theoretical value corresponding to the slope efficiency is the external differential quantum efficiency, η_d (1:52). This value expresses the ratio of the photons emitted to the carriers injected by current. The emitted light results from a function of the gain and loss in the system as follows:

$$\begin{aligned} \eta_d &= \eta_i (2\Delta P / h\nu) / (\Delta I / q) \\ &= \eta_i [\text{mirror loss} / (\text{internal loss} + \text{mirror loss})] \\ &\approx \eta_i \left\{ (1/L) \ln(1/R) / [\alpha + (1/L) \ln(1/R)] \right\} \end{aligned} \quad (5.8)$$

Here η_i is the internal differential quantum efficiency and indicates the ratio of photons generated in the active layer to the carriers injected. This value typically ranges between 60-90% and will drop with degradation. Thus three factors contribute to reduction of the external quantum efficiency during operation, the reduction of η_i , the increase in mirror loss at the facets, and the increase of internal loss due to dark area defects. To relate this to measurable values, the slope efficiency and external differential quantum efficiency are related as

$$\eta_s = 1/2(h\nu / q) \eta_d \quad (5.9)$$

V.1.2. Power Measurement Justification. Having demonstrated the need for power measurements as a function of current, the next step demands demonstrating that

the power measurements obtained actually reflected the output of lasers analyzed. This development depends on the location of the power detector and the divergence of the lasers. Thus a development of the divergence angles shall be provided and related to the measurement set up employed throughout testing.

Most optical beams propagate in free space as almost pure transverse electromagnetic waves. Verdeyan (20:62) begins with the divergence equation of an electric field in free space, $\nabla \cdot E = 0$, and develops the mathematical description of the fundamental transverse electric field. The observed spatial patterns depend on the intensity of the optical beam and thus on the square of the amplitude factor of the electric field,

$$I(x, y, z) \propto |E(x, y, z)|^2 = E_0^2 \frac{w_0}{w(z)} \exp\left[-2 \frac{r^2}{w^2(z)}\right] \propto I_0 \exp\left[-2 \frac{r^2}{w^2(z)}\right] \quad (5.10)$$

For this equation, 'z' is the distance along the axis of propagation, 'r' is the radial distance from the axis of propagation, and 'w', the spot size, is the radial distance at which point the electric field is 1/e of the electric field at the optic axis. Equivalently, 'w' is the point at which the amplitude of the intensity is 1/e² of the intensity at the optic axis. The minimum 'w' is known as 'w₀', the waist of the beam, and also serves as the reference point for z = 0.

In Verdeyan's development of the beam, he demonstrates how the spot size depends on the distance of propagation and the waist:

$$w^2(z) = w_0^2 \left[1 + \left(\frac{\lambda_0 z}{\pi n w_0^2} \right)^2 \right] \quad (5.11)$$

Here ' λ_0 ' is the (central) wavelength and ' n ' is the index of refraction for the uniform medium that the wave propagates through. By definition the far field of a coherent beam occurs where the second argument in brackets is much greater than one. In this area the spot size relation simplifies; $w(z) \propto z / w_0$. For the measurements taken in these studies

the waist, and hence $z = 0$, is assumed to occur virtually at the front edge of the device and all measurements are made in the far field of the optic beam.

The half-width divergence angle, θ , is defined as the angle subtended by $r = w(z)$ and z in the far field. In other words, for the far field, the half-width divergence angle is:

$$\theta = \arctan \frac{w(z)}{z} \quad (5.12)$$

Fig. 2 displays this definition.

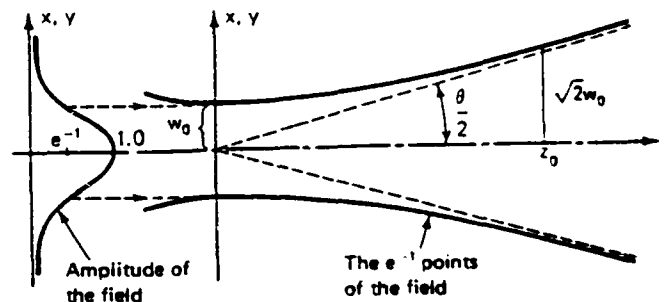


Fig. 2 (20:70) Spreading of a TEM mode.

The half-width divergence angle defines the area in a given reference plane that will contain 95% of the power generated by the laser. This can be calculated by integrating the intensity across the spot size of a reference plane and dividing by the integrated intensity over the entire reference plane.

This discussion has tacitly assumed that the laser cavity is cylindrical and the waist and spot size are circular. Semiconductor lasers, unless careful and complex fabrication steps are added, have laser cavities with rectangular cross sections as do the lasers studied here. In consequence, the output beam is elliptic. Fig. 3 portrays a simple ridge emitting semiconductor laser. An elliptical divergence means that there are two divergence angles.

be determined. To obtain these angles, treat the maximum and minimum observed axes as independent scenarios and employ the above equations. As mentioned previously, the waist is assumed to occur at the front edge of the device. The waist of the minimally divergent orientation approximately equals the width of the active cavity and the waist of the maximally divergent orientation approximately equals the thickness of the cavity.

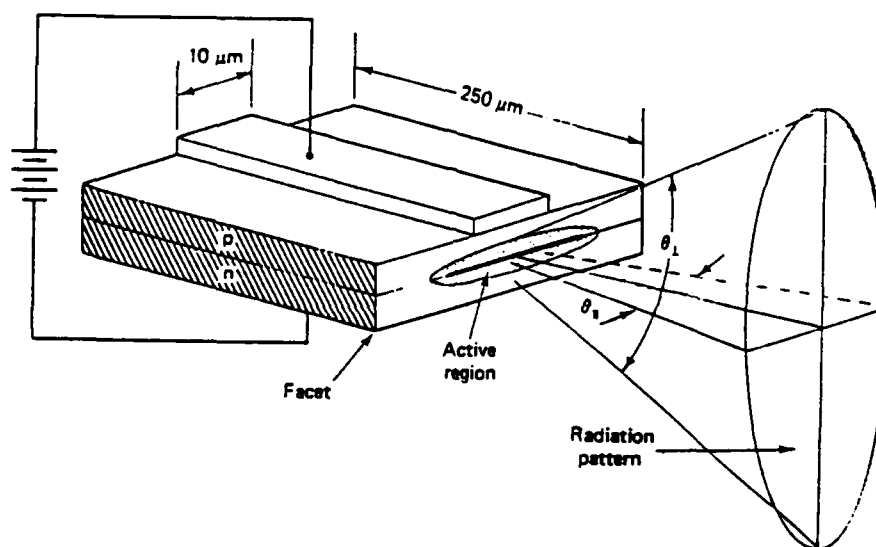


Fig. 3 (20:362) A generic edge emitting semiconductor laser

The lasing cavity dimensions will be based on the active layer thickness and the width of the p-contact of the design. As previously mentioned, not all the light is contained in the active layer of a semiconductor laser and the containment factor must be incorporated. Assume that the containment factor is reflected entirely in the thickness of the active layer. Hence the effective thickness of the cavity is the active layer divided by

the containment factor. It is acknowledged that current spreading occurred, but as this could not be quantified, the width of the cavity shall be taken to be the width of the p-contact for a consistent reference.

As the interest is in the limit on power measurement accuracy, only the maximum divergence angle to be encountered is of immediate concern. The equation for the far field half width divergence angle is obtained from equation (5.11),

$$\theta = \arctan \left[\frac{\lambda_o}{\pi n \left(\frac{ct}{\Gamma} \right)} \right] \quad (5.12)$$

The only new variable, ' ct ', represents the cavity thickness.

Implementing this equation on the testing conducted, the worst case variables are observed as:

$$ct \sim 200 \text{ Angstroms}$$

$$\lambda_o = 980 \text{ nanometers, the longest wavelength observed.}$$

Other relevant variables are:

$$n = 1.0 \text{ the refractive index of air, the medium of propagation,}$$

$$\Gamma = 0.2 \text{ the typical confinement factor of a InGaAs laser structure.}$$

These values produce a half width divergence angle of $\theta = 72^\circ$. Thus the maximum radius of the elliptic power envelope, r_{\max} , taken at 0.5 cm from the leading edge of the laser, becomes:

$$r_{\max} = z \cdot \tan(\theta) = 0.5 \text{ cm} \cdot \tan(72^\circ) = 1.6 \text{ cm} \quad (5.13)$$

This value is smaller than the radius of the detectors employed and thus the meter readings are valid.

V.1.3. Sample Characteristic Power Curve. This section runs through a typical calculation of the characteristic power curve. Such calculations were conducted any time a significant change in the performance of a laser was suspected. This example used laser 66B immediately after it had completed the pre-aging stage. Measurements were taken at room temperature, 24.5°C, and the power meter was calibrated to $\lambda = 960\text{nm}$. Appendix 10 provides the corresponding calculations.

First, the measured powers and corresponding currents were distinguished by prefixes sighting the conditions of operation. For this case, the label was IR66B, to sight this as the initial room temperature characterization. The two letter prefixes variables are below:

Variables	Conditions
I,S,F	Initial, Secondary (intermediate), Final
E,R	Elevated temperature, Room temperature

From the array of powers and current, a least mean squared linear fit to all powers above 1mW was generated to determine the slope and threshold current. These functions were termed "slp", and " I_0 " respectively. The two functions generated the linear power curve as (x is the current):

$$r_{lin}(x) = slp * (x - I_0) \quad (5.14)$$

Bevington's technique was incorporated to determine the margin of error in the slope and the threshold current (22). The 5% absolute accuracy of the Coherent Fieldmaster power meter and a 1% absolute accuracy for the current meters were employed in this error analysis.

V.1.4. Characteristic Power Curve Summary. This section presented the theory and measurements used to develop a linear function of the power output as a function of

drive current. In this justification, the theoretical model for the slope efficiency and threshold currents were outlined. Also, to determine that power measurements accurately obtained all output, the divergence angle for a laser cavity was developed and applied to the measurement setup used for analysis. Finally, an example of the typical calculations made to characterize a laser was provided.

V.2. The Operational Lifetime of a Laser

Chapter I defined the failure of a device to be either the point at which, for the given set of operation conditions, 1.5 times the current required initially was necessary to maintain a constant power output, or the laser quit lasing entirely. The time between initial operation and the point of failure was termed the lifetime of the device. Further development demonstrated that the lifetime depended on power output exponentially, or as an equation:

$$life = A_p P^{-n} \quad (1.2)$$

This calculation dictated the current measurement of multiple devices operated at 5, 7, and 10mW at 100°C until the device failed or a linear extrapolation for the lifetime could be determined from the measurements.

V.2.1. Extrapolated Lifetime. Several devices did not fail in the time exposed to 100°C and as a result their lifetime had to be linearly extrapolated from the measurements available. This subsection demonstrates the curve fitting employed on one such device, laser 54C. Appendix 11 provides a complete sample of the implementation on laser 54C.

The data array for this line fit came from the currents measured and their corresponding time of measurements. The data array label, R54C5, indicated that the laser operated on mount R at 5mW. Typically a second array, R54C5a, was entered to

conveniently observe all data at once. As the standard of failure is proportional to the initial current, all current measurements were normalized to the minimum observed current. Using the sample, row 1 of R54C5 became cR54C5. The minimum current was employed as lifetime measurements indicate the effects of degradation and quite regularly the lasers improved initially. This initial improvement indicates that pre-aging at room temperature proved insufficient for stabilizing the operation at 100°C.

The next manipulation converted the time of measurement to the elapsed operation time measured in minutes. Using the sample, row 2 of R54C5 became tR54C5. With the normalized current and the elapsed time, using generalized array arguments "t" and "r", Mathcad generated the least mean squared linear fit and generated the slope, slp, and vertical intercept, C₀. The intercept should approach 1.0 due to the normalizing of currents and the fact that the minimum current should have occurred at or near the beginning of operation. The intercept for laser 54C was C₀ = 0.998, demonstrating the high agreement. These two component generated the linear model to interpolate the time of failure:

$$rlin5(ot) = slp * ot + C_0 \quad (5.21)$$

Here "ot" stands for operation time. The standard deviation for "ot" arose from dividing the standard deviation between the measured data points and the linear regression by the slope of the linear regression. This term was labeled "st". The lifetime then was calculated as that time generating a normalized current equal to 1.5. The lifetime calculated for laser 54C and "st" are below:

$$lifetime \pm \Delta st = 3300 \pm \Delta 32 \text{ minutes}$$

V.2.2. Categories of Operation. Having described the conditions for failure, the analysis produced four categories of device operation. The first category contained those devices that lased throughout their heated exposure and demanded more current at a steady rate over the time exposed. In the data table provided, Appendix 12, these devices are

identified by a "C" after their estimated lifetime, implying a calculated lifetime. Three other devices, 49A, 63B, and 70A, also fell into this category as they required increasing current at a steady rate and actually required 1.5 times their initial current before the elevated exposure ended. The second category contained those devices that lased initially in their exposure but failed during the period and were unable to generate the set power output at any current. Excluding the three devices in the first category, these devices are identified by an "F" appended to their lifetimes. The third category contains those devices that never lased at their elevated temperatures. These devices are identified by "NL" in the power column and "LUM" in columns dedicated to threshold currents in the elevated characterizations. The fourth category contains those devices that could have lased at high temperature but served as control devices instead. These device are identified by "NL" in the power column and have parameters in the threshold current columns for elevated characterizations.

V.2.3. Calculated Lifetime Function. Now that all the variables have been developed, the calculation for the lifetime as a function of power output can be derived. This function inherently depends on the steady degradation of the lasers and thus primarily on only one criteria of failure, the need for 1.5 times the initial current to maintain constant output. In consequence, the lasers that never lased at elevated temperature and those devices that suddenly quit lasing were not incorporated into the calculations. Thus the lasers that fell into the first category were used for calculations. Appendix 12 provides the data base for all four categories of data and thus for the lifetime equation as well.

With these guidelines, 9 valid data points were available from lasers operating at 5mW, 6 data points from lasers operating at 7mW, and one data point from the lasers operating at 10mW. The 10mW data point was not incorporated as it was felt that more data points were required to include 10mW into the calculation and the single data point would not fit the curve generated by the rest of the data. Appendix 13 demonstrates the

math employed to derive the typical lifetime for operation at 100°C. The final equation produced was

$$\text{lifetime } (P) = 1.911 \cdot 10^4 P^{-1.39} \text{ (minutes)} \quad (5.22)$$

V.3. Mechanisms Governing Degradation

As previously described, the analysis generated four categories of lasers based on their operation at 100°C. Research produced three primary mechanisms that would govern the operation and degradation of lasers. These mechanisms were contact degradation, typified by metallic diffusion or short or open circuits that ended operation of the device under any future operating conditions, facet degradation, or catastrophic optical damage, which entailed burning out the facets and shattering the local crystal structure, and dark defects, due to crystal imperfections existing or developing in the active region. Generally high temperature operation demands higher crystal standards than those of room temperature operation. Thus, another plausible cause for some of the data base not to operate at 100°C could be that these device fell in the margin between minimum standards of room temperature and elevated temperature operation. These four scenarios shall be considered along with the measures taken to eliminate or confirm their influence.

V.3.1. Contact Degradation. This mechanism, excluding metallic diffusion, was the simplest to confirm. None of the devices submitted to 100°C exhibited a sudden short or open circuit during operation. For those devices that did fail, typically the failed device luminesced and all lased upon returning to room temperature. The two devices that did not lase at room temperature after exposure to elevated temperature never lased at elevated temperature and hence the combined effect of current and high temperature was not responsible for their damage. Combined current and high temperature were the only

conditions that could cause metallic displacement below the melting points typical of the alloys used in the contacts.

Metallic diffusion of the contacts still represented a possible contributing mechanism for degradation of the lasers. Research implied the operating conditions employed were well below those typical of this mechanism. Fukuda cites studies observing electromigration of Au films operating at $5\text{-}20 \times 10^5 \text{ A/cm}^2$, $200\text{-}300^\circ\text{C}$, for 10-1000 hours (1:142). The lasers in this study generally operated at $5\text{-}8 \times 10^3 \text{ A/cm}^2$, 100°C , for 4-12 hours. Samples have been submitted for future Auger analysis but the general impression is that metallic diffusion and contact degradation as a whole were not influential contributors to the degradation of these devices.

V.3.2. Facet Degradation. Facet degradation provided the next plausible mechanism of degradation. Signs of this mechanism would be either pitted facets or in an extreme case, the destruction of the crystal in the facet region. SEM analysis was used to gain evidence of either results. Laser 49A, a device that failed after 600 minutes was observed and neither facet displayed any damage, Fig. 4.

The facets of lasers 34B, 34C, 38B, and 55A were also observed. Lasers 34B, 34C, and 38B were operated in the trial run of elevated temperature and were not observed for 8 hours. Also, variables were induced as these devices were never characterized beyond the knowledge that they lased at the beginning of elevated exposure. In consequence, these were not incorporated into the general data base. Laser 34B lased at least 280 minutes and laser 34C was a control laser. Laser 38B failed within 25 minutes of operation and was the only device of the three observed to have possibly suffered facet damage from operation, Fig. 5.

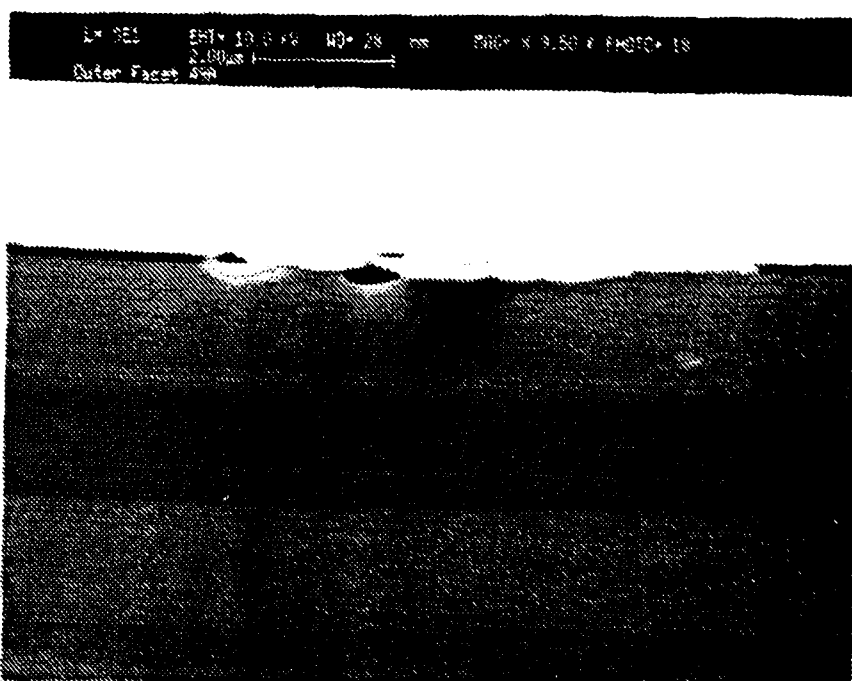
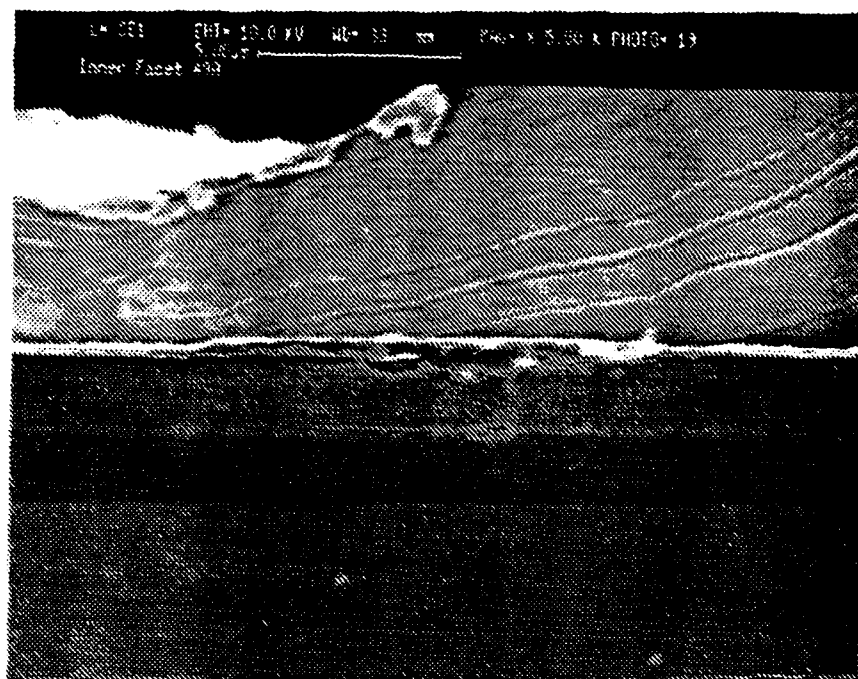


Fig. 4 Inner and Outer Facets of Laser 49A.

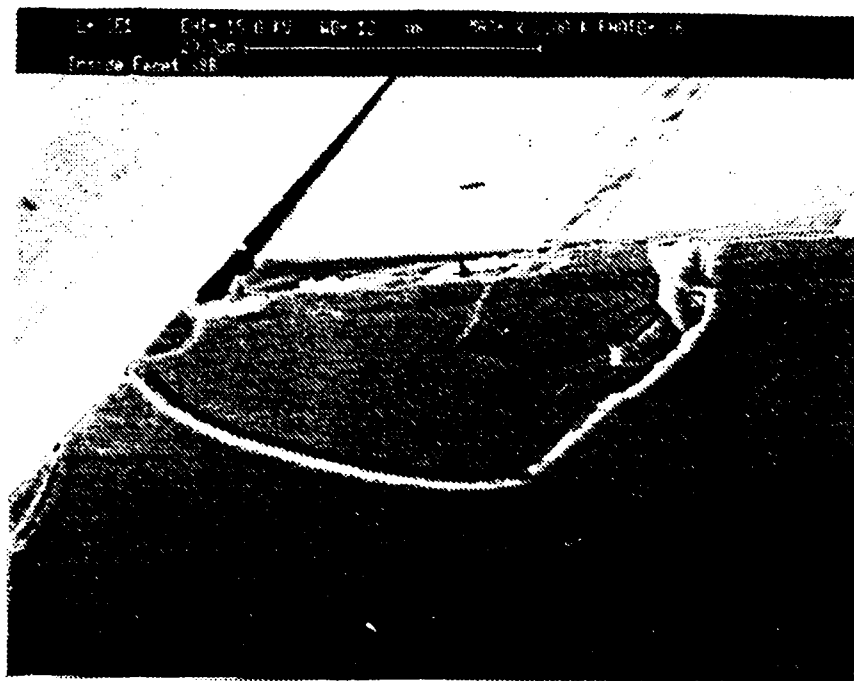


Fig. 5 Inner Facet of 38B, displaying possible facet crystal damage.

The facets' influence on performance was confirmed in tests designed to remove oxide from the surface layer of the facets. Laser 55A was submitted to a 15 second rinse in 10:1 HF acid. This rinse is known to have damaged the facets as the laser performed less efficiently after the rinse.

The overall impression implies that facet damage might have significantly contributed to the failure of the 7 devices with lifetimes shorter than laser 34B but the best means to demonstrate this would demand further SEM analysis. These are the devices that were inherently more stressed and facets already damaged would create more regions to absorb heat and contribute to destruction of the facets. The control lasers and 17 lasers with longer lifetime are not believed to have been strongly influenced by this mechanism.

V.3.3. Dark Defect Degradation. The third mechanism induced by operation stems from crystal defect generation throughout the laser cavity. As the literature review demonstrated, these defects absorb photons and generate heat, reducing the efficiency of the laser and generating more crystal defects to amplify the damage. The only means to observe this possibility directly comes from either scattered electron microscopy, SEM, or transmitted electron microscopy, TEM, analysis. The SEM analysis would only expose the dark defects that reached the facets. These would be observed as small dark spots across the facet surface and would only represent a small fraction of the possible damage within the cavity. Devices have been submitted for future TEM analysis and by selectively thinning the device down to the active layer, dark spots across the exposed region would demonstrate these defects.

Dark defect degradation involves the gradual diffusion and growth of crystal defects toward the hotter regions of the device. As this is a gradual process the most evident sign of the degradation is a steady increase in the current necessary to maintain the desired output. Eventually a defect could grow to breach the active region and cause a short, this would severely reduce output and possibly burn the device. This mechanism regularly serves as the primary cause for degradation in devices that reach the wear-out period of their lifetime.

The acid rinse of laser 55A demonstrated signs of dark defect degradation. After the rinse the device was submitted to SEM analysis. The analysis of the exposed active region demonstrated heavy etch pitting on the device ends. The rinse is known to react vigorously with crystal defects and thus demonstrated the heavy concentration of crystal defects around the active layer of the device. The control device, laser 55B, was subjected to the same rinse and demonstrated little pitting on one facet end and none on the other. While this is only one device, these tests demonstrated that the continuous lasing at

elevated temperature encouraged crystal defect growth, leading to dark defect degradation.

Fig. 6 displays the facets of laser 55A and 55B.

Several reasons imply that this was the primary cause of degradation in this lifetime study. First, virtually all literature involving reliability analysis encountered dark defects as a contributor to the degradation of their devices. Second, over half the data base demonstrated the linear increase of current necessary to maintain power. Finally, as the other two primary mechanisms were effectively dismissed, this mechanism, though explicitly proven as the cause on only a single device, remains the only primary degradation mechanism to account for the decay of the lasers' performance.

V.3.4. Lasers Inoperational at Elevated Temperature. One category of lasers never could experience degradation at high temperature as they never could lase during such exposure. Sixteen of the fifty two devices analyzed could only luminesce at 100°C.

Typical thermal influence on laser operation dictates energy band spreading, causing higher threshold currents and lower slope efficiencies. This trend can only extend to the point when carrier saturation occurs before a round trip gain can exceed one to obtain lasing. Upon reaching this point the device can never lase and will only luminesce. The gain equation depends upon the absorption coefficient of the medium and the geometry of the cavity. Although the elevated temperature would exacerbate the difference in performance between devices with different absorption coefficients and differing cavities, both temperature settings should exhibit traits highlighting their inferior performance.

Working on this premise, the characteristic curves gained at room temperature were compared throughout the data base. The only significant distinction arose in the threshold currents. The threshold current for devices that could not lase at 100°C averaged at 53mA before exposure, almost 8mA above the cumulative average of 45.2mA. After

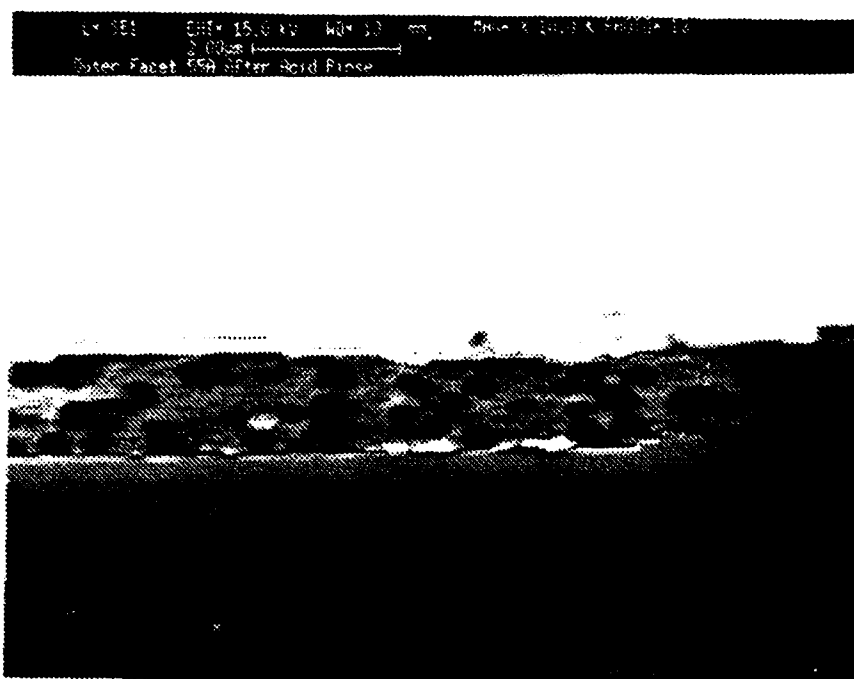
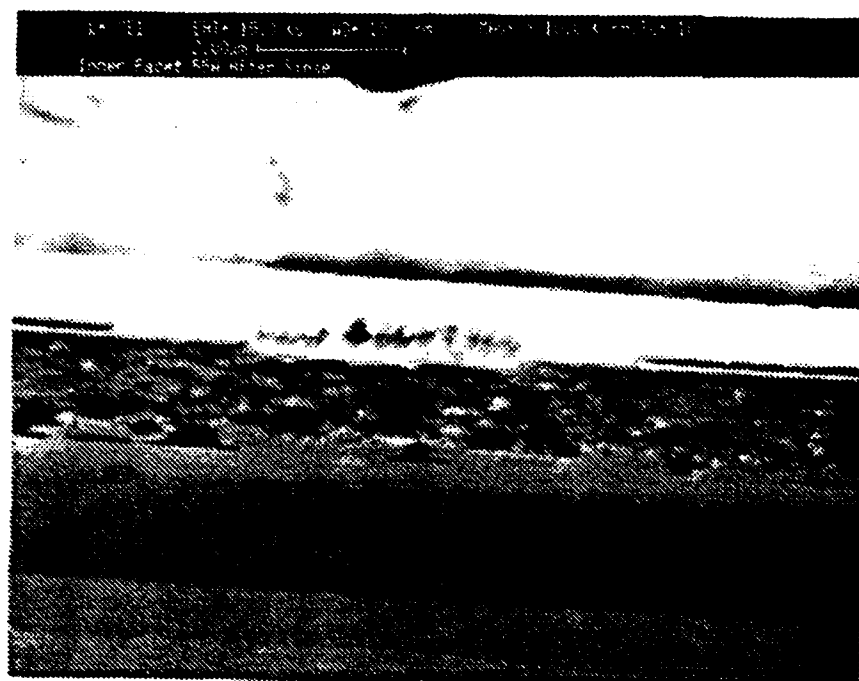


Fig. 6a Inner and Outer Facets of 55A, after HF rinse.

exposure this difference grew to 56.7mA vs. 47.2mA. Two devices, 41A and 66A, demonstrate this observation particularly well as both had threshold currents above 85mA and slope efficiencies below 0.19, 32% below the average slope efficiency of 0.28.

To address the geometry of this group of devices, laser 45A was examined under SEM analysis. The facet planes for this device were observably non-parallel (Fig. 7). Non-parallel facets dictate that a reduced portion of each facet will reflect photons back through the cavity and on to the opposite facet. This requires more current to generate the same net output for a cavity with parallel facets of the same dimensions. Returning to laser 45A's room temperature characteristic curves, the threshold current was 63.1mA before exposure and 73.8mA after exposure, well above the averages cited previously.

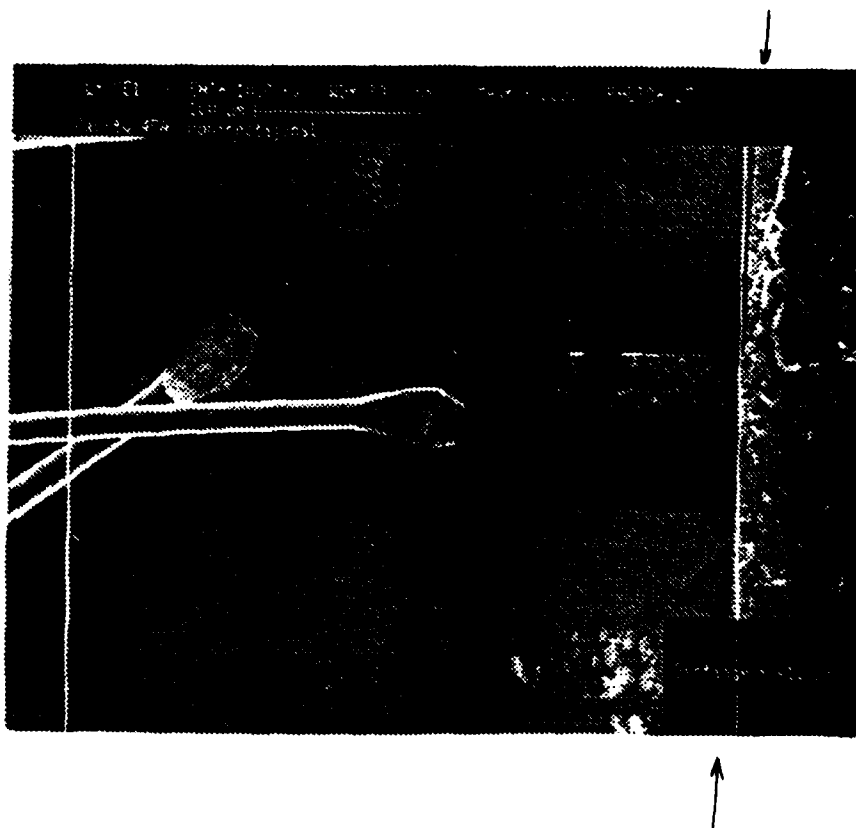


Fig. 7 The non-parallel facets of laser 45A.

Additional factors that could influence this distinction could arise from excessive crystal defects evolving during fabrication and facet damage during cleaving. As SEM analysis could not be performed on all devices, the role of facet damage could not be determined. Devices were submitted for future TEM analysis to determine if significantly more crystal defects were present in this category of devices over the rest of the data base.

V.3.5. Degradation Mechanism Summary. Four general characteristics were explored for their influence on laser degradation. Two of the three degradation mechanisms, contact degradation and facet degradation, were observed to be minor contributors to the decay of all but 7 of the 52 devices analyzed. Dark defect degradation, inherently the most difficult to verify, remained as the suspected primary degradation mechanism. The fourth area observed involved comparing the devices that could never lase at 100°C to the rest of the data base. These devices demonstrated higher threshold currents and at least one device was observed to have non-parallel facet planes. Both observations are indicative of inherently less efficient lasers. Thus an argument was made and demonstrated that these devices, while satisfying standards to induce lasing at room temperature, did not demonstrate high enough standards for lasing at 100°C.

V.4. Data Summary

This section presents the average characterization of the devices based on their various operation conditions. The devices are further grouped by their output during their elevated temperature period. These curves are used in later development to cite trends found in the data. The cumulative average absolute error for currents was $\pm 1.58\%$ and the cumulative average absolute error for the slope efficiencies was 3.78%. Table I provides the average threshold currents and slope efficiencies of the devices as grouped by their

operating categories. The characteristic equations and their curves for each category of operation are below (Fig. 8a-f). The characteristic equation in the general format is:

$$P(I) = \eta_s \cdot (I - I_{th}) \quad (5.23)$$

Where P is the power output, I is the current, I_{th} is the threshold current, and η_s is the slope efficiency.

a) Devices unable to lase at 100°C, "Luminescent Devices" (16 devices)

	Threshold Current (mA)	Slope Efficiency (W/A)
Initial R. T. Characterization	53.04 ± 1.51 (2.84%)	0.287 ± 0.134 (4.66%)
Final R. T. Characterization	56.72 ± 0.406 (0.716%)	0.360 ± 0.0073 (2.04%)

b) Devices run at 5mW constant output (10 devices)

	Threshold Current (mA)	Slope Efficiency (W/A)
Initial R. T. Characterization	36.53 ± 1.31 (3.60%)	0.248 ± 0.0128 (5.02%)
Final R. T. Characterization	42.41 ± 0.767 (1.81%)	0.336 ± 0.0094 (2.81%)
Initial 100°C Characterization	76.87 ± 0.399 (0.519%)	0.489 ± 0.0125 (2.55%)
Final 100°C Characterization	85.43 ± 1.06 (1.25%)	0.288 ± 0.0139 (4.82%)

c) Devices run at 7mW constant output (5 devices)

	Threshold Current (mA)	Slope Efficiency (W/A)
Initial R. T. Characterization	43.02 ± 0.467 (1.09%)	0.324 ± 0.0071 (2.19%)
Final R. T. Characterization	53.30 ± 0.662 (1.24%)	0.395 ± 0.0135 (3.40%)
Initial 100°C Characterization	88.74 ± 0.569 (0.641%)	0.465 ± 0.0152 (3.28%)
Final 100°C Characterization	104.24 ± 1.02 (0.974%)	0.294 ± 0.0180 (6.11%)

Table I (a-c) Characterizations as grouped by the operational history.

d) Devices run at 10mW constant output (3 devices)

	Threshold Current (mA)	Slope Efficiency (W/A)
Initial R. T. Characterization	43.37 ± 0.878 (2.02%)	0.274 ± 0.0071 (2.60%)
Final R. T. Characterization	50.63 ± 0.641 (1.27%)	0.335 ± 0.0078 (2.34%)
Initial 100°C Characterization	81.83 ± 0.454 (0.555%)	0.371 ± 0.0085 (2.30%)
Final 100°C Characterization (1 device only)	70.70 ± 0.543 (0.768%)	0.375 ± 0.0084 (2.24%)

e) Control Devices (13 devices)

	Threshold Current (mA)	Slope Efficiency (W/A)
Initial R. T. Characterization	43.01 ± 1.38 (3.21%)	0.272 ± 0.0141 (5.19%)
Final R. T. Characterization	41.23 ± 1.56 (3.77%)	0.265 ± 0.0134 (5.05%)
Initial 100°C Characterization	79.13 ± 0.459 (0.580%)	0.466 ± 0.0113 (2.42%)
Final 100°C Characterization	79.62 ± 0.609 (0.765%)	0.467 ± 0.0170 (3.64%)

f) Cumulative Characterization of Entire Data Base (53 devices *)

	Threshold Current (mA)	Slope Efficiency (W/A)
Initial R. T. Characterization	45.20 ± 1.29 (2.86%)	0.279 ± 0.0138 (4.96%)
Final R. T. Characterization	47.16 ± 0.893 (1.89%)	0.333 ± 0.0105 (3.15%)
Initial 100°C Characterization	81.82 ± 0.462 (0.565%)	0.486 ± 0.0125 (2.58%)
Final 100°C Characterization	95.93 ± 0.958 (0.998%)	0.384 ± 0.0170 (4.41%)

* 6 devices were run at multiple outputs to examine the effects of this on degradation. These devices were not included in any group other than the cumulative characterization.

**Table I (d-f) Characterizations of devices as grouped by the operational history
(continued).**

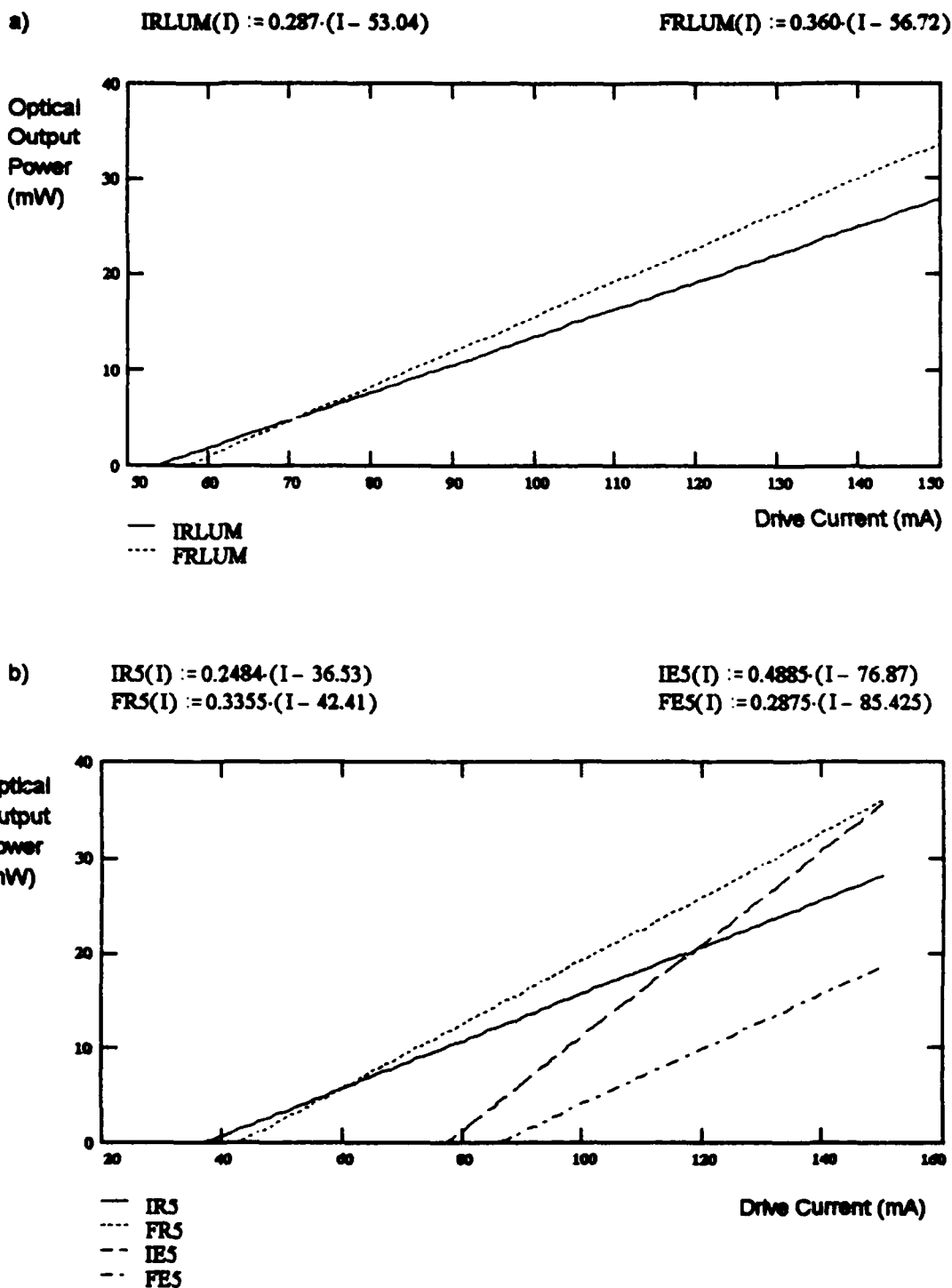


Fig. 8 a) Initial and Final room temperature average characterizations of the luminescent category of devices. ($\Delta I = \pm 1.78\%$, $\Delta \eta_s = \pm 3.35\%$)

b) Average characterizations at room temperature and 100°C for devices aged at 5mW. ($\Delta I = \pm 1.79\%$, $\Delta \eta_s = \pm 3.80\%$)

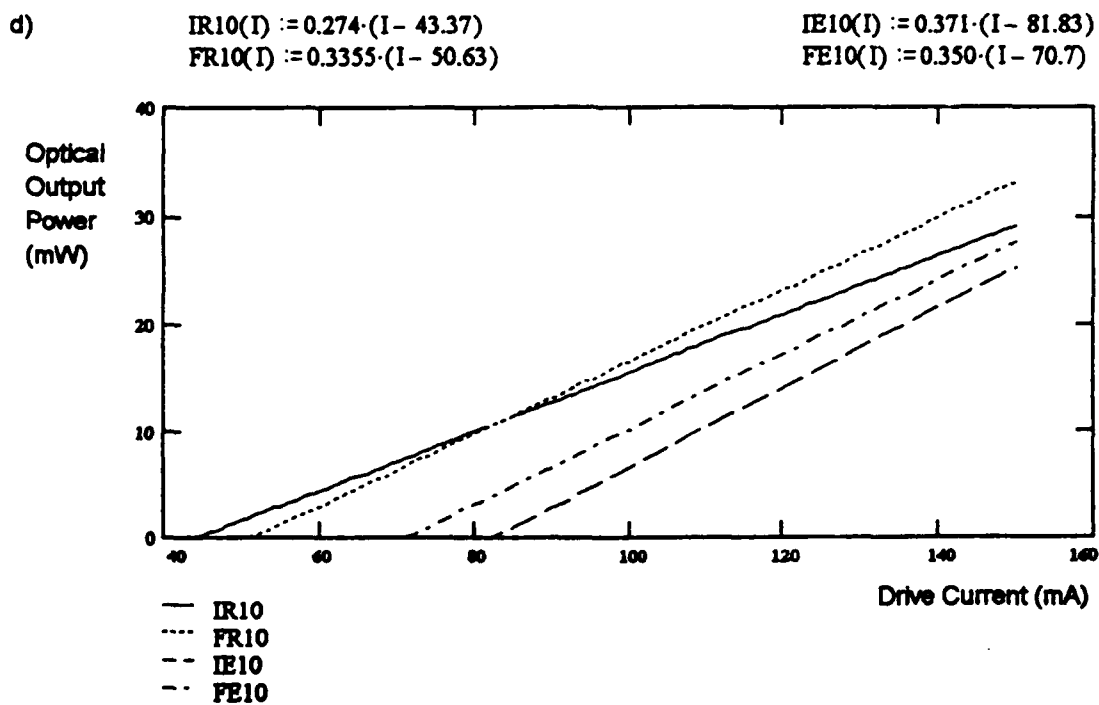
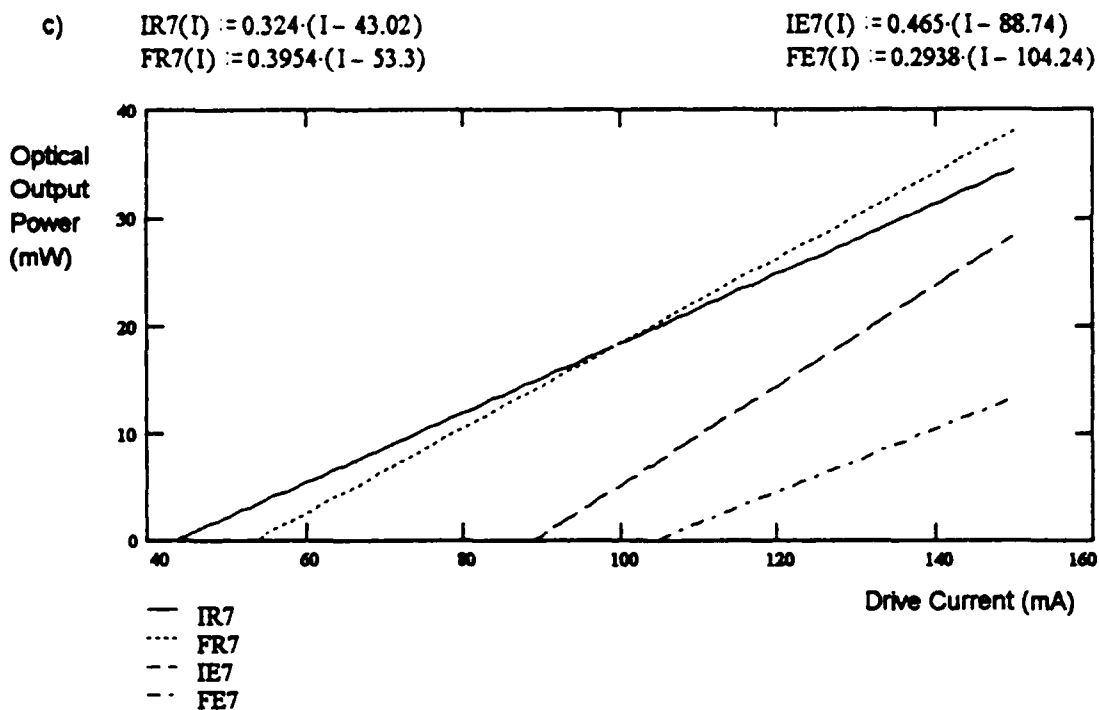
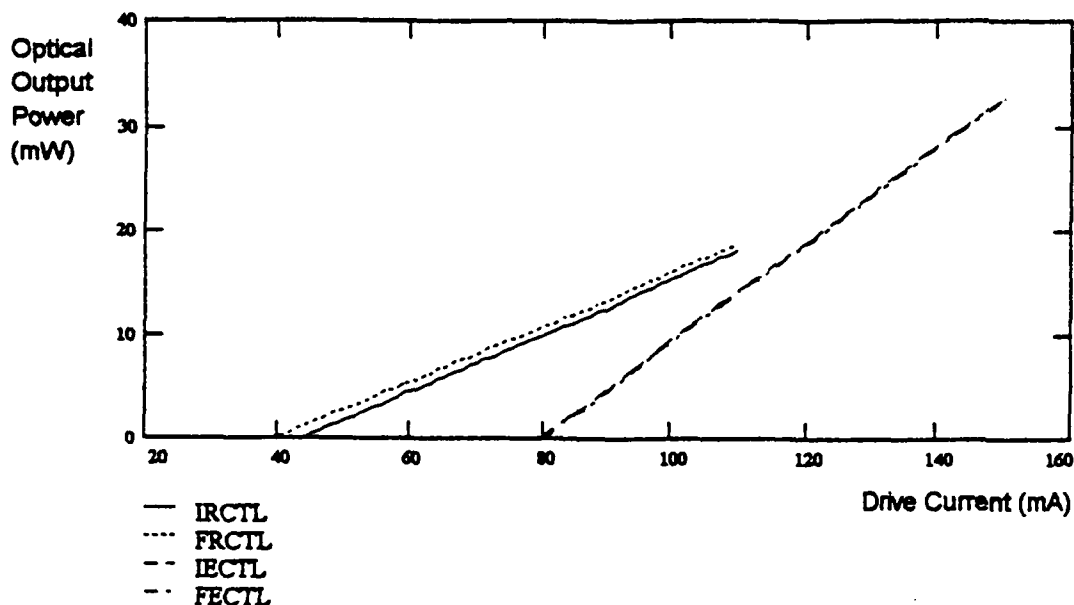


Fig. 8 c) Average characterizations at room temperature and 100°C for devices aged at 7mW. ($\Delta I = \pm 0.986\%$, $\Delta \eta_s = \pm 3.75\%$)

d) Average characterizations at room temperature and 100°C for devices aged at 10mW. The final 100°C characterization reflects only one device. ($\Delta I = \pm 1.15\%$, $\Delta \eta_s = \pm 2.37\%$)

e) $IRCTL(I) := 0.272 \cdot (I - 43.00)$ $IECTL(I) := 0.466 \cdot (I - 79.13)$
 $FRCTL(I) := 0.265 \cdot (I - 38.92)$ $FECTL(I) := 0.467 \cdot (I - 79.62)$



f) $IRWHL(I) := 0.2785 \cdot (I - 45.2)$ $IEWHL(I) := 0.486 \cdot (I - 81.82)$
 $FRWHL(I) := 0.333 \cdot (I - 47.16)$ $FEWHL(I) := 0.378 \cdot (I - 86.8)$

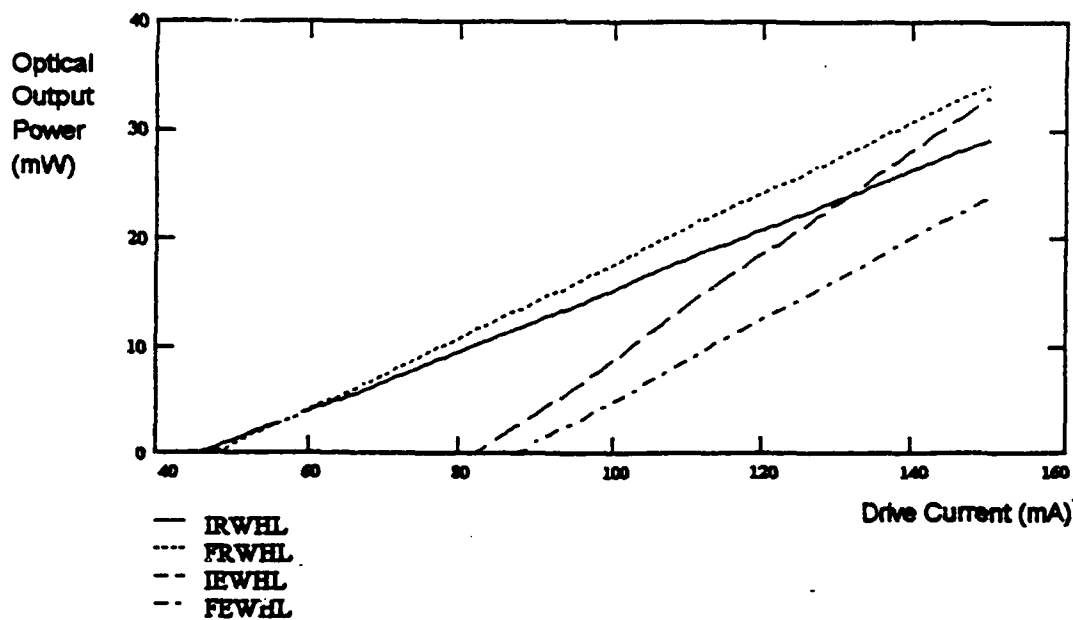


Fig. 8 e) Average characterizations at room temperature and 100°C for control devices.

Note that initial and final 100°C characterizations are identical.

$(\Delta I = \pm 2.08\%, \Delta \eta_s = \pm 4.08\%)$

f) Average characterizations at room temperature and 100°C for the data base as a whole. $(\Delta I = \pm 1.58\%, \Delta \eta_s = \pm 3.78\%)$

V.5. Improved Performance at Elevated Temperature

An anomaly to general laser theory arose in the characterization of the lasers that functioned at 100°C. Theory and previous studies demonstrate that as the operating temperature of semiconductor lasers increase, the threshold current rises and the slope efficiency drops. While all devices that functioned at elevated temperatures demonstrated the increase in threshold current, the cumulative average slope efficiency rose from 0.279 ± 0.014 W/A, taken at the initial room temperature characterization, to 0.486 ± 0.013 W/A, taken at the initial elevated temperature characterization. Neither an overestimate of the wavelength drift, inducing at most a 2% error, nor the 3.78% absolute error in data measurements can account for this large a difference between slope efficiencies.

Even if no wavelength drift existed, the elevated temperature slope efficiency would be reduced only by 2%. This error was observed by assuming no drift and calibrating the Fieldmaster power meter to $\lambda = 960\text{nm}$, the room temperature setting, and taking measurements at the elevated temperature. The power meter was immediately recalibrated to $\lambda = 980\text{nm}$, the elevated temperature calibration, and measurements on the same current settings as with the previous calibration were recorded.

If error can not account for this consistent increase in slope efficiency, the remaining options involved a significant change in the cavity structure. Suggested changes not inherent to typical laser operation included additional annealing, the growth of a facet oxide to improve reflectivity, an improvement of contacts, and the reduction of stress on the cavity induced by the mounting epoxy. A final suggestion involves the improvement of the internal quantum efficiency due to a mismatch of lattice constants and coefficients of thermal expansion between layers.. After a brief review of the history of the devices, the efforts taken to account for each of these possible causes are outlined.

As it is quite possible that the operational history of the devices may have influenced this anomaly, a review of how the devices were treated after fabrication and up to the characterization at elevated temperature follows. Upon receiving the devices, each was briefly tested to see which produced an output above 1mW. This testing drove each device for no more than 5 minutes at currents under 150mA. Next, the devices able to lase were pre-aged at room temperature, 23-27°C, generating between 1.5-7.0mW for a period between 2-16 hours with a mean of 10.7 hours. After pre-aging the initial room temperature characterizations were conducted, typically running each device for 30 minutes at 7mW and momentarily up to 12mW. Then all devices experienced a gradual increase to 100°C over a period of 45-100 minutes. The devices were not lasing during this period. Upon stabilizing at 100°C the devices were characterized again, lasing between 5-10mW for 10 minutes and momentarily up to 15mW. The measurements from both characterization sessions represent the data base for the unexpected improved slope efficiency observed.

V.5.1. Additional Annealing Effects. The first proposed mechanism to account for improved lasers reasons that annealing might have occurred during the gradual increase in temperature. This annealing would reduce the crystal defect density, improving the crystal quality of the active layer and reducing the absorption coefficient of the laser. This inspired questions to the sponsor on details in fabrication. During fabrication these devices experienced a thermal spike up to 525°C with a total time of 10 seconds spent above 400°C. This spike was specifically designed for the initial annealing of the devices. Later elevated thermal exposure involved one hour at 225°C to cure the epoxy mounting the devices to the TO-5 packages. This previous exposure to higher temperatures implies that little additional annealing could have occurred during the 40-100 minute gradual increase to 100°C. Note that for all this heating the lasers were not operating so no temperature

gradient existed in the device and thus the dark defects were not attracted toward the active regions as they are during laser operation.

An additional argument against this mechanism arises in that any permanent change to the physical quality of the laser would be reflected in improved performance of the control devices upon returning to room temperature. The control devices demonstrated less than a 1% change in their elevated threshold currents and slope efficiencies throughout their exposure. In comparing the pre- and post-exposure room temperature characterizations, the threshold currents decreased an average of 9.5% and the slope efficiencies decreased only 2%. The change in threshold current could be attributed to some annealing while the change in slope efficiency is easily accounted for by the 3.78% error inherent to the slope calculations. Thus the only permanent change was reflected in the threshold current and the phenomenon observed in the slope efficiencies can not be attributed to any such change in the device.

V.5.2. Improved Facet Reflectivity. The second suggested mechanism reasoned that the gradual baking of the device might have grown an oxide on the facet surfaces. This might be proposed as this was the first time these surfaces were exposed to the air during baking. The argument continued that possibly this layer could improve the facet reflectivity and thus improve laser performance.

In an effort to confirm this influence, device 55A was rinsed in a 10:1 HF acid solution for 15 seconds to remove any such oxide that might have grown. Multiple characterizations, pulsed and continuous wave, were conducted on this device before and after the rinse with the direct aid of the Wright Laboratories/ELR laser laboratory. The pulsed characterizations were necessary as the hardware available for immediate elevated temperature characterizations only ran devices under pulsed current operation. Note that this hardware did not require the 45-100 minute thermal stabilization period required for earlier characterization. All additional hardware used is included in Appendix 4. Table II

below lists the various characterization results and the conditions of each characterization. Characterizations are listed in the sequence of their analysis. The threshold current, I_{th} , units are mA and the slope efficiency, η_s , units are mW/mA.

	A	B	C	D	E	F	G	H	I
I_{th}	37.9	40.0	44.2	42.3	45.9	45.6	57.2	58.2	46.5
η_s	0.436	0.344	0.475	0.266	0.388	0.386	0.284	0.289	0.382

Before HF rinse:

A: Continuous wave lasing, room temperature, before rinse, conducted with hardware used on the bulk of the data base. (All the remaining characterizations are conducted with Wright Laboratory/ELO hardware)

B: Continuous wave lasing, room temperature.

C: Pulsed lasing, 0.024% duty cycle at 200 Hz, room temperature.

After HF rinse:

D: Continuous wave lasing, room temperature.

E: Pulsed lasing, 0.024% duty cycle at 200 Hz, room temperature.

F: Pulsed lasing, 0.74% duty cycle at 200 Hz, room temperature.

G: Pulsed lasing, 0.74% duty cycle at 200 Hz, initial exposure at 100°C.

H: Pulsed lasing, 0.74% duty cycle at 200 Hz, 1039 minutes lasing at 100°C.

I: Pulsed lasing, 0.74% duty cycle at 200 Hz, room temperature.

Table II Multiple characterizations of laser 55A, listed in sequence of analysis.

These results indicate that the HF rinse did damage the facets as the slope efficiencies were lower after the rinse, or that the oxide was removed. SEM analysis

confirmed the facet damage (Fig. 6a, p. 97) The freshly exposed facet surface resulting from the rinse did not demonstrate the same increase. Thus the exposure to elevated temperature did not generate any oxide that enhanced reflectivity on fresh facet surfaces.

Two other arguments discourage this mechanism as the cause for the enhanced slope efficiency. The first argument parallels that encountered in the annealing development. Again, any effect that generates a permanent change in the crystal structure seems unlikely as the control devices did not change during the exposure to elevated temperatures and oxide would have grown on the control facets.

Fukuda supplies the second argument in his development of facet oxidation (1:131). Fukuda argues that facet oxidation is a degradation mechanism as it actually creates crystal defects at the facet surface. These defects become part of the active layer and effectively become dark area defects. These defects reduce the band-gap energy, providing a continuum of energy levels to allow non-radiative recombination. This means the absorption coefficient of the facet increases with oxidation. The net result is that any facet oxidation will degrade the laser. To summarize, a HF rinse on a device in question, the fact that no permanent crystalline change could occur, and the fact that facet oxidation is a degrading mechanism, indicate that no oxide layer could have grown on the facets to improve the overall laser performance.

V.5.3. Improved Contacts. The performance of the contacts can vary with the operating temperature. Diffusion may also occur during elevated temperatures and/or sufficient current density operation. If mild diffusion could generate an improved ohmic contact, it would improve performance for all future operating conditions. One reason for this is simply that diffusion is not a reversible process that would "undiffuse" upon returning to room temperature. The strongest argument against this mechanism is that by definition a good ohmic contact has negligible contact resistance relative to the bulk resistance of the semiconductor (19:169). The voltage drop across the contacts should be

small compared to the drop across the active region of the device. Thus the contacts should not significantly influence the device performance under any conditions.

Assuming that the contacts' influence might be significant, if mild diffusion did occur during the warm-up period between the power characterizations, this would again generate a permanent improvement to the devices and would be reflected in the control devices. Devices have been submitted for Auger analysis to confirm any diffusion effects in the contacts and the devices as a whole.

Addressing the thermal influence on the ohmic contact resistance, Sze develops the specific contact resistance, R_c (19:169). Thermal influence is primarily reflected in contacts involving doping levels below 10^{17} dopants/cm³, where thermionic emission current dominates. This influence is reflected by (19:170):

$$R_c = \frac{k}{qA^*T} \exp \left[\frac{q\phi_{Bn}}{kT} \right] \quad (5.24)$$

The variables involved are the Boltzmann constant, k , the temperature, T , the atomic charge, q , the effective Richardson constant, A^* , and the barrier height, ϕ_{Bn} . This indicates that the resistance of the contact will drop as the operation temperature rises.

Thermionic current effects can not be used for GaAs technology due to "fermi-pinning" dictating a large barrier height of ~ 0.9 eV for all metal-GaAs interfaces (21:717). Thus junctions must involve high doping to induce tunneling current effects.

The contacts used for these devices connected to regions doped at 10^{18} dopants/cm³. This doping is sufficient for tunneling current to dominate over thermionic current effects. Tunneling current specific contact resistance depends on material parameters that are not strongly influenced by the operation temperature. Sze cites the dependence as (19:171):

$$R_c \sim \exp \left[\frac{4\sqrt{m_n \epsilon_s} \phi_{Bn}}{\hbar \sqrt{N_D}} \right] \quad (5.25)$$

The additional variables are the effective mass, m_n , the semiconductor permittivity, ϵ_s , the doping density, N_D , and the reduced Planck constant, \hbar . Thus contact improvement is not a likely contributor to the enhanced performance.

V.5.4. Cavity Stress Reduction. The final proposed mechanism suggested that the epoxy thermal expansion coefficient differed from that of the devices. As a consequence, upon cooling to room temperature after curing at 225°C, a residual stress between the epoxy and device developed. Such a stress could bend the device and theoretically render the facets not quite parallel. The argument continues that by heating the device again, even if not up to the curing temperature, this stress is partially reduced and the facets become increasingly parallel. To quantify the effect of this mechanism the thermal expansion coefficient of the epoxy must be obtained and compared to that of the GaAs substrate.

Two arguments arise against this mechanism, the first being that this effect was not encountered in any of the previous studies and texts reviewed concerning laser operation and reliability. The second argument evolves from the final characterizations obtained from laser 55A. Inspecting Table II, p. 109, reveals that with elevated operation the slope efficiency decreased. As far as the epoxy-semiconductor junction was involved, this environment was identical to previous exposure and yet the enhanced operation was not repeated. In conclusion, this does not seem a likely mechanism responsible for the improved laser operation at 100°C.

V.5.5. Variable Internal Quantum Efficiency. Upon examining the equations that involve the threshold current and slope efficiency of the laser data base and trying to fit them to the observed performance, the best option is that the internal quantum efficiency must behave as a reversible function of temperature. This summary runs through the

variables influencing both characteristics and concludes with an argument for attributing the observations to the internal quantum efficiency changing with the operation temperature.

The data demonstrated an obvious increase in threshold current with temperature increase. This encourages an argument for a contraction in cavity length (L) or a reduction in facet reflectance (R) when examining equation 5.6, repeated below.

$$J_{th} = (d / \beta) \left\{ \left(\frac{1}{\Gamma} \right) \left(\alpha + \frac{1}{L} \ln \frac{1}{R} \right) \right\}^{1/m} + dJ_o \quad (5.6)$$

If either were the dominant mechanism this could generate an increase in slope efficiency also through equation 5.8 and equation 5.9, repeated below.

$$\eta_d \approx \eta_i \left\{ (1/L) \ln(1/R) / \left[\alpha + (1/L) \ln(1/R) \right] \right\} \quad (5.8)$$

$$\eta_s = 1/2(h\nu / q) \eta_d \quad (5.9)$$

Either trend shrinks the quantities (1/L) or (1/R) which are factors in both equations modeling the threshold current and the efficiency. The literature review found no studies ascribing their results to these mechanisms. Also a length contraction due to increased temperature, or a negative thermal expansion coefficient, is only observed at low temperatures for type IV, II-V, and II-VI compounds (23:129). As GaAs, InGaAs, and AlGaAs are III-V compounds, this trait does not exist for the compounds and hence is not possible for the devices.

The next variable is the absorption coefficient of the device. This variable would have to decrease to improve the slope efficiency but this works opposite to the observed increase in threshold current. In fact, as presented earlier, this parameter increases during operation as the dark area defects grow in the active layer.

The remaining variables of the threshold current are curve fitting constants and the thickness of the active layer. The active layer thickness would have to expand to increase the threshold current and does not enter into the slope efficiency calculation so this could easily contribute to the increased threshold current observed and not conflict with the observed increase in slope efficiency.

The only remaining variable is the internal quantum efficiency of the efficiency equations. The control data demonstrates that the slope efficiency increases by a factor of 1.7 with temperature and returns to the initial value when returning to room temperature. This implies that the internal quantum efficiency would have to depend on operating temperature and have to be an elastic function. This could easily be explained in terms of strain relief at the InGaAs/GaAs junctions of the quantum well. Since InGaAs has a larger lattice constant than GaAs, but a smaller coefficient of thermal expansion, an increase in temperature decreases the difference in lattice constants. Table III outlines the data relevant to this argument, providing the lattice constants at room temperature and 600°K, as well as the room temperature coefficient of thermal expansion, α , for GaAs and InAs (23:1317,1321). The values for $\text{In}_x\text{Ga}_{1-x}\text{As}$ vary in a continuous manner between those of the compounds at either extreme.

Compound	Lattice Constant (Å) (300°K)	Lattice Constant (Å) (600°K)	α (10^{-6} K^{-1}) (300°K)
GaAs	5.65325	5.6800	6.63
InAs	6.0583	6.080	4.52

Table III (23:1317,1321). Lattice constants and the coefficient of thermal expansion for GaAs and InAs.

This explanation permits the internal quantum efficiency to act as an elastic function of temperature as the lattice constants will return to their larger mismatch upon

returning to room temperature. As the internal quantum efficiency does not figure into the threshold current density, its improvement does not hamper the trend toward higher threshold current densities at elevated operation temperatures.

The previous argument does not account for the permanent improvement of the threshold current. Actually, mild annealing induced by the combined effect of lasing and elevated temperatures might account for this. This mechanism is reinforced by the improved performance demonstrated by the devices lasing at constant power outputs during their first hour of lasing.

In summary, the section reviewed the material variables influencing the threshold current and slope efficiency to develop an explanation for the increased slope efficiency observed at elevated operation temperatures. After presenting each variables' influences on these characteristics, the best explanation required the internal quantum efficiency to improve at elevated temperatures and return to its original value when the device returned to room temperature. This could occur by reducing the lattice constant mismatch at the InGaAs/GaAs junctions. As GaAs has a smaller lattice constant and a larger coefficient of thermal expansion than the same properties of InGaAs, it was reasoned that the lattice mismatch would indeed reduce as the junction temperature increases. As the mismatch returns upon cooling, this dictates a lower internal quantum efficiency and satisfies the requirements for agreement with the data observations. Thus, a variable internal quantum efficiency can account for the increase of slope efficiency observed at elevated operating temperatures.

V.5.6. Anomalous Improved Performance Summary. After comparing the slope efficiencies of lasers characterized initially at room temperature and then at 100°C, a trend of improved slope efficiency at elevated temperature was observed, contrary to theory and published empirical results. Five mechanisms were suggested and investigated to account for this observation. These mechanisms involved additional annealing, the growth of a

facet oxide to improve reflectivity, an improvement of contacts, the reduction of stress on the cavity induced by the mounting epoxy, and a variable internal quantum efficiency. The first four mechanisms were unable to account for the observation. A primary argument defeating the first three mechanisms involved the fact that any permanent structural improvement would have been reflected in the control devices after elevated exposure. This required improvement was not observed. The variable internal quantum efficiency was able to satisfy all observed data trends. As GaAs has a smaller lattice constant and larger coefficient of thermal expansion than any $\text{In}_x\text{Ga}_{1-x}\text{As}$ tertiary compound, the difference in their lattice constants shrinks with increasing temperature. This results in improving the internal quantum efficiency. Upon cooling, the internal quantum efficiency returns to its initial value as the lattice constants return to theirs. This satisfies the data trends observed. As a result of this analysis, this was the only mechanism developed to account for the improved slope efficiency. This trend deserves future research, even if only to find an error in the method of data gathering.

V.6. Summary and Conclusions

This chapter served to outline the need and justification of the power readings obtained at room temperature and elevated temperature as a function of current. From these measurements, the lasers' performance could be quantified and the influence of various constant power outputs at elevated temperature could be examined. A development of the broadest anticipated divergence patterns demonstrated that power readings measured over 95% of the total optical output.

The first product of these power readings was the characterization of the lasers. This characterization generated the approximate threshold current and slope efficiency for each device before, during, and after exposure to several hours at 100°C. An absolute error of 3.78% was derived for the slope efficiency.

The next product of these measurements was the operational lifetime of the average device as a function of power at 100°C. This development demonstrated that the pre-aging phase conducted at room temperature did not provide entirely stable operation at elevated temperature. This conclusion arises from the fact that multiple devices improved during the first hour of operation before beginning the anticipated degradation. The calculated lifetime was:

$$\text{lifetime} (P) = 1.911 \cdot 10^4 P^{-1.39} \text{ (minutes)} \quad (5.22)$$

Analysis of operation at elevated temperatures generated four categories of devices. Those devices that lased throughout their heated exposure and demanded more current at a steady rate over time formed the first category. The second category contained those devices that lased initially in their exposure but failed during the period and were unable to generate the set power output at any current. The third category contained those devices that never lased at their elevated temperatures. The fourth category contained those devices that could have lased at high temperature but served as control devices instead.

The next step involved deducing the degradation mechanisms that dictated the performance decay. Contact degradation and facet degradation were demonstrated as minor contributors to the degradation. Dark defect degradation remained the most likely mechanism. Devices have been submitted for future Auger analysis and future TEM analysis to provide additional confirmation of this conclusion. The results of these analyses are outside the scope of this work.

In the effort to determine why several devices never lased at elevated temperature, these devices were compared to the rest of the data base. Generally these devices demonstrated a higher threshold current at room temperature. SEM analysis on one such device demonstrated that the facets were not parallel and this would dictate inferior performance to a similar device with parallel facets. Conclusions dictated that inferior

crystal quality could demand additional absorption in the cavity and a non-rectangular cavity geometry would hamper performance.

Next a summary of the characteristic power curves was provided. Graphs representing the average of the devices' slope efficiencies and threshold currents were provided for the various operating conditions tested.

The final topic addressed the unexpected improved slope efficiency observed at elevated operation. Theory and published research implies a lower efficiency with an increase in operation temperature. Four mechanisms were proposed and discredited. These mechanisms involved additional annealing, the growth of a facet oxide to improve reflectivity, an improvement of contacts, and the reduction of stress on the cavity induced by the mounting epoxy. A fifth mechanism, involving a varying internal quantum efficiency, proved able to account for this observation. The higher slope efficiency observed with continuous wave laser operation at 100°C deserves future research.

VI. Conclusions and Recommendations

This chapter summarizes the research conducted to model the high temperature effects on the operation of an edge emitting GaAs quantum well semiconductor laser design provided by Wright Laboratories. Three sections are presented outlining this work. First the research goals and their results shall be outlined. Second, additional observations and conclusions are presented. The third section suggests topics that require further study.

VI.1. Research Goals

The research conducted centered on three goals. The primary goal was to determine the influence of three degradation mechanisms, dark area defects, facet degradation, and contact degradation, on the operation of the lasers at 100°C. Inherent to this goal is the determination of which mechanism dominated the degradation. To achieve this goal, a means of quantifying the operation had to be developed. The second and third research goals filled this role. The second research goal was to characterize the performance of the lasers at different stages of operation at room temperature and 100°C. This characterization took the form of the power output generated as a function of the driving current. The characterizations produces the threshold current and slope efficiency for each stage of operation. The third goal was to determine the operational lifetime as a function of power output at 100°C. This lifetime was based on the standard of a 50% increase from the initial current necessary to maintain a constant power output.

VI.1.1. Degradation Mechanisms. Beginning with the determination of the degradation mechanism roles, contact and facet degradation were demonstrated to be minor contributors, leaving the generation of dark area defects as the primary influence on operational decay. Contact degradation's most obvious signs of influence, an abrupt end to

lasing for all temperatures and currents, was not observed. The operation conditions employed on the data base were considerably shorter and at lower temperatures and current densities than studies found in relevant literature to support an argument for the gradual diffusion of the contacts. Operating conditions did not exceed 16 hours and were conducted at 100°C at typical maximum current densities of $7.75 \times 10^3 \text{ A/cm}^2$. Fukuda cites studies observing electromigration of Au films operating for 10-1000 hours at 200-300 °C and $5\text{-}20 \times 10^5 \text{ A/cm}^2$ (1:142). As this alone will not disprove an argument for diffusion, devices were submitted for future Auger analysis to analyze the material composition profiles of unaged devices and aged devices.

Facet degradation was the next mechanism investigated. Signs of this mechanism would be either pitted facets or in an extreme case, the destruction of the crystal in the facet region. SEM analysis was employed on 5 of 27 devices that demonstrated any degradation to gain evidence of either results. The only device to demonstrate any facet damage suffered a possible facet blowout and had failed within 25 minutes of operation. The device with the next shortest lifetime, 280 minutes, to have its facets observed showed no facet damage. The resulting implication could be that facet damage contributed to the failure of the 7 devices with lifetimes shorter than laser 280 minutes. The best means of determination would entail additional SEM analysis on these 7 devices. The SEM analysis already conducted demonstrated that facet degradation did not contribute to the degradation of the bulk of the data base.

Signs of the final degradation mechanism studied, dark defect degradation, were observed in the bulk of the data base. Over half the data base demonstrated the linear increase of current necessary to maintain power, one such sign of this mechanism. Also, due to a HF 10:1 acid rinse of an aged laser and a control laser, the crystal defect density was demonstrated to be enhanced by laser operation at elevated temperatures. As the other two primary mechanisms were effectively dismissed, this mechanism, though explicitly

proven as the cause on only a single device, remains as the primary degradation mechanism to account for the decay of the lasers' performance.

Thus the first goal was achieved and demonstrated that contact and facet degradation did not significantly influence the degradation of the data base. This focus of study also demonstrated that dark defect degradation dominated as the primary degradation mechanism.

VI.1.2. Laser Characterization. The second goal of this research was to quantify the performance of the lasers of the data base. This study demonstrated the validity of measuring the power output as a function of driving current. The components generated from such characterization are the approximate threshold current and the slope efficiency. This research goal generated the characterization of lasers after approximately 10 hours of pre-aging at room temperature, ~25°C, the characterization upon initial exposure to 100°C, the characterization at the end of exposure to 100°C, and the characterization upon returning to room temperature. Appendix 12 tabulates the threshold current and slope efficiency for each device under each characterization.

VI.1.3. Lifetime Calculation. The third goal was to determine the operational lifetime of this design as a function of power while operating at 100°C. This dictated measuring the current necessary to maintain a constant output power for up to 16 hours while operating at the elevated temperature. As a result of this effort, 9 lasers operating at 5mW, 6 lasers operating at 7mW, and a single laser operating at 10mW were available for this calculation. This development demonstrated that the pre-aging phase conducted at room temperature did not provide entirely stable operation at elevated temperature. This conclusion arose from the fact that several devices improved during the first hour of operation before beginning the anticipated degradation. The calculated lifetime as a function of power was:

$$lifetime (P) = 1.911 \cdot 10^4 P^{-1.39} \text{ (minutes)} \quad (6.1)$$

VI.2. Additional Observations

Two general observations evolved during the course of this study. First, analysis of operation at elevated temperatures generated four categories of devices. Those devices that lased throughout their heated exposure and demanded more current at a steady rate over time formed the first category. The second category contained those devices that lased initially in their exposure but failed during the period and were unable to generate the set power output at any current. The third category contained those devices that never lased at their elevated temperatures. The fourth category contained those devices that could have lased at high temperature but served as control devices instead.

The second observation was an unanticipated trend of improved slope efficiency measure at initial elevated operation. Theory and published research implies a lower efficiency with an increase in operation temperature. All devices that functioned at elevated temperatures demonstrated a cumulative average slope efficiency rise from 0.279 ± 0.014 W/A, taken at the initial room temperature characterization, to 0.486 ± 0.013 W/A, taken at the initial elevated temperature characterization. The 3.78% absolute error produced from data measurements could not account for this large a difference between slope efficiencies.

In the effort to account for this trend, four mechanisms were proposed and discredited. These mechanisms involved additional annealing, the growth of a facet oxide to improve reflectivity, an improvement of contacts, and the reduction of stress on the cavity induced by the mounting epoxy. A fifth mechanism, and the only one able to account for the improved slope efficiency, was the improvement of the internal quantum efficiency due to the fact that the difference between the lattice constants of adjacent layers diminishes with elevated temperatures.

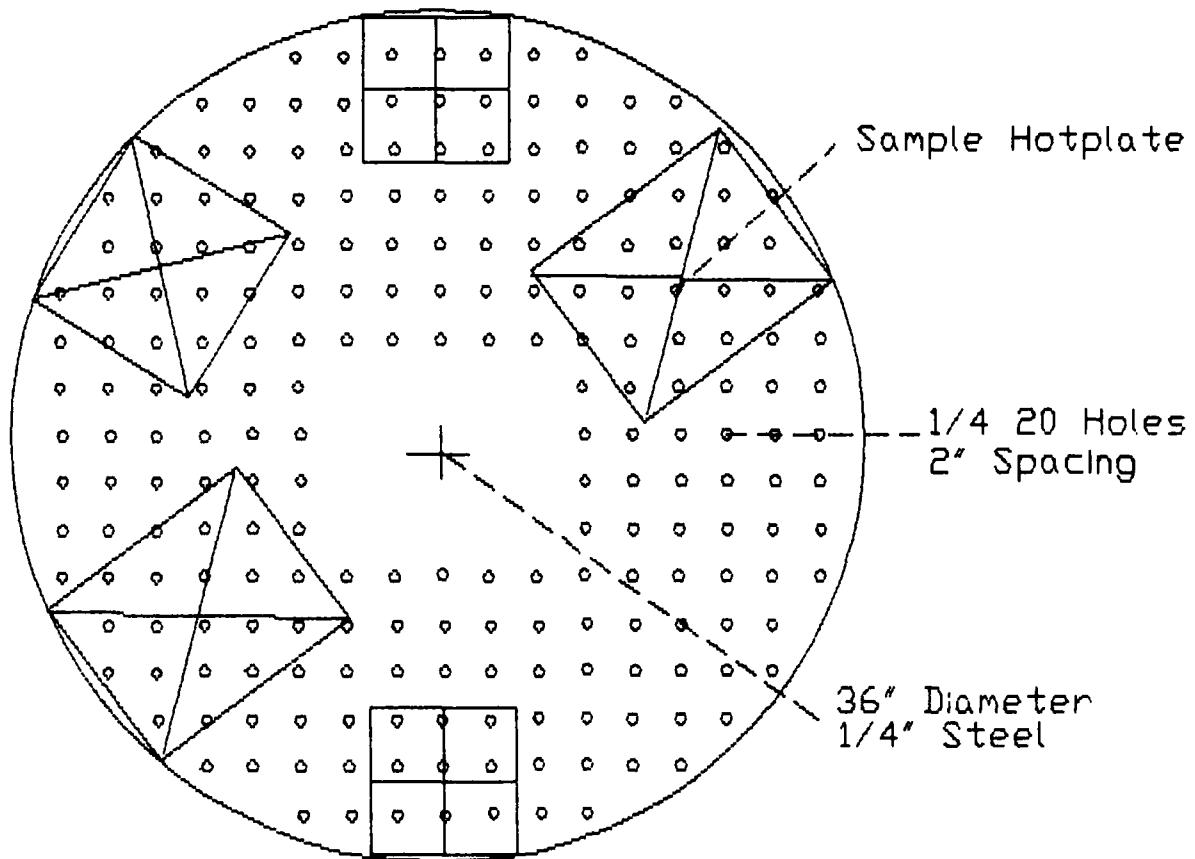
VI.3. Recommendations for Future Research

Two general topics resulting from this research deserve additional study, further confirmation of the influence of the three degradation mechanisms, and the verification of the variable internal quantum efficiency's influence on the increased slope efficiency encountered during initial operation at 100°C. Devices have already been submitted for future Auger analysis which should clarify the extent to which the contacts diffused into the active region during operation. Devices have also been submitted for future TEM analysis to directly observe any crystal defects in the active layer. Finally, SEM analysis should be conducted on the 7 devices demonstrating the shortest lifetimes in the data base to determine if facet degradation contributed to their failure.

Another topic, one that arose in the literature review preparing for this work, involved the facet heating resulting from the duty cycle of the operating current (10:212). Defects that had not been attributed to facet defects implied that the devices being evaluated were operated at either too high an optical power or with an excessively long pulse width in the power vs. current curve measurement. A longer pulse width leads to more energy being applied to facet heating. By increasing the duty cycle and shortening the pulse width the authors effectively reduced degradation from this mechanism. As a larger duty cycle results in more junction heating and a longer pulse width results in greater facet heating, it was concluded that the rate of degradation was dependent on facet heating. Tests similar to these should be conducted on this design to determine the optimal duty cycle and pulse width for minimizing degradation at the elevated operation temperature.

Appendix 1: Steel Plate Carousel Design Diagram

Appendix 1

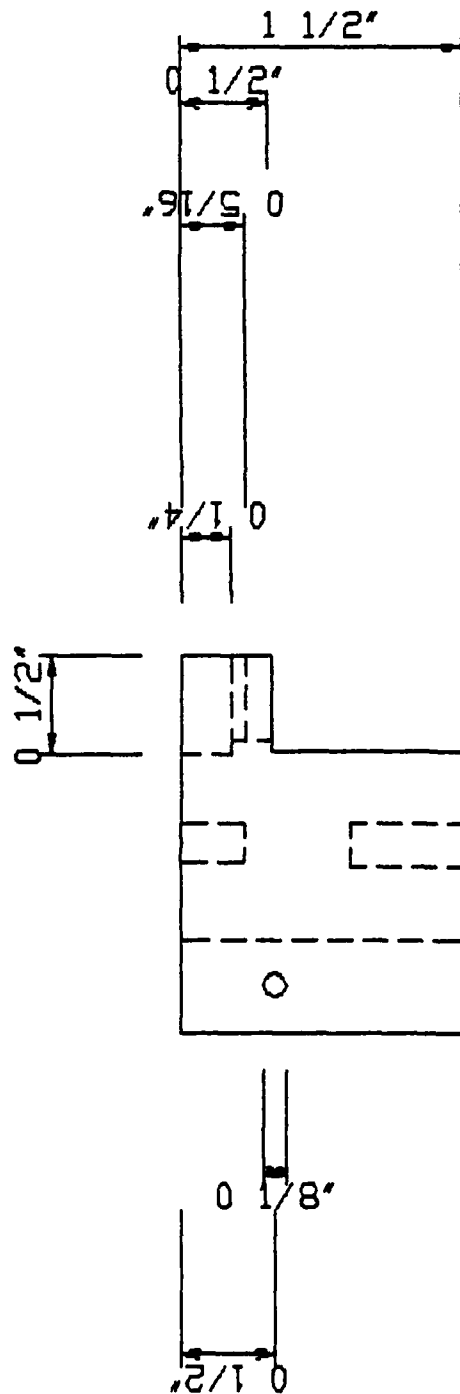


Appendix 2: Laser Mount Design Diagrams

Technical drawing of a mechanical part showing front, top, and side views with dimensions:

- Front View (Top):** A vertical rectangle with a total width of $2''$. It features a central vertical slot with a width of $0.3/8''$ and a depth of $0.1/4''$.
- Top View (Middle):** A circular view showing a central hole with a diameter of $0.7/32''$. The hole is positioned $0.11/16''$ from the top edge and $0.1/8''$ from the bottom edge. The hole is also $0.1/2''$ from the right edge and $0.1/2''$ from the left edge.
- Side View (Bottom):** A vertical rectangle with a total width of $0.1/2''$.

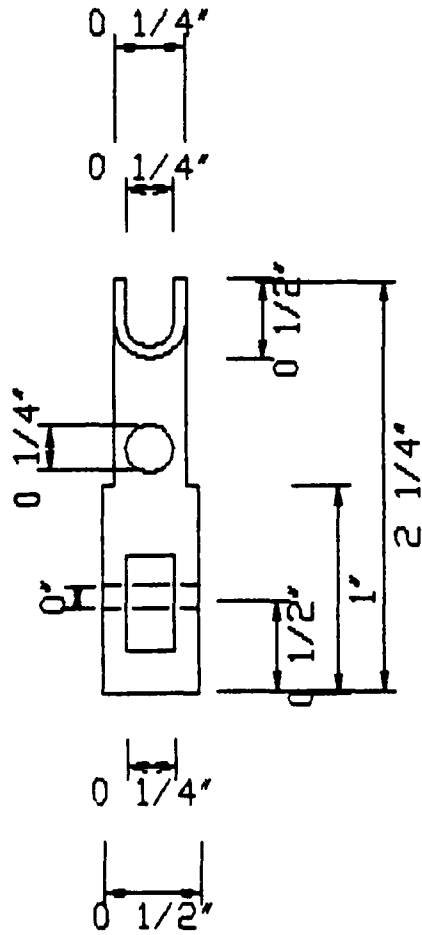
School of Engineering	
Air Force Institute of Technology	
Wright Patterson AFB, OH	
DR. BY:	David Leicester
COURSE	Thesis
DATE:	6 Sept. 93
SCALE:	1:1



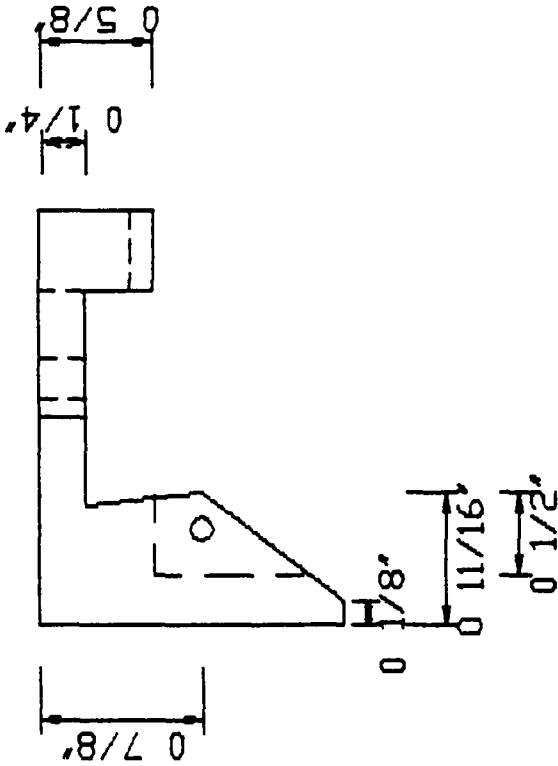
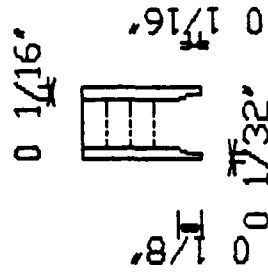
OTHER ITEMS REQUIRED:

1. $1\frac{1}{8}"$ PIVOT AXLE
2. AXLE SPRING

School of Engineering	
Air Force Institute of Technology	
Wright Patterson AFB OH	
DR. BY:	David Leicester
COURSE:	Thesis
DATE:	6 Sept. 93
SCALE:	1:1



FORK'S LIP PROFILE:



School of Engineering
Air Force Institute of Technology
Wright Patterson AFB OH

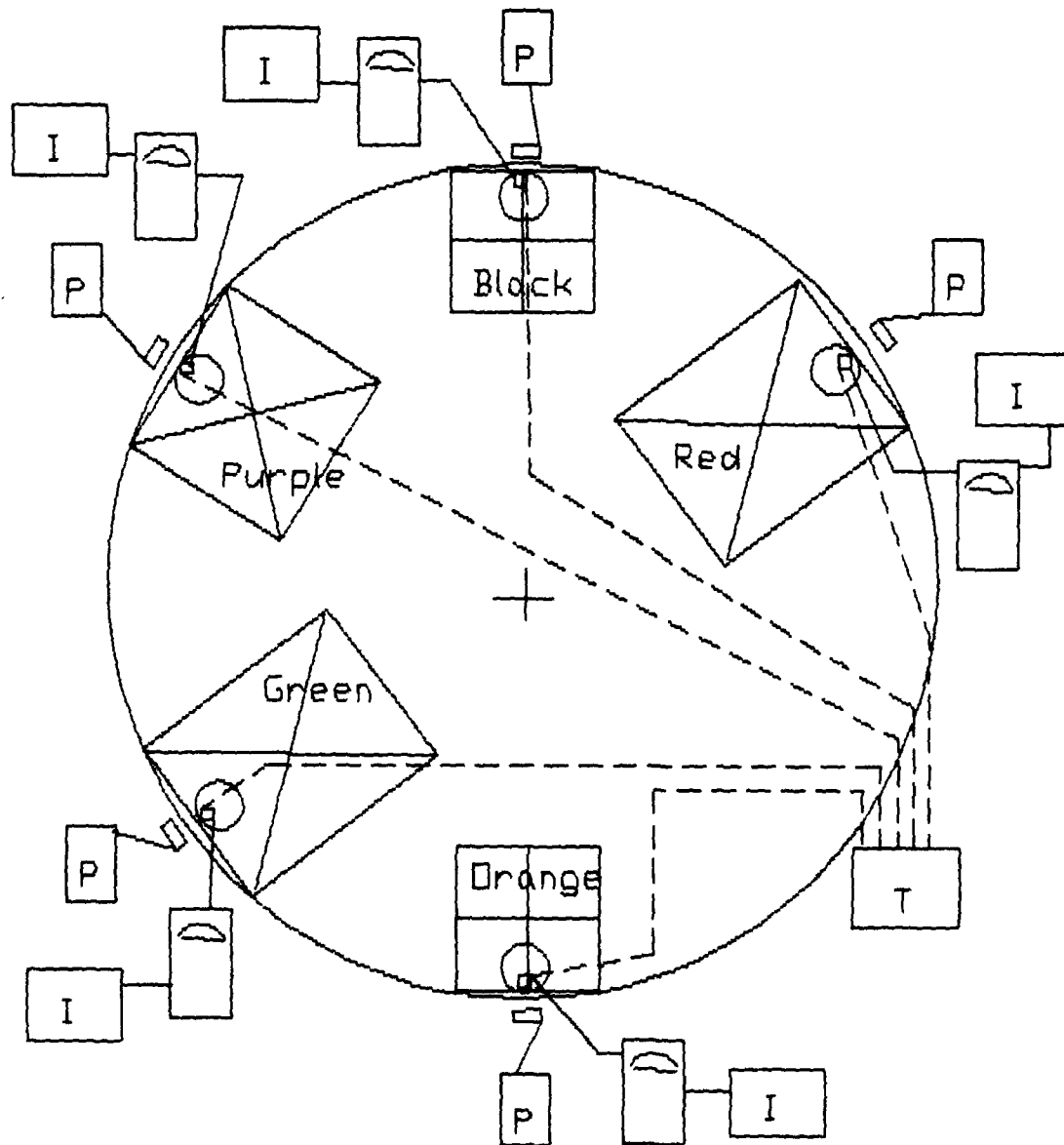
DR. BY: David Leicester

COURSE Thesis

DATE: 6 Sept. 93 SCALE: 1:1

Appendix 3: Power Measurement Block Diagram Setup

Appendix 3



Index:

⊙ Laser/Laser Mount

I Current Source

Current Meter

P Power Meter

T Temperature Meter

Appendix 4: Hardware List

This first list includes the hardware employed for all tests except the final HF acid rinse tests.

(Quantity Item)

- | | |
|---|--------------------------------------------------------------|
| 1 | Loomis Scriber, Model MKT-38-LI |
| 1 | Cole-Parmer Digi-Sense Temperature Controller, Model 2186-00 |
| 1 | Fluke 77/AN Multimeter |
| 2 | Fluke 77/BN Multimeter |
| 1 | JRG Variable Resistor Box |
| 1 | Soar Corp. Mini Resistance Box |
| 1 | Powertec D.C. Power Supply, Model 6C3000 |
| 2 | Hewlett-Packard 6236B Triple Output Power Supply |
| 1 | Hewlett-Packard E3611A D.C. Power Supply |
| 1 | ILX Lightwave LDC-3722 Laser Diode Controller |
| 1 | Spectra Diode Labs SDL800 Laser Diode Driver |
| 3 | Newport Digital Power Meter, Model 815 Series |
| 1 | Coherent Fieldmaster Power Meter, Model FM |
| 1 | Coherent 1000:1 Attenuator |
| 1 | Cole-Parmer Fiberglass, miniconnector J-Type Thermocouple |
| 1 | Cole-Parmer Metal, miniconnector J-Type Thermocouple |
| 3 | Miniconnector J-Type Thermocouple |
| 1 | 36" Diameter, 1/4" Steel Plate Carousel (Fabricated) |
| 6 | Aluminum TO-5 Package Mounts (Fabricated) |

- 1 Sybron/Thermolyne Type 1000 Stir Plate, Model SP-A1025B
- 1 Thermolyne Type 1900 Hot Plate, Model HP-A1915B
- 1 Thermolyne Type 2300, Model HP-2305B
- 2 Cole-Parmer Stirrer/Hotplate, Model 4658
- 1 Cenco PL60 Stirrer/Heater, Catalog 16632
- 1 Corning Remote Stirrer/Hotplate, Model PC-325
- 1 Olympus B071 Optical Microscope
- 1 Olympus 0.01mm standard, M-0550
- 1 Canon AE-1 Programmable Camera, 4852310

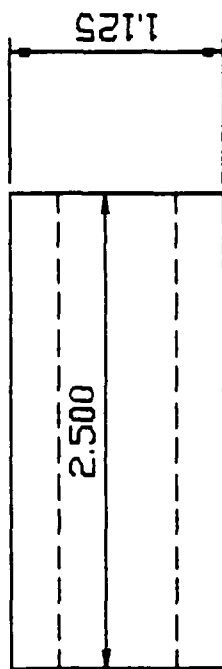
This list includes the hardware used only during the HF acid rinse tests:

- 1 Phir Laser Power Monitor, Model PD2-A
- 1 EG&G Princeton Applied Research Boxcar Averager, Model 162
- 1 SRS Power Supply and Display Module: Comp. Int. SR245
- 1 SRS Fast Sampler SR225
- 1 SRS Analog Processor SR235
- 1 SRS Gatd Integrator and Boxcar Averager
- 1 Fluke 8506A Thermal RMS Digital Multimeter
- 1 Micro Custom Built Computer System
 - IOTech IEEE 488 Board
 - Metrobyte DAS20 I/O Board
- 1 Tektronix/Sony 390AD Digitizer
- 1 Tektronix 7104 and DCS01 Oscilloscope Camera System
- 1 Avtech AVO-7A-C Pulse Generator
- 1 Sony SLD 202 Photocell
- 1 Watlow 945 Temperature Controller

- 1 **Spex Minimate Spectrometer**
- 1 **Gamma-Scientific Photometer**
- 1 **Melles Griot and Newport Fiber Positioner**
- 1 **Opto-Electronic Laser Diode Driver**
- 1 **SDL 922 Quasi-Continuous Wave Laser Driver**
- 1 **Opto-Electronic PD-15 Photodetector**
- 1 **Kyocer Fiber-pigtailed OEIC Package**

Appendix 5: Optical Microscope Adapters Design Diagram

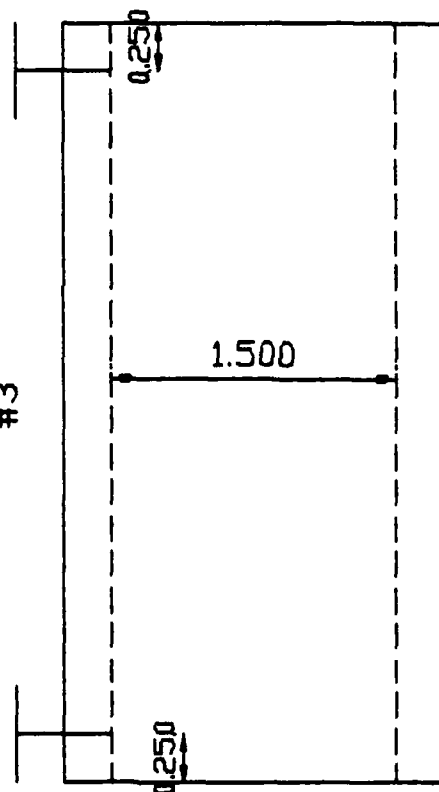
#1



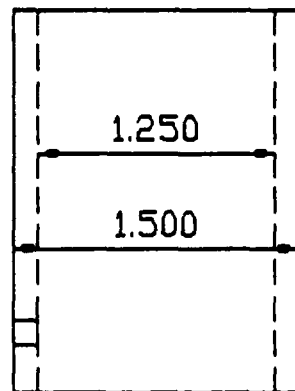
set screw/holes 3X

set screw/holes 3X

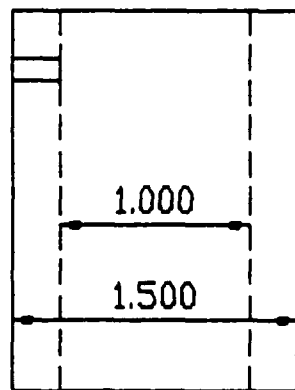
#3



#2



#4



1. All components are cylindrical tubes.
2. Dimensions not specified are flexible.
3. All tubes should have a flat black enamel coating.
4. Tubes #2 and #4 are inserts to tube #3.

School of Engineering	
Air Force Institute of Technology	
Wright Patterson AFB OH	
DR. BY:	David Leicester, 1Lt.
COURSE:	Thesis
DATE:	27 July 93
SCALE:	1:1

Appendix 6: Cleaving Technique

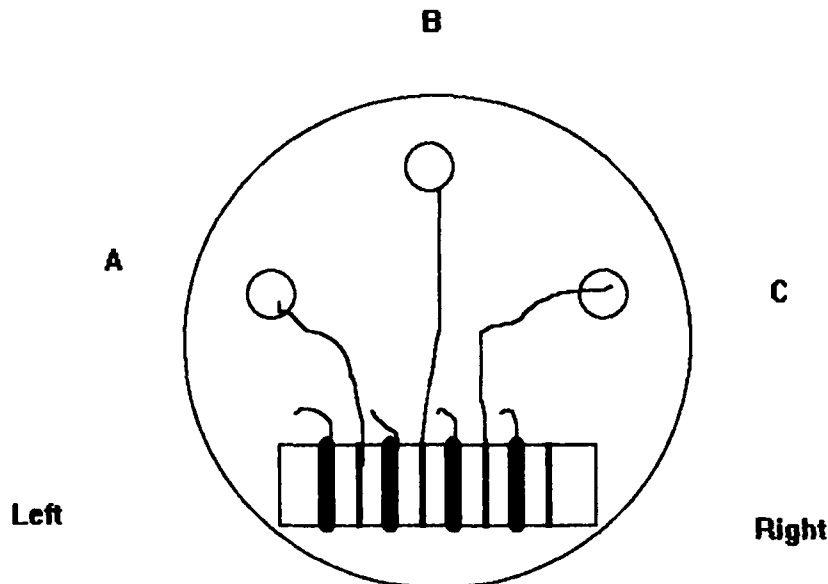
This provides a step-by-step checklist for the technique developed to obtain high-yield, uniform laser bars.

1. Power up the Loomis scribe.
2. Open pressure lines and set vacuum to $\sim 5\text{kPa}$.
3. Set skip index adjustment to $400.0\mu\text{m}$.
4. Lay down wafer and align masking pattern perpendicular to scribe's motion direction.
 - 4a. Using sighting eyepiece, align reticule marks on one end of masking pattern.
 - 4b. With "step" function off, engage "index" function and observe wafer traveling under field of view.
 - 4c. Repeat 4a and 4b until pattern is aligned on both ends to reticule.
5. Turn on the "step" function
6. Beginning at one end of wafer, scribe along the edge of the wafer chip at the desired crystal orientation and spatial period.
 - 6a. With a finger holding down lever arm to scribe, thus suspending the scribe, engage vacuum drive to scribe.
 - 6b. Manually, gently lower scribe to wafer 1-2mm from edge of wafer.
 - 6c. Enact scribe drive to drag scribe off edge of wafer.
 - 6d. Disengage vacuum drive to scribe.
 - 6e. Resulting scribe mark should be deep enough to observe penetration of gold alloy contacts. If not, adjust elevation of scribe and repeat step 6.
7. Press the "index" button and hold until scribe mount completes $400\mu\text{m}$ step.

8. Repeat steps 6 and 7 until one edge of wafer has been completely scribed.
9. Mount wafer chip to a soft pliable metal strip with Apiezon W-wax ("Black Wax").
 - 9a. Heat portion of metal strip to $\sim 100^{\circ}\text{C}$ keeping wax in contact with heated portion.
 - 9b. When enough wax has been deposited on metal to form a complete layer between the chip and metal, remove assembly from hotplate.
 - 9c. Spread wax to a thin uniform layer on metal.
 - 9d. Place wafer on wax film with scribe marks parallel to the axis of flexing that the metal strip will be submitted to. Minimum repositioning is desired.
 - 9e. Move on to step 10 after the wax has resolidified. (5 minutes)
10. Gently flex the assembly parallel to the scribe marks. The cleaves can be observed by the reflection pattern of the wafer chip. Stop flexing when the reflection pattern can be observed.
11. Dismount and clean the laser bars.
 - 11a. Submit metal, wax, and wafer to three separate rinses in trichloroethylene, TCE, keeping all laser bars in a single container.
 - 11b. Rinse the laser bars, and metal separately for cleaning purposes, in methanol.
 - 11c. Rinse the lasers bars in deionized water.
12. Carefully remove laser bars from deionized water and allow to dry on lens paper.
13. Store laser bars in safe wafer container for future use.

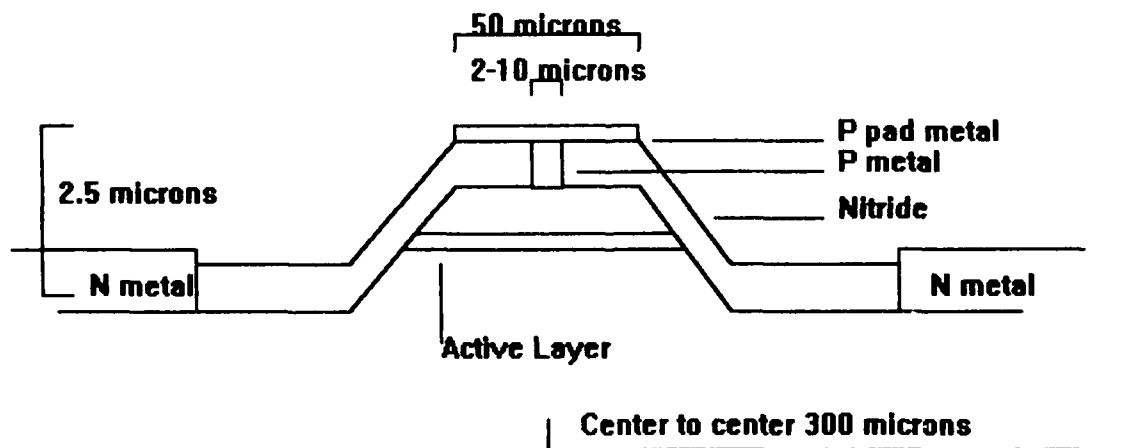
Appendix 7: TO-5 Package Mount/Device Material Profiles

This appendix describes how each device was packaged and the material composition profile for the 599, 600, and 706 laser technologies.



Typical package (599 or 600) with 3 lasers mounted. Thin strips are p-contacts and thick strips are n-contacts.(Not to Scale)

Material Profile for 599 and 600 wafers:



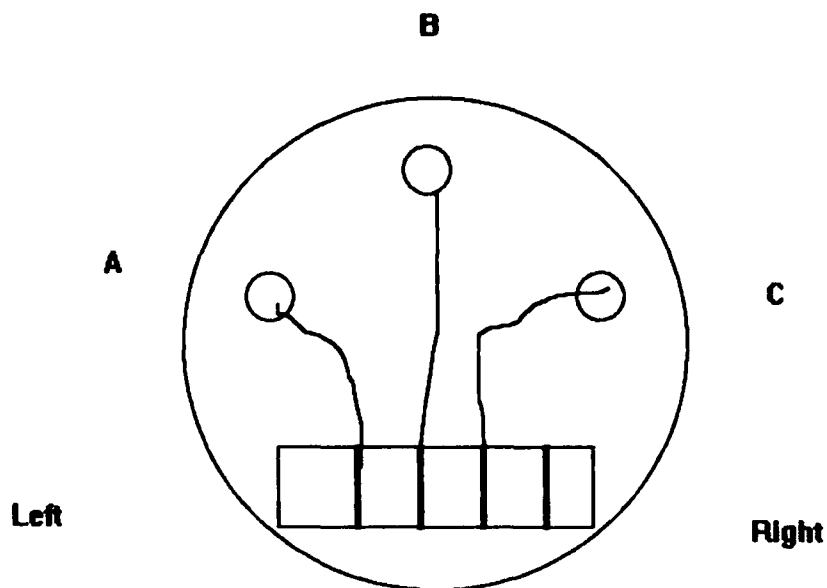
Typical profile for a single 599 or 600 device. Composition detailed below.
The 599 design aligns the contacts parallel to the (100) plane. The 600 design incorporates a 6° offset from the (100) plane toward the (001) plane.

599/600 Device Composition

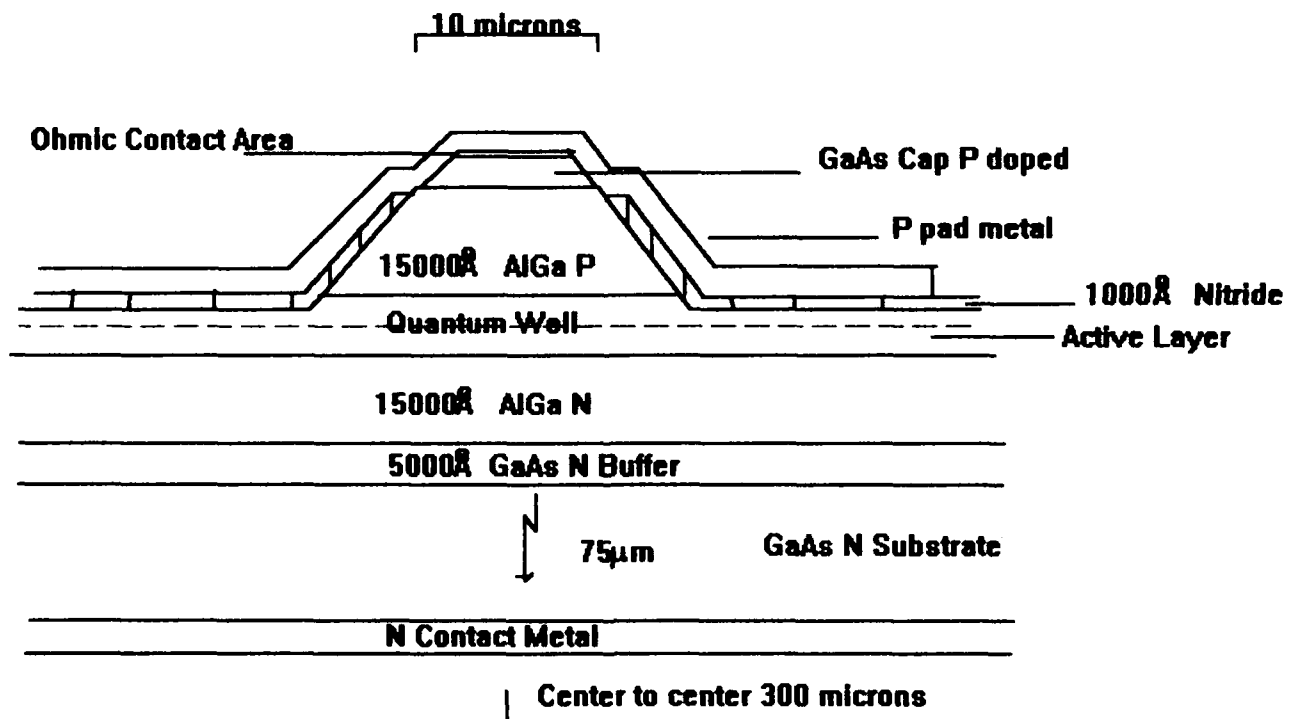
Material	Thickness	Doping Level	X
N-type Substrate		1×10^{18} (Si)	
GaAs	500Å	1×10^{18} (Si)	
$\text{Al}_x\text{GaAs:Si}$	1µm	5×10^{17}	40%
Al_xGaAs	2000Å		20%
ACTIVE LAYER			
GaAs	60Å		
In_xGaAs	50Å		20%
GaAs	60Å		
Al_xGaAs	2000Å		20%
$\text{Al}_x\text{GaAs:Be}$	1µm	1×10^{18}	40%
GaAs:Be	500Å	$>4 \times 10^{18}$	

Electrodes:

N ohmic	Thickness (Å)	P ohmic	Thickness (Å)
GaAs		GaAs	
Ni	70	Au	100
Ge	130	Zn	300
Ni	70	Au	2000
Au	300		
Ni	150		
Au	2000		
Pad	Metal		
Ti	300		
Au	2000		



Typical 706 package with 3 lasers mounted. Strips are p-contacts.
(Not to Scale)



Typical profile for a single 706 device. Composition detailed below.

706 Device Composition:

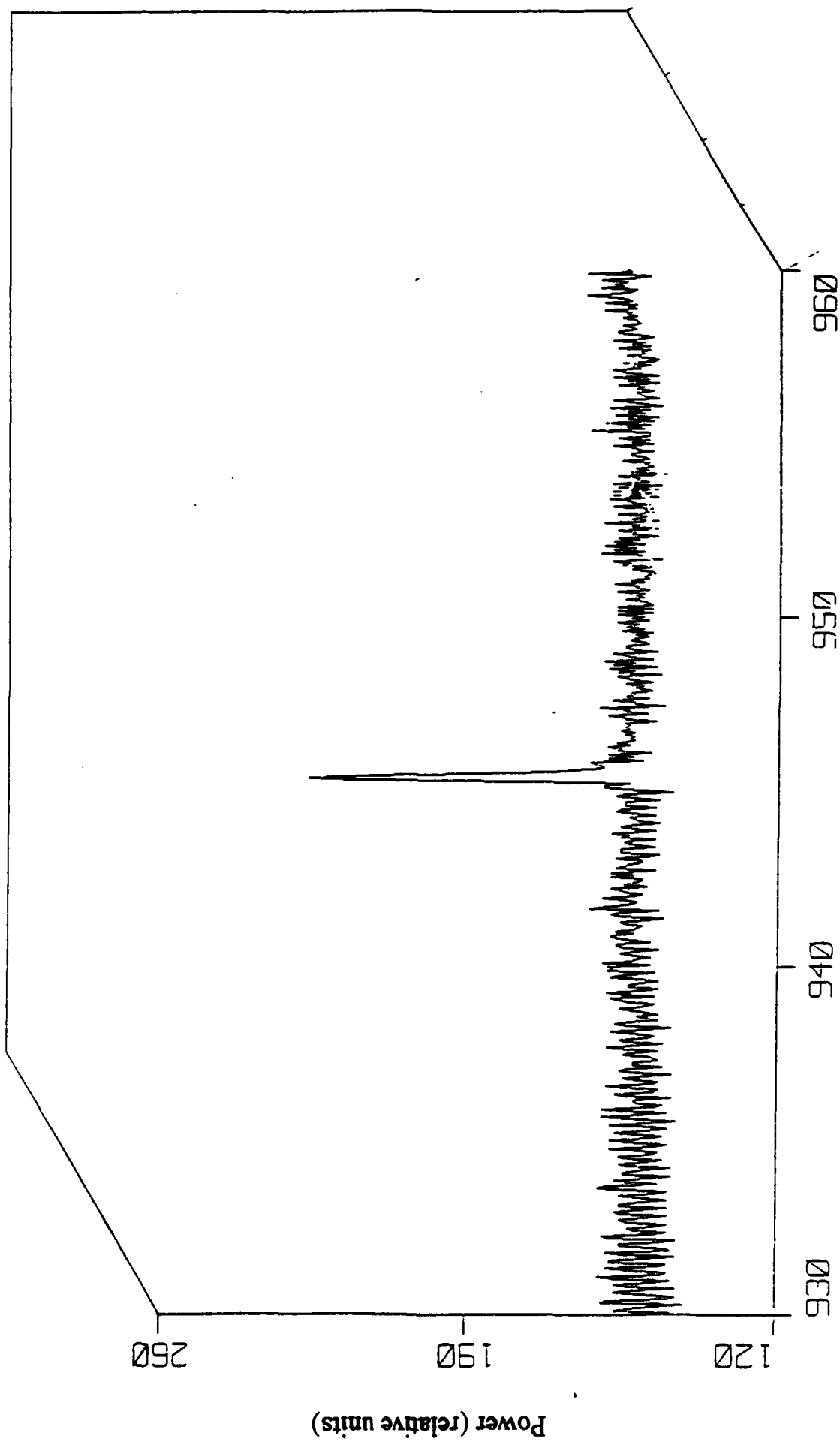
Material	Thickness	Doping Level	X
N-type Substrate	75mil	1×10^{18} (Si)	
GaAs	5000Å	1×10^{18} (Si)	
Al _x GaAs:Si	15000Å	5×10^{17}	60%
Al _x GaAs	1500Å		20%
ACTIVE LAYER			
GaAs	100Å		
In _x GaAs	60Å		20%
GaAs	100Å		
Al _x GaAs	1500Å		20%
Al _x GaAs:Be	15000Å	1×10^{18}	60%
GaAs:Be	1000Å	$>2 \times 10^{19}$	

Electrodes:

N ohmic	Thickness (Å)	P ohmic	Thickness (Å)
GaAs		GaAs	
Ni	70	Ti	300
Ge	130	Pt	300
Ni	70	Au	3000
Au	300		
Ni	150		
Au	2000		
Pad	Metal		
Ti	300		
Au	2000		

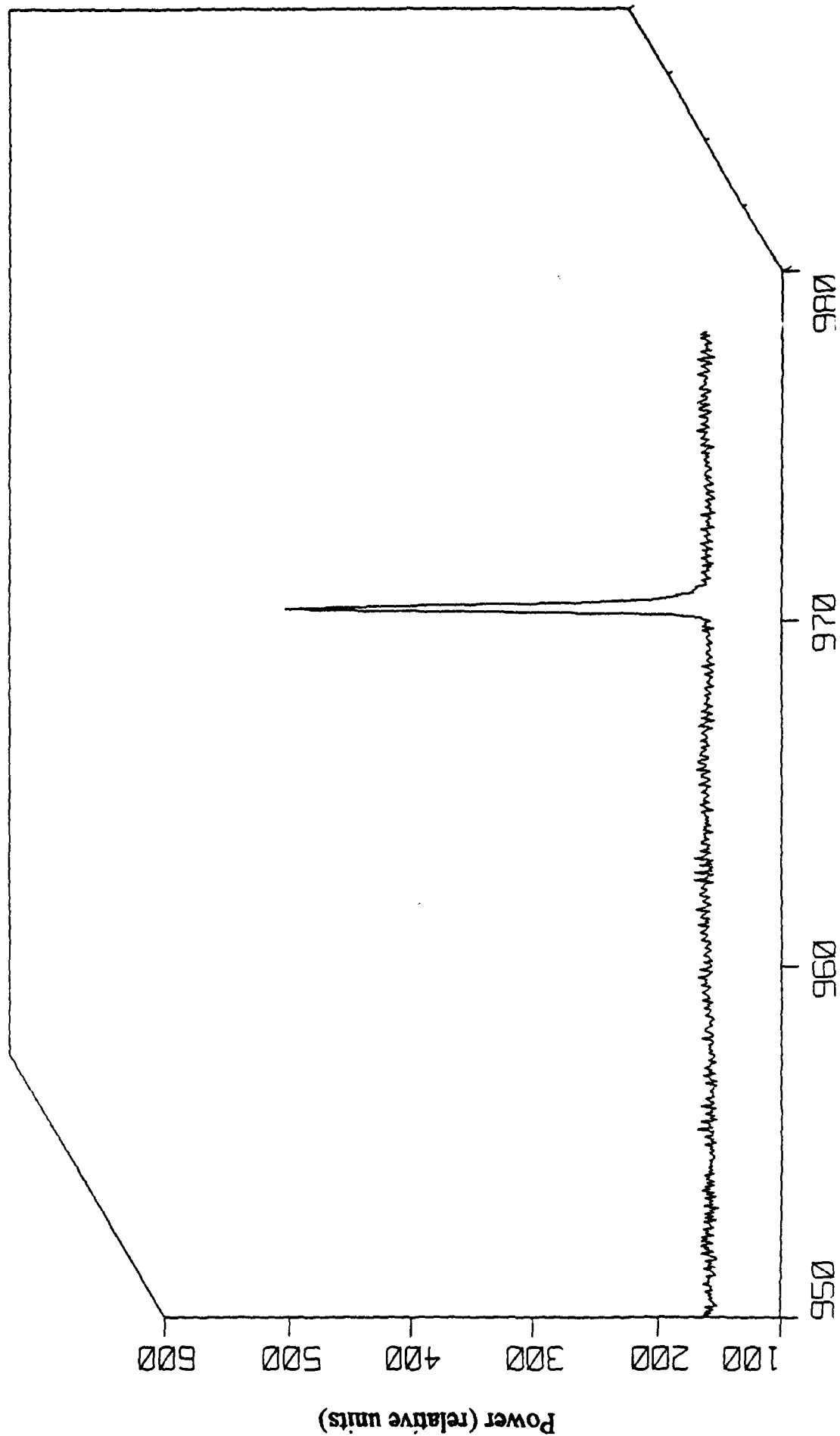
Appendix 8: Spectral Distribution Graphs

Laser 10B at 61mA



Wavelength (μm), Peak at 945μm

Laser 10B at 180mA



Wavelength (μm), Peak at 970μm

Appendix 9: Initial Rough Characterization of High Temperature Performance

Appendix 9

This data involves initial laser operation studies conducted at 100 C. (HTMP100.MCD)

Data approximations have been incorporated into this data.

Calculations conducted on Matchcad V.3.1 computer software.

1. All FND-100 voltages have been linearly interpolated to the initial target powers.

	time (min)	current (mA)	temp. (C)	power (mW)		time (min)	current (mA)	temp. (C)	power (mW)
R34B :=	0	89.6	94.0	4.5	O38A :=	0	86.0	105	4.6
	15	92.0	96.0	4.9		17	86.5	105.9	4.9
	30	92.2	96.8	4.6		52	86.7	100	6.5
	60	92.2	96.2	5.1		79	86.8	97.8	6.76
	92	93.0	94.7	5.7		114	88.0	99.5	6.6
	128	93.0	95.5	5.2		150	88.9	99.8	6.6
	158	93.1	94.6	4.9		160	89.9	100.2	6.7
	199	94.3	95.0	4.7		172	91.7	101.5	6.6
	215	97.1	95.2	4.5		896	91.9	94.7	4.5
	245	97.1	94.9	4.6		900	98.2	95.0	6.6
	279	101.7	95.8	4.5		937	108	100.1	6.6
	1005	101.64	91.5	0.24		983	112.3	99.8	6.8
G37C :=	0	109	95.0	10.1	O38B :=	0	154.5	100.9	3.3
	40	107	96.0	10.1		25	159	105.7	0.3
	65	116	95.5	10.1					
	100	119	95.8	8.1					

Temperature scaling factors obtained from thermocouple calibration.

$$r := 1.053$$

$$g := 1.058$$

$$o := 1.000$$

$$ir := 0..11$$

$$ig := 0..3$$

$$ioa := 0..14$$

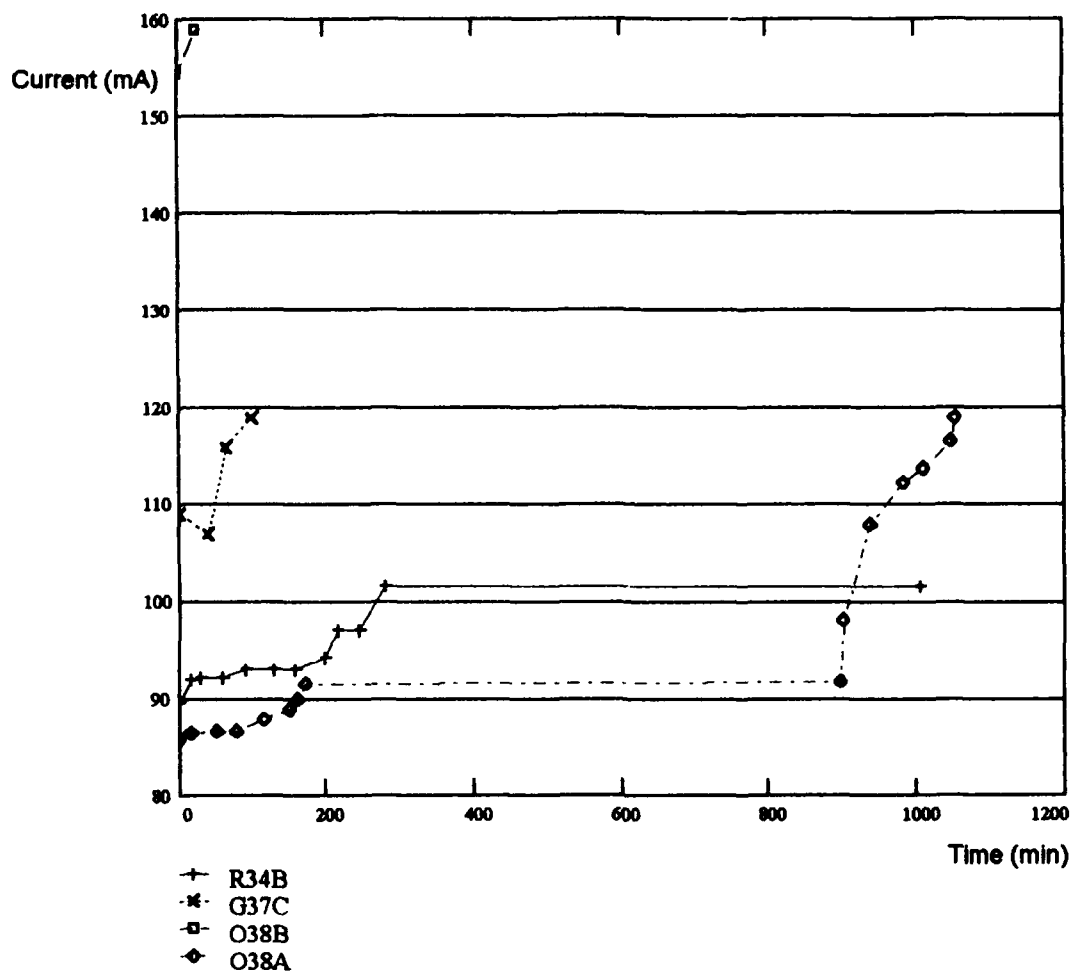
$$iob := 0..1$$

$$R34B_{r,2} := r \cdot R34B_{r,2}$$

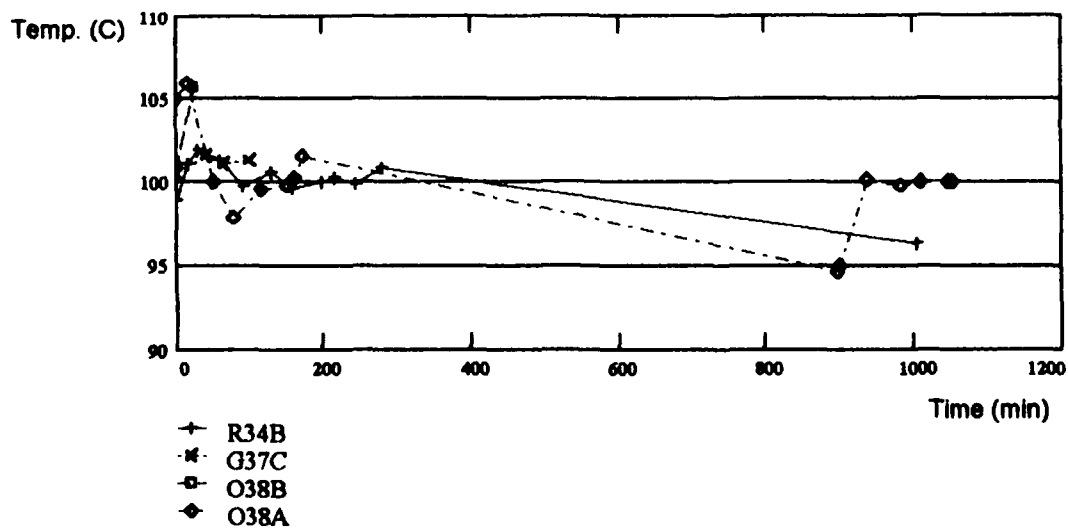
$$G37C_{g,2} := g \cdot G37C_{g,2}$$

R34B =	0	89.6	98.982	4.5	G37C =	0	109	100.51	10.1
	15	92	101.088	4.9		40	107	101.568	10.1
	30	92.2	101.93	4.6		65	116	101.039	10.1
	60	92.2	101.299	5.1		100	119	101.356	8.1
	92	93	99.719	5.7					
	128	93	100.562	5.2					
	158	93.1	99.614	4.9					
	199	94.3	100.035	4.7					
	215	97.1	100.246	4.5					
	245	97.1	99.93	4.6					
	279	101.7	100.877	4.5					
	1.005 · 10 ³	101.64	96.349	0.24					

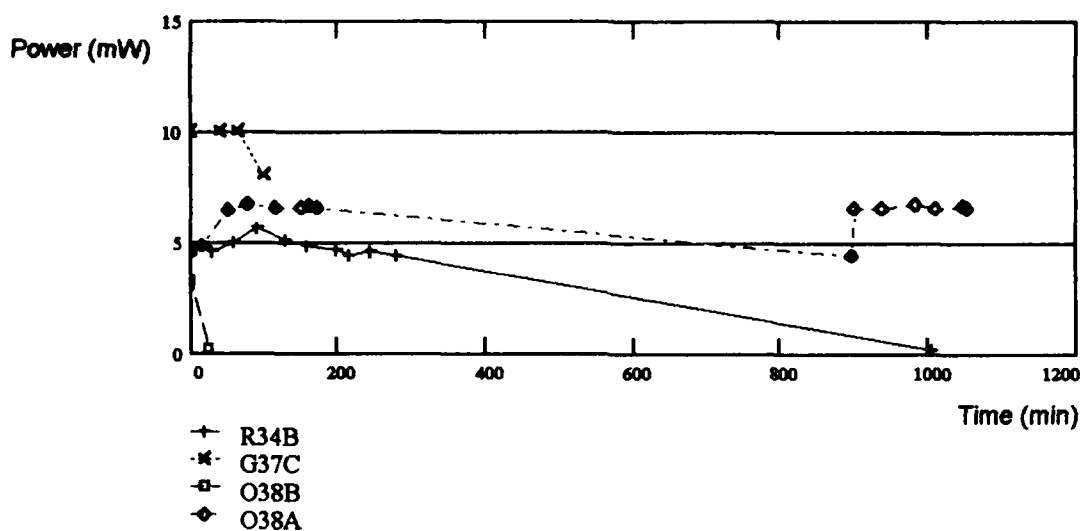
Current (mA) vs. Time (min):



Temperature (C) against Time (min):



Power (mW) against Time (min):



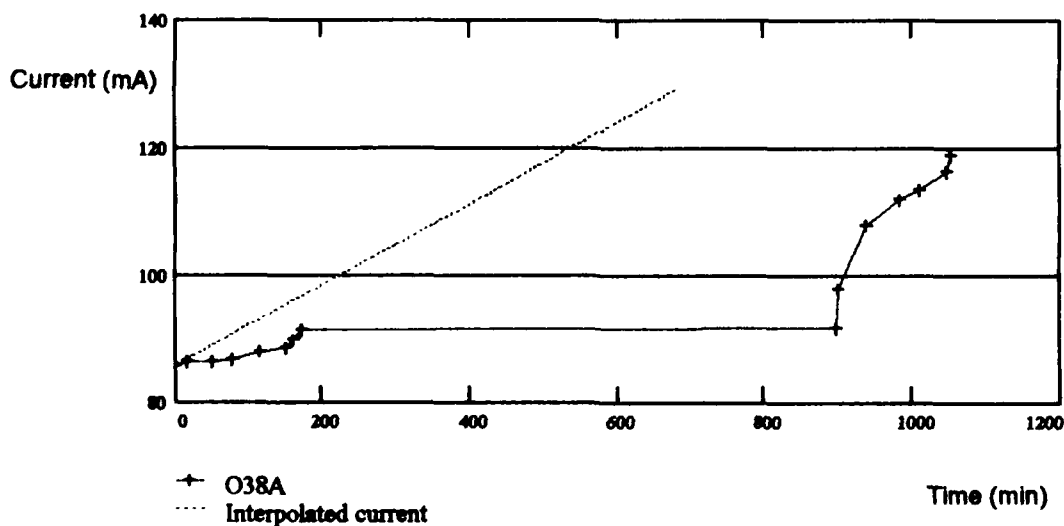
A crude estimate of the lifetime of laser O38A can be calculated from the slope of both regions analyzed at a constant power output and producing a line with this slope beginning at time zero and passing through 150% of the initial current measured.

$io1 := 0..7$	$io2 := 9..14$	
$t1_{io1} := O38A_{io1,0}$	$t2_{io2-9} := O38A_{io2,0}$	Initial current:
$c1_{io1} := O38A_{io1,1}$	$c2_{io2-9} := O38A_{io2,1}$	$O38A_{0,1} = 86$
$slp1 := \text{slope}(t1, c1)$	$slp2 := \text{slope}(t2, c2)$	$I_o := O38A_{0,1}$
$slp1 = 0.027$	$slp2 = 0.118$	

Weighting each slope by the number of data points as fraction of the total number data points:

$slp := \frac{9}{15} \cdot slp1 + \frac{6}{15} \cdot slp2$	$slp = 0.064$	$I_{fail} := 1.5 \cdot I_o$	$I_{fail} = 129$
$I(t) := slp \cdot t + I_o$	$tm := 0..680$	$I(680) = 129.281$	

Interpolated O38A Current against Time:



Appendix 10: Room Temperature Characterization of Laser 66B

Appendix 10: Room Temperature Characterization of Laser 66B

Laser 66B

$$\text{IR66B} := \begin{pmatrix} 32 & 52 & 58 & 60 & 62 & 64 & 67 & 69 & 73 & 76 & 79 & 82 \\ 0.30 & 0.80 & 1.9 & 3.0 & 4.1 & 5.3 & 6.4 & 7.2 & 8.1 & 9.1 & 10.3 & 11.4 \end{pmatrix} \quad \text{lsr} := \text{IR66B}$$

Calculations generated on Matchcad V. 3.1 computer software (24), [APP10.MCD].

Manipulation to generate the laser's linear domain:

$$\begin{aligned} r1 &:= 0..11 \quad d := 0 \quad b := 0 \quad k := 0..9 \quad d_k := \text{lsr}_{0,k+2} \quad b_k := \text{lsr}_{1,k+2} \\ \text{slp} &:= \text{slope}(d, b) \quad I_0 := \text{intercept}(b, d) \quad I_0 = 51.545 \\ \text{rlin}(x) &:= \text{slp} \cdot (x - I_0) \quad \text{slp} = 0.377 \\ \text{err}_k &:= b_k - \text{rlin}(d_k) \quad \text{stdev}(\text{err}) = 0.367 \quad \text{sl} := \frac{\text{stdev}(\text{err})}{\text{slp}} \quad \text{sl} = 0.974 \\ \text{PIR66B}(x) &:= \text{rlin}(x) \quad \text{IIR66B} := \text{ceil}(I_0) .. \text{lsr}_{0,11} \end{aligned}$$

Compute intercept, slope, and their uncertainties using Philip R. Bevington's technique:

Plot current (X) vs. power (Y) to get I_0 .

$$i := 0..9 \quad X_i := \text{lsr}_{1,i+2} \quad Y_i := \text{lsr}_{0,i+2}$$

$$N := \text{length}(Y) \quad N = 10$$

$$\Delta := N \cdot \sum_i (X_i)^2 - \left(\sum_i X_i \right)^2 \quad \Delta = 885.56$$

$$A := \frac{1}{\Delta} \left[\sum_i (X_i)^2 \cdot \sum_i Y_i - \sum_i X_i \cdot \sum_i X_i \cdot Y_i \right] \quad A = 51.545 \quad \text{Y-intercept, threshold current } (I_0)$$

$$B := \frac{1}{\Delta} \left[N \cdot \sum_i X_i \cdot Y_i - \left(\sum_i X_i \right) \cdot \left(\sum_i Y_i \right) \right] \quad B = 2.613 \quad \text{Slope}$$

$$\sigma := \sqrt{\frac{1}{N-2} \cdot \sum_i (Y_i - A - B \cdot X_i)^2} \quad \sigma = 1.081$$

$$\sigma_A := \sqrt{\frac{\sigma^2}{\Delta} \cdot \sum_i (X_i)^2} \quad \sigma_A = 0.84 \quad \text{Uncertainty in Intercept}$$

$$\sigma_B := \sqrt{\frac{N \cdot \sigma^2}{\Delta}} \quad \sigma_B = 0.115 \quad \text{Uncertainty in slope}$$

$$r := \frac{N \cdot \sum_i X_i \cdot Y_i - \left(\sum_i X_i \right) \cdot \left(\sum_i Y_i \right)}{\sqrt{N \cdot \sum_i (X_i)^2 - \left(\sum_i X_i \right)^2} \cdot \sqrt{N \cdot \sum_i (Y_i)^2 - \left(\sum_i Y_i \right)^2}} \quad r = 0.992 \quad \text{Correlation Coefficient}$$

Threshold Current I_0 is: $A = 51.545$ with an uncertainty +/- of: $\sigma_A = 0.84$ $\frac{\sigma_A}{A} = 1.62\%$

Invert XY plot to get power (X) vs. current (I)

$i := 0..9$ $X_i := I_{X0,i+2}$ $Y_i := I_{X1,i+2}$

$$N := \text{length}(Y)$$

$$N = 10$$

$$\Delta := N \cdot \sum_i (X_i)^2 - \left(\sum_i X_i \right)^2$$

$$\Delta = 6.14 \cdot 10^3$$

$$A := \frac{1}{\Delta} \left[\sum_i (X_i)^2 \cdot \sum_i Y_i - \sum_i X_i \cdot \sum_i X_i \cdot Y_i \right]$$

$$A = -19.324 \quad \text{Y-intercept}$$

$$B := \frac{1}{\Delta} \left[N \cdot \sum_i X_i \cdot Y_i - \left(\sum_i X_i \right) \cdot \sum_i Y_i \right]$$

$$B = 0.377$$

Slope

X-intercept for $Y=0$ (I_0): $-\frac{A}{B} = 51.275$

$$\sigma := \sqrt{\frac{1}{N-2} \cdot \sum_i (Y_i - A - B \cdot X_i)^2}$$

$$\sigma = 0.41$$

$$\sigma_A := \sqrt{\frac{\sigma^2}{\Delta} \cdot \sum_i (X_i)^2}$$

$$\sigma_A = 1.15$$

Uncertainty in Intercept

$$\sigma_B := \sqrt{\frac{N \cdot \sigma^2}{\Delta}}$$

$$\sigma_B = 0.017$$

Uncertainty in Slope

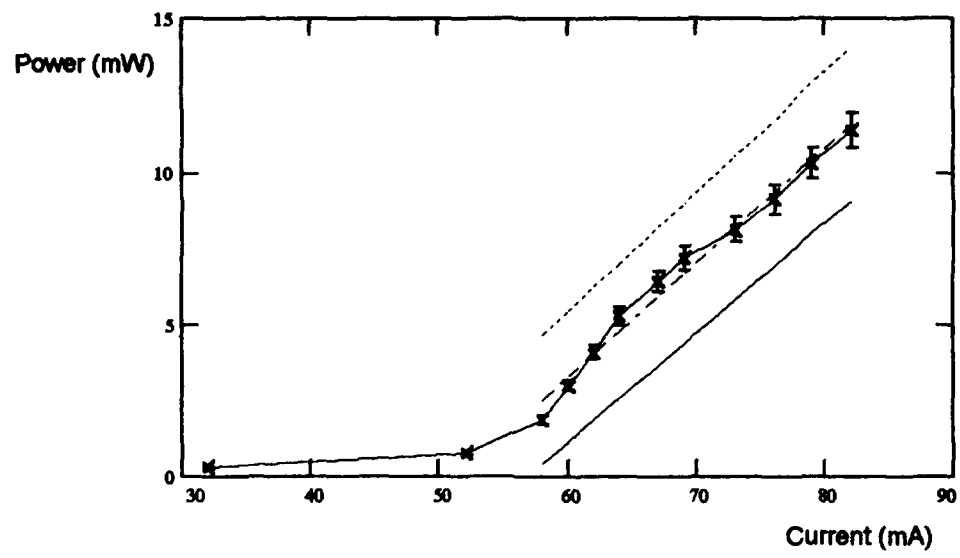
$$r := \frac{N \cdot \sum_i X_i \cdot Y_i - \left(\sum_i X_i \right) \cdot \sum_i Y_i}{\sqrt{N \cdot \sum_i (X_i)^2 - \left(\sum_i X_i \right)^2} \cdot \sqrt{N \cdot \sum_i (Y_i)^2 - \left(\sum_i Y_i \right)^2}}$$

$$r = 0.992$$

Correlation Coefficient

Slope Efficiency is: $B = 0.377$ with an uncertainty +/- of: $\sigma_B = 0.017$ $\frac{\sigma_B}{B} = 4.395\%$

Laser 66B Output Power (mW) vs. Pump Current (mA)
(Initial Room Temperature Characterization)



Appendix 11: Current Required During Aging for Laser 54C

Appendix 11: Current Demanded Over Time to Maintain Constant Power Output

Calculations generated on Matchcad V. 3.1 computer software (24), [APP11.MCD].

$$R54C5 := \begin{pmatrix} 71.9 & 71.2 & 70.9 & 71.1 & 71.7 & 71.8 & 72.4 & 73.0 & 73.2 & 73.8 & 74.0 \\ 2100 & 2117 & 2149 & 2220 & 2251 & 2319 & 2350 & 2421 & 2447 & 2525 & 2549 \end{pmatrix}$$

$$R54C5a := \begin{pmatrix} 74.2 & 74.7 & 75.0 & 75.3 & 75.4 & 76.2 & 76.4 & 76.3 & 76.4 & 77.4 & 77.5 \\ 2617 & 2651 & 2718 & 2750 & 2822 & 2851 & 2921 & 2950 & 3020 & 3049 & 3118 \end{pmatrix}$$

$$b := 0..10 \quad R54C5_{0,b+11} := R54C5a_{0,b} \quad R54C5_{1,b+11} := R54C5a_{1,b}$$

$$b5 := 0..21 \quad cR54C5_{0,b5} := \frac{R54C5_{0,b5}}{70.9}$$

$$tR54C5 := (0 \ 17 \ 49 \ 80 \ 111 \ 139 \ 170 \ 201 \ 227 \ 265 \ 289)$$

$$tR54C5a := (317 \ 351 \ 378 \ 410 \ 442 \ 471 \ 501 \ 530 \ 560 \ 589 \ 618) \quad tR54C5_{0,b+11} := tR54C5a_{0,b}$$

$$l5 := 0..21 \quad t := 0 \quad c := 0$$

$$t_{l5} := tR54C5_{0,l5} \quad c_{l5} := cR54C5_{0,l5}$$

$$slp := \text{slope}(t, c)$$

$$slp = 0.00015$$

$$C_0 := \text{intercept}(t, c)$$

$$C_0 = 0.998$$

$$rlin5(x) := slp \cdot x + C_0$$

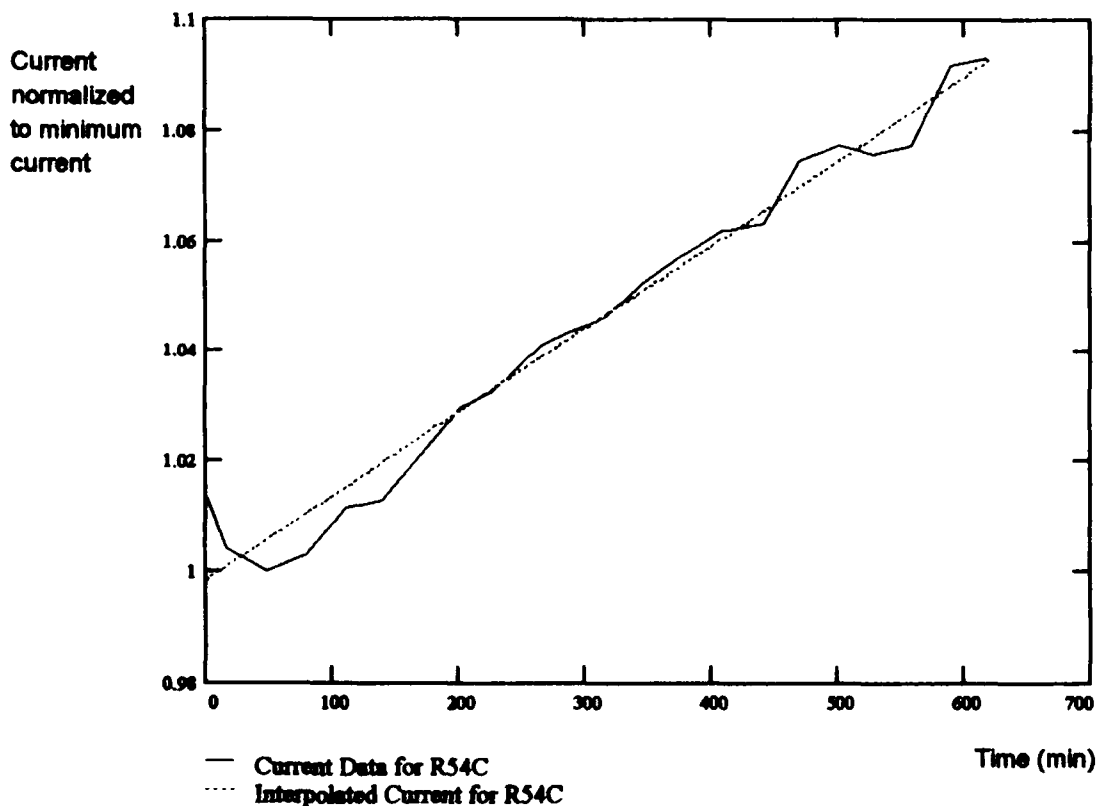
$$T5 := 0..620$$

$$rlin5(3300) = 1.501$$

$$err := c - rlin5(t) \quad \text{stdev}(err) = 0.005$$

$$st := \frac{\text{stdev}(err)}{slp}$$

$$st = 32.324$$



Appendix 12: Laser Characterization Summary Chart

Glossary:

- Laser** - Numerical identification label of lasing circuit
- Pwr** - Constant optical power output device held at during elevated thermal exposure
(NL - not lasing, this is for those devices that could only luminesce or were used
as control devices.) (mW)
- time elev.** - Duration of elevated thermal exposure (min)
- IR Ith** - Threshold current for initial room temperature characterization (mA)
- %IRth** - Absolute error of initial room temperature threshold current
- IR slp** - Slope efficiency for initial room temperature characterization (W/A)
- %IRsl** - Absolute error of initial room temperature slope efficiency
- FR Ith** - Threshold current for final room temperature characterization (mA)
- %FRth** - Absolute error of final room temperature threshold current
- FR slp** - Slope efficiency for final room temperature characterization (W/A)
- %FRsl** - Absolute error of final room temperature slope efficiency
- Mnt** - Mount, the thermal platform identification
- IE Ith** - Threshold current for initial elevated temperature (100°C) characterization (mA)
- %IEth** - Absolute error of initial elevated temperature threshold current
- IE slp** - Slope efficiency for initial elevated temperature characterization (W/A)
- %IEsl** - Absolute error of initial elevated temperature slope efficiency
- FE Ith** - Threshold current for final elevated temperature characterization (mA)
- %FEth** - Absolute error of final elevated temperature threshold current

Glossary (continued):

FE slp - Slope efficiency for final elevated temperature characterization (W/A)

%FEsl - Absolute error of final elevated temperature slope efficiency

E lifet - Estimated lifetime (min) (C - calculated, F - device actually failed after this duration) (min)

Cavity L - Cavity length of each device (μm)

Cavity W - Cavity width of each device (μm)

Time at elevated temperature is typically (but not always) the time elapsed between elevated characterizations.

Occasionally wavelength calibrations were incorrect but these measurements have been highlighted and generally induced at most a 2% error in power measurements.

Laser BATCH	Pwr ONE	IR Ith	%IRth Rλ =	IR slp 970n m	%IRsl	FR Ith	%FRth	FR slp	%FRsl	Mnt
40A	NL	36.3	5.35	0.372	11.5	40.0	0.323	0.432	0.721	B
41A	NL	89.8	6.88	0.075	14.9	LUM				P
41B	5	37.7	2.92	0.173	4.21	44.6	3.05	0.125	2.81	P
42A	5	43.6	1.84	0.220	3.22	35.0	5.85	0.178	6.61	G
42B	NL	41.6	1.63	0.276	3.35	33.1	6.36	0.166	5.62	G
43A	5	31.9	1.76	0.264	2.41	45.9	0.467	0.315	0.918	R
43B	NL	38.5	1.09	0.289	2.02	36.7	1.51	0.272	1.77	R
BATCH	TWO		Rλ =	960n						
44A	NL	54.9	4.72	0.274	9.18	62.1	2.87	0.317	8.77	R
44B	10	49.2	1.17	0.219	2.16	58.9	1.80	0.312	3.95	R
45A	NL	63.1	4.10	0.236	7.83	73.8	1.03	0.266	2.98	B
45B	NL	56.5	3.58	0.182	5.42	78.9	1.23	0.372	4.28	B
46B	10	53.2	0.702	0.381	1.83	59.7	0.486	0.422	1.23	P
46C	NL	54.1	0.404	0.339	1.04	69.8	1.07	0.303	2.62	P
47C	NL	33.9	6.75	0.180	5.13	46.2	0.905	0.266	1.38	G
48B	NL	33.8	3.34	0.375	7.23	34.0	1.48	0.330	2.47	O
48C	10	27.7	4.20	0.223	3.81	33.3	1.51	0.270	1.83	O
BATCH	THREE		Rλ =	960n						
49A	7	32.1	1.67	0.310	2.83	44.5	0.392	0.471	1.20	R
49B	NL	41.2	2.75	0.353	5.97	42.0	2.03	0.383	4.16	R
50A	7	40.3	1.19	0.455	2.77	43.5	1.76	0.459	5.22	B
50B	NL	40.5	2.15	0.256	3.42	33.7	8.44	0.215	7.76	B
51A	7	48.4	1.39	0.319	3.17	69.6	0.720	0.315	2.40	P

Laser	IE lth	%IEth	IE slp	%IEsl	FE lth	%FEth	FE slp	%FEsl	E lifet	Cavity L ±7.1µm	Cavity W ±1µm
BATCH	ONE	Eλ = 1000nm									
40A										321.5	2.86
41A	LUM				LUM					400.1	5.72
41B	77.3	0.818	0.51	3.17	85.5	1.86	0.273	5.69	1170C	400.1	4.29
42A	82.7	0.962	0.666	6.11	99.4	2.96	0.089	12.7	140F	400.1	4.29
42B	79.9	0.136	0.674	0.947	80.2	0.545	0.646	2.85		400.1	4.29
43A	83.8	0.592	0.34	3.50	84.7	0.636	0.285	2.90	3000C	400.1	4.29
43B	70.5	1.05	0.252	4.47	68.6	0.854	0.244	2.41		400.1	4.29
BATCH	TWO	Eλ = 980nm									
44A	91.6	1.93	0.206	5.41	96.7	3.03	0.154	14.4		443.0	7.15
44B	87.1	0.505	0.327	1.74	LUM				64F	443.0	7.15
45A	LUM				LUM					414.4	5.72
45B	LUM				LUM					412 S	6.43 S
46B	91.0	0.948	0.389	4.32	LUM				41F	400.1	4.29
46C	LUM				LUM					400.1	4.29
47C	LUM				LUM					400.1	2.86
48B	69.4	0.366	0.439	1.50	69.1	0.602	0.448	2.05		400.1	4.29
48C	67.4	0.212	0.398	0.833	70.7	0.768	0.375	2.24	2000C	414.4	2.86
										420 S	3.66 S
BATCH	THREE	Eλ = 980nm									
49A	70.4	0.771	0.573	3.67	92.5	1.76	0.231	7.97	600F	411 S	3.57 S
49B	73.4	0.460	0.610	2.50	73.8	0.428	0.699	2.86		414.4(C)	4.3(C)
50A	77.6	0.619	0.788	3.96	86.9	0.722	0.359	3.08	1350C	400.1	4.29
50B	82.5	0.180	0.585	1.43	80.9	0.473	0.542	2.21		400.1(A)	4.29(A)
51A	123.6	1.14	0.254	5.53	137.8	0.585	0.264	4.79	1170C	400.1	4.29

Laer	Pwr	IR lth	%IRth	IR slp	%IRsl	FR lth	%FRth	FR slp	%FRsl	Mnt
51B	NL	44.8	1.69	0.219	2.49	41.8	3.41	0.207	4.58	P
52A	7	51.6	0.406	0.240	0.924	62.6	0.91	0.417	3.13	G
52B	NL	52.4	2.83	0.207	5.33	52.2	1.40	0.221	2.45	G
53A	NL	54.5	2.78	0.255	5.89	58.6	2.16	0.370	6.38	O
53C	7	42.7	0.769	0.296	1.24	46.3	2.43	0.315	5.07	O
BATCH	FOUR		Rλ =	960n						
				m						
54B	NL	40.1	1.82	0.229	3.89	55.2	0.434	0.320	1.04	R
54C	5	27.3	3.26	0.289	6.73	33.9	1.07	0.377	2.11	R
55A	5	26.9	8.16	0.235	8.03	37.9	1.04	0.436	2.30	B
55B	NL	44.3	3.74	0.264	5.77	39.8	4.05	0.255	5.56	B
56B	5	43.1	0.656	0.327	1.44	48.3	0.573	0.462	2.02	P
57A	NL	38.5	1.13	0.280	3.44	39.7	1.05	0.425	2.36	G
57B	5	37.9	4.22	0.231	5.18	42.6	4.11	0.255	6.95	G
58B	NL	47.4	0.395	0.520	2.53	51.3	0.143	0.521	0.527	O
BATCH	FIVE		Rλ =	960n						
				m						
59A	5	32.0	6.01	0.160	6.78	44.9	0.405	0.371	1.00	R
60A	7,10	33.4	5.06	0.218	5.10	38.1	2.79	0.248	3.61	B
60B	5	42.4	3.29	0.346	7.20	45.7	0.468	0.393	1.07	B
62A	NL	58.9	3.13	0.221	6.33	LUM				P
62B	5,7	42.7	1.98	0.312	4.12	46.0	1.23	0.447	3.21	P

Laser	IE lth	%IEth	IE slp	%IEsl	FE lth	%FEth	FE slp	%FEsl	E lifet	Cavity L ±7.1µm	Cavity W ±1µm
51B	73.9	0.395	0.418	1.83	73.4	0.730	0.426	3.26		400.1	4.29
52A	96.5	0.332	0.375	1.75	116.8	1.51	0.180	13.2	112F	400.1	8.58
52B	89.0	0.165	0.556	1.07	90.2	0.427	0.632	3.84		400.1	7.15
53A	89.6	0.802	0.312	3.77	91.1	1.06	0.305	4.76		414.4	5.72
53C	75.6	0.343	0.337	1.47	87.2	0.292	0.435	1.52	2050C	400.1	4.29
BATCH FOUR Eλ = 980nm											
54B	LUM				LUM					471.6	4.29
54C	64.1	0.234	0.572	0.985	67.9	0.489	0.515	2.425	3300C	471.6	2.86
										484 S	2.63 S
55A	72.8	0.455	0.544	2.40	76.1	0.919	0.409	3.31	2840C	471.6	4.29
55B	80.9	0.297	0.637	1.91	79.0	0.410	0.593	1.92		471.6	2.86
56B	76.0	0.189	0.423	0.938	86.1	0.694	0.299	2.88	1350C	400.1	2.86
57A	LUM				LUM					400.1	4.29
57B	75.7	0.444	0.583	2.19	85.8	0.530	0.310	1.92	1300C	400.1	4.29
58B	LUM				LUM					400.1	2.86
BATCH FIVE Eλ = 980nm											
59A	79.0	0.363	0.384	1.76	NL				151F	400.1	2.86
60A	64.3	0.955	0.240	2.00						414.4	4.29
	S63.4	1.32	0.207	2.81	74.2	1.73	0.186	4.33	1980C7		
60B	77.9	0.802	0.362	2.79	S97.9	1.88	0.120	6.72	304F	414.4	5.72
					105.5	0.676	0.106	3.40			
62A	LUM				LUM					400.1	2.86
62B	77.7	0.282	0.586	1.72	95.5	1.90	0.153	7.60	348F	400.1	4.29

Laser	Pwr	IR lth	%IRth	IR slp	%IRsl	FR lth	%FRth	FR slp	%FRsl	Mnt
63A	NL	39.5	2.91	0.281 980n	3.99	37.3	11.8	0.207 960nm	12.3	G
63B	5,7,10	49.4	3.54	0.324 m	6.74	49.7	0.444	0.342	0.873	G
64B	NL	40.2	3.85	0.345	7.62	50.7	0.313	0.368	0.738	O
64C	NL	52.1	1.00	0.356	2.68	62.2	0.957	0.300	2.52	O
BATCH	SIX		Rλ =	960n						
66A	NL	86.4	4.16	0.139 m	20.0	LUM				R
66B	NL	51.5	1.63	0.377 980n	4.40	64.8	1.44	0.291 960nm	4.02	R
70A	5,7	48.6	3.96	0.264 m	7.08	50.1	0.574	0.450	1.71	B
70B	NL	41.4	6.13	0.218	7.19	38.3	1.83	0.284	2.56	B
72A	NL	57.6	1.03	0.255	1.86	LUM				P
30B	5,7,10	56.6	0.659	0.350	1.71	49.0	0.907	0.311	1.79	G
30C	NL	31.7	6.03	0.266	5.73	26.4	1.72	0.219	1.36	G
31A	5	42.5	3.86	0.243	4.95	45.3	1.05	0.445	2.36	O
31B	7,10	46.9	1.59	0.243	2.72	48.9	0.243	0.406	0.580	O
33A	NL	42.2	0.208	0.485	0.492	48.0	0.517	0.458	1.27	P
Averages			2.86		4.96		1.89		3.02	

Laser	IE lth	%IEth	IE slp	%IEsl	FE lth	%FEth	FE slp	%FEsl	E lft	Cavity L	Cavity W ±1μm
63A	76.6	0.622	0.485	2.44	77.1	0.460	0.486	2.09		±7.1μm	
63B	82.0	0.278	0.662	1.69	107.1	0.383	0.176	1.65	536F	400.1	4.29
64B	LUM				LUM					400.1	2.86
64C	LUM				LUM					400.1	4.29
BATCH	SIX		Eλ =	980n						400.1	4.299
				m							
66A	LUM				LUM					371.5	7.15
66B	LUM				LUM					371.5	7.15
70A	79.8	0.770	0.414	3.88	103.8	2.12	0.136	6.65	432F	400.1	4.29
70B	81.7	0.906	0.302	3.21	85.6	0.487	0.335	2.78		400.1	2.86
72A	LUM				LUM					400.1	4.29
30B	78.7	0.495	0.613	2.81	85.2	0.626	0.503	2.82	3580C5	400.1	4.29
30C	69.7	0.228	0.585	0.997	69.4	0.444	0.562	1.83		400.1	2.86
31A	79.4	0.329	0.501	1.66	NL				73F	400.1	2.86
31B	76.3	0.534	0.593	2.92						400.1	2.86
	S77.0	0.767	0.523	3.60	94.1	1.84	0.167	7.22	278F		
33A	LUM				LUM					371.5	2.86
Averages		0.550		2.51		0.969		4.41			

Appendix 13: Lifetime Calculation as a Function of Power

Appendix 13: Lifetime Calculation as a Function of Power

This calculates the empirical relation for the lifetime of a laser as a function of output power.

Calculations generated on Matchcad V. 3.1 computer software (24), [LFTM.MCD].

41B 43A 54C 55A 56B 57B 63B 70A 30B

LF5 := (1170 3000 3300 2840 1350 1300 1140 669 3580)

SDV5 := (14.3 16.1 32.3 39.0 14.2 25.8 10.4 4.5 12.9)

i := 0..8 LF5_i := LF5_{0,i}

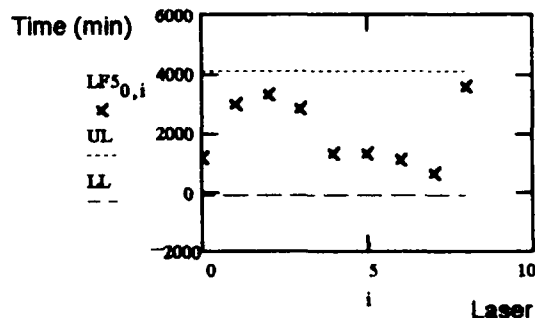
$$LF5_{av} := \frac{\sum LF5_{0,i}}{9} \quad LF5_{av} = 2.039 \cdot 10^3$$

err := LF5_{av} - LF5 stdev(err) = 1.054 · 10³ SDV5 := stdev(err)

UL := LF5_{av} + 2 · SDV5

LL := LF5_{av} - 2 · SDV5

Lifetimes for Lasers Operating at 5mW



i := 0..5

LF7 := $\begin{bmatrix} 600 \\ 1350 \\ 1170 \\ 2050 \\ 1980 \\ 512 \end{bmatrix}$ SDV7 := $\begin{bmatrix} 35.9 \\ 18.5 \\ 16.9 \\ 14.3 \\ 25.0 \\ 6.2 \end{bmatrix}$

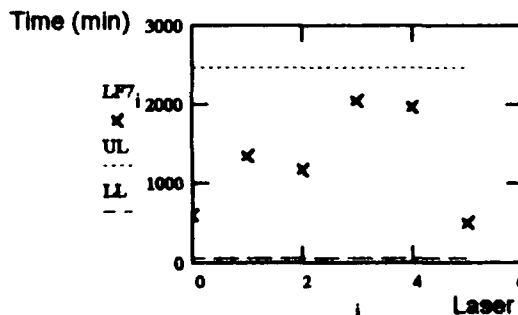
$$LF7_{av} := \frac{\sum LF7_i}{6} \quad LF7_{av} = 1.277 \cdot 10^3$$

err := LF7_{av} - LF7 SDV7 := stdev(err) stdev(err) = 598.898

UL := LF7_{av} + 2 · SDV7

LL := LF7_{av} - 2 · SDV7

Lifetimes for Lasers Operating at 7mW



$$y := \frac{\ln(LF5_{av})}{\ln(LF7_{av})}$$

$$x := \frac{\ln(5)}{\ln(7)}$$

slp := slope(x, y)

a := intercept(x, y)

slp = -1.39

a = 9.858

$$A := e^a$$

$$A = 1.911 \cdot 10^4$$

$$t(P) := A \cdot P^{slp}$$

$$LF5_{av} = 2.039 \cdot 10^3$$

$$LF7_{av} = 1.277 \cdot 10^3$$

$$t(5) = 2.039 \cdot 10^3$$

$$t(7) = 1.277 \cdot 10^3$$

Appendix 14: Variable List

Variables are listed in order of appearance.

I	current (mA)	U_c	built-in potential (V)
I_o	initial current (mA)	V_r	external bias (V)
T	temperature ($^{\circ}\text{C}$ or $^{\circ}\text{K}$)	EL	spontaneous emission intensity (mW/cm ²)
J	current density (A/cm ²)	EL_o	initial spontaneous emission intensity (mW/cm ²)
P	power (mW)	J_{th}	threshold current density
E_a	activation energy (eV)	J_{tho}	initial threshold current density
$k = 1.38062 \cdot 10^{-23} \text{ J/}^{\circ}\text{K}$	Boltzmann constant	η_d	external differential quantum efficiency
A_T, A_P, A_J, n	curve fitting constants	η_{do}	initial external differential quantum efficiency
$life$	operational lifetime (min.)	C	line fitting constant
t_d	generation time of first DSD (min.)	J_g	current density in a lasing region of the device
A	curve fitting constant (cm ⁴ /A ²)	L	cavity length (μm)
λ, λ_o	lasing wavelengths (nm)	L_a	length of dark portion of cavity (μm)
$h = 6.6262 \cdot 10^{-34} \text{ J}\cdot\text{sec}$	Planck's constant	α_{2deg}	absorption coefficient for dark region (1/ μm)
p	photon momentum (kg·m/s)		
$c = 2.998 \cdot 10^8 \text{ m/sec}$	speed of light		
n_f, N_f	final donor concentration		
n_i, N_i	initial donor concentration		

α_{2deg}	absorption coefficient before degradation. $(1/\mu m)N_{dl}$	J_o	threshold current density across a $1\mu m$ thick active layer
	number of dark lines	Γ	containment factor
W_a	dark line width (μm)	η_s	slope efficiency (W/A)
J_t	total current density	η_i	internal differential quantum efficiency
α_a	absorption coefficient in a dark region ($1/\mu m$)	ν	lasing frequency (Hz)
α, α_g	absorption coefficient in a lasing region ($1/\mu m$)	$q = 1.602 \times 10^{-19}$ C	electronic charge
R, R_o	reflection coefficients	E	electric field (N/C)
β_d	gain coefficient	z	propagation distance (m)
α_d	cavity loss ($1/\mu m$)	r	radial distance from propagation axis (m)
d	active layer thickness (μm)	w	spot size (m^2)
m	exponent of current dependency on gain	w_o	waist, minimum spot size (m^2)
α_o	cavity loss before degradation ($1/\mu m$)	θ	half width divergence angle (rad)
α_{mo}	mirror loss ($1/\mu m$)	ct	cavity thickness (μm)
R_{th}	rate of change of normalized threshold current (1/hr)	slp	calculated slope efficiency (W/A)
R_1, R_2	reflection coefficients	C	current normalization factor
g_{th}	threshold gain coefficient	ot	operation time (min)
n, n_s	refractive index	st	standard deviation of ot (min)
g_{max}	maximum gain coefficient	R_c	specific contact resistance (Ω)
\dots	curve fitting constant	A^*	effective Richardson constant ($J/C^\circ K^2$)
		ϕ_{Bn}	barrier height (eV)
		m_n	carrier effective mass (kg)
		ϵ_s	semiconductor permittivity (F/cm)

N_D doping density ($1/\text{cm}^3$)

$\hbar = 1.054 * 10^{-34}$ J-sec

reduced Planck constant

Bibliography

1. M. Fukuda, Reliability and Degradation of Semiconductor Lasers and LED's, Artech House, Inc. 1991.
2. P.G. Eliseev, Reliability Problems of Semiconductor Lasers, Nova Science Publishers, Inc. 1991.
3. T. Kobayashi, T. Kawakami, and Y. Furukawa, "Thermal Diagnosis of Dark lines in Degraded GaAs-AlGaAs Double-Heterostructure Lasers", Jpn. J. Appl. Phys., Vol. 14, pp. 508-515, 1975.
4. M. Fukuda, K. Wakita, and G. Iwane, "Dark defects in InGaAsP/InP double heterostructure lasers under accelerated aging", J. Appl. Phys., Vol. 54, pp. 1246-1250, 1983.
5. M. Fukuda, K. Wakita, and G. Iwane, "Observation of Dark Defects Related to Degradation in InGaAsP/InP DH Lasers under Accelerated Operation", Jpn. J. Appl. Phys., Vol. 20, pp. L87-L90, 1981.
6. Gfeller, F.R. and D.J. Webb. "Degradation and lifetime studies of high-power single-quantum-well AlGaAs ridge lasers," J. Appl. Phys. Vol. 68: 14-20 (July 1990).

7. T. Egawa, Y. Hasegawa, T. Jimbo, and M. Umeno, "Effects of Dislocation and Stress on Characteristics of GaAs-Based Laser Grown on Si by Metalorganic Chemical Vapor Deposition", Jpn. J. Appl. Phys., Vol. 31, pp. 791-797, 1992.
8. W. Fritz, "Gradual bulk degradation in (AlGa)As laser diodes during -20 °C tests due to arsenic-out diffusion", J. Appl. Phys., Vol. 66, pp. 2260-2264, 1989
9. S.N.G. Chu, S. Nakahara, M.E. Twigg, L.A. Koszi, E.J. Flynn, A.K. Chin, B.P. Segner, and W.D. Johnston Jr., "Defect mechanisms in degradation of 1.3- μ m wavelength channelled-substrate buried heterostructure lasers", J. Appl. Phys., Vol. 63, pp. 611-623, 1988.
10. W. Fritz, T. Faltus, J. Yahl, "Failure mechanisms in monolithic AlGaAs laser devices", Proceedings of the SPIE, Vol. 1219, pp. 211-215, 1990.
11. R.B. Martins, P. Henoc, B. Akamatsu, and J.F. Palmier, "A model for the degradation of Ga(Al)As single-quantum well lasers", J. Appl. Phys., Vol. 70, pp. 554-561, 1991.
12. H. Yonezu, M. Ueno, T. Kamejima, and I. Sakuma, "Lasing Characteristics in a Degraded GaAs-Al_xGa_{1-x}As Double Heterostructure Laser", Jpn. J. Appl. Phys., Vol. 13, pp. 835-842, 1974.
13. Yoo, J.S., M.S. Oh, H.S. Park, S.T. Jung, G.T. Park, and K.Y. Park. "Studies on the Low Local Temperature Rise in the Mirror Facet of a High-Power In BaAsP/GaAs Laser", Jpn. J. Appl. Phys. Vol. 31: L1686-L1688 (December 1992).

14. Ghafouri-Shiraz, H. "Analysis of facet reflectivity, mirror loss, single-transverse mode condition and beam divergence angle at 1.3 micron and 1.55 micron wavelength of InGaAsP/InP buried heterostructure semiconductor laser diodes," Optics & Laser Technology Vol. 22 : 38-46 (No. 1 1990).
15. Chen, T.R., Y. Zhuang, Y.J. Xu, D. Perry, N. Bar-Chaim, A. Yariv, B. Yu, Q.Z. Wang, Y.Q. Zhou. "Applications of a dielectric coating to semiconductor lasers," Optics & Laser Technology Vol. 22: 245-254 (No. 4 1990).
16. Chinone, N., H. Nakashima, and R. Ito. "Long-term degradation of GaAs-Ga_{1-x}Al_xAs DH lasers due to facet erosion," J. Appl. Phys., Vol. 48: 1160-1162 (March 1977).
17. Hayakawa, T., S. Yamamoto, T. Sakurai, and T. Hijikata. "Facet degradations in Ga_{1-x}Al_xAs/Ga_{1-y}Al_yAs double-heterostructure lasers," J. Appl. Phys. Vol. 52: 6068-6073 (October 1981).
18. T.C. Shen, G.B. Gao, and H. Morkoc. "Recent developments in ohmic contacts for III-V compound semiconductors," J. Vac. Sci. Technol. B 10(5): 2113-2132 (September/October 1992).
19. S.M. Sze, Semiconductor Devices, Physics and Technology, AT&T Bell Laboratories, 1985.
20. J. T. Verdeyen, Laser Electronics, 2nd Edition, Prentice Hall, Inc., 1989

21. J. Bardeen, "Surface State and Rectification at a Metal-Semiconductor Contact," Physical Review, Vol. 17, number 10: 717-727 (1947).
22. P. R. Bevington, Data Reduction and Error Analysis for the Physical Sciences, McGraw-Hill Book Company, 1969.
23. K. W. Böer, Survey of Semiconductor Physics, Vol. II, Van Nostrand Reinhold, 1992.
24. Mathcad, Version 3.1. Computer software. MathSoft, Inc. 1992.

Vita

Captain David H. Leicester was born 4 January 1967 in Santa Monica, California and grew up in Pacific Palisades, California. He graduated from Palisades High School in 1985 and attended Northwestern University, graduating with a Bachelor of Science in Electrical Engineering in June 1989. Upon graduation, he received a reserve commission in the USAF and served his first tour of duty at Eglin AFB, Florida. He began as a Software Consultant for the 3200 Support Squadron and later served as a Computer Hardware Interface Specialist, fabricating customized interface units for Eglin's testing computer network. He entered the Graduate School of Engineering, Air Force Institute of Technology, in May 1992.